Process-Induced Defects during Tow Steering in Automated Fiber Placement: Experiment, Modeling and Simulation

Nima Bakhshi

A Thesis
in
The Department
of
Mechanical, Industrial and Aerospace Engineering

Presented in Partial Fulfillment of the Requirements
for the Degree of Master of Applied Science in Mechanical Engineering at
Concordia University
Montreal, Quebec, Canada

November 2018

CONCORDIA UNIVERSITY

School of Graduate Studies

This is to certify that the thesis prepared

By: Nima Bakhshi

Entitled: Process-Induced Defects during Tow Steering in Automated Fiber Placement: Experiment, Modeling and Simulation

and submitted in partial fulfillment of the requirements for the degree of

Master of Applied Science (Mechanical Engineering)

complies with the regulations of the University and meets the accepted standards with respect to originality and quality.

Signed by the final Examining Committee:

_____ Chair

Dr. Kudret Demirli

_____ Examiner

Dr. Suong Van Hoa

_____ Examiner

Dr. Lucia Tirca

_____ Supervisor

Dr. Mehdi Hojjati

Approved by _____

Dr. Martin D. Pugh

Chair, Department of Mechanical, Industrial & Aerospace Engineering

November 27, 2018 _____

Dr. Amir Asif, Dean

Dean, Gina Cody School of Engineering and Computer Science

ABSTRACT

Process-Induced Defects during Tow Steering in Automated Fiber Placement:
Experiment, Modeling and Simulation

Nima Bakhshi

Various advantages offered by Automated Fiber Placement (AFP) have led to its increasing application in the aerospace industry to manufacture high-quality, large structural parts. Application of this technology, however, is considerably restrained by the defects that appear in the layup particularly during tow steering. An extensive experimental investigation using various process parameters and steering radii is performed to gain a deeper understanding of defect formation processes during steering of thermosetting prepreg tows. Five predominant defect types, namely in-plane fiber waviness, sheared fibers, tow pull up (bridging), blisters and out-of-plane wrinkles that occur during the steering are identified. The defects formation mechanisms are explained and discussed. Furthermore, a more detailed set of experiments is performed to capture the viscoelastic growth of individual wrinkles with time.

A novel finite element modeling framework for simulating the prepreg deposition process is presented in the commercial finite element software, Abaqus. It is demonstrated that by prescribing the global behavior of prepreg tow during the process and representing prepreg tack with an appropriate cohesive zone model, this approach is capable of capturing wrinkles and blisters that are caused by tow steering. Moreover, the conventional local approaches for modeling defects are extended by utilizing a viscoelastic interface to develop a theoretical model which is capable of demonstrating the time-dependent growth of wrinkles.

The interaction between prepreg and compaction roller is known to be influential on the quality of the deposited tow. Five compaction rollers with different materials, stiffness, and architecture are built. In a series of experiments the effect of each roller on the appearance of defects, particularly on blisters is investigated. The optimum roller design based on the experimental observations was identified.

ACKNOWLEDGEMENTS

I would first like to express my sincerest appreciation to my supervisor Dr. Mehdi Hojjati for his immense trust, support and guidance throughout this program. The present work would not be possible without him.

I like to thank Mr. Jeffrey Fortin-Simpson and Dr. Daniel-Iosif Rosca for performing the AFP trials that were used for producing the experimental data presented in chapters 3 and 6, respectively. I would also like to thank my friends and colleagues from Concordia Center for Composites especially, Mr. Muhsan Belhaj and Mr. Mohammad Hossein Ghayour for their collaboration and fruitful discussions on the topic.

Last but not least, my sincerest thanks to my parents for their endless love, support and continuous encouragement throughout my years of study. I would like to dedicate this work to them.

DEDICATION

To my beloved parents.

TABLE OF CONTENTS

LIST OF FIGURES

LIST OF TABLES

1 INTRODUCTION

1.1 BACKGROUND AND MOTIVATION

Composite materials have gained a significant importance and application in various industries during the past few decades. Figure 1.1 demonstrates the rapid introduction and increasing application of composite materials in Airbus airplanes as an example of composites' demand in the aerospace industry which is one of the major consumers of composite materials. Large structural aircraft components have been designed and manufactured using composites, in order to take advantage of their superior properties to excel at structural efficiency as well as passenger experience.

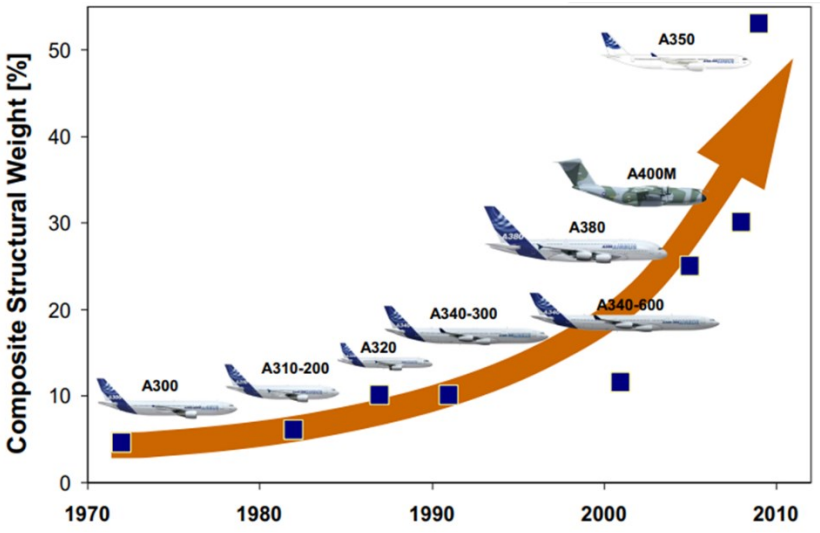

Figure 1.1 Structural weight (%) of composites in Airbus aircrafts over the years.

High demands of the production as well as manufacturing quality consistency requirements have resulted in the development of automated technologies for stacking composite lamiae to laminate parts. In addition to increased productivity, lower labor intensity and higher quality consistency, automated technologies such as automated fiber placement allow the user to steer the prepreg tows and place them on curvilinear fiber paths. Using curvilinear fiber paths opens up a new and more flexible design space which enables the composite engineers to take full advantage of the *directionality* of composite materials and further tailor composites' mechanical properties for a

specific well-defined application. This relatively new family of composites is known as variable stiffness composites and has been gaining increasing importance in recent years.

Steering prepreg tows, however, is not limited to the manufacturing of variable stiffness composites. Keeping the desirable constant fiber orientation on non-flat tools requires some level of tow steering. Essentially, as demonstrated in Figure 1.2, any fiber path other than the tool surface *geodesic*[1] requires the prepreg tow to steer away from the geodesic of the tool surface.

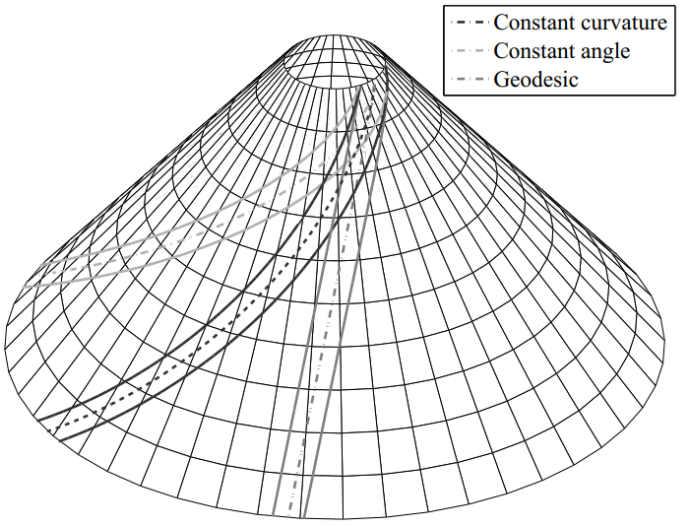

Figure 1.2 Three different tow paths on a cone.

Due to a prepreg's property called tack (i.e. prepreg's adhesiveness), tow is ideally able to remain on the prescribed reference path. The strength of prepreg tack can be moderately controlled using process conditions such as layup temperature, material deposition speed and compaction pressure. If the prepreg tack is not strong enough to strictly keep the prepreg tows on the prescribed fiber paths, various different defects may appear in the layup. Existence of these defects in the uncured

[1] Geodesic is, essentially, the generalization of the concept of straight line to curved spaces. It is the shortest path between two points on a surface in the three dimensional space. This is the path a prepreg tow would naturally want to move towards.

laminates can severely affect the mechanical properties of the final cured parts. Consequently, manufacturers discard the defective layers and avoid the conditions leading to the defects entirely.

Identifying all defects that can appear in steered tows and gaining a deeper understanding of the processes driving the formation of the defects are crucial for facilitating the industrial-scale manufacturing of variable stiffness composites, and moreover, for further optimizing the manufacturing processes involved in the production of existing traditional composites with constant fiber orientations. Relevant theoretical approaches as well as simulative frameworks for modeling the automated fiber placement and specific defect formation processes should be developed and their application for attaining this purpose should be explored.

1.2 Aims and Objectives

One of the primary objectives of the present study is to identify different types of defects that can appear in steered prepreg tows. Moreover, it is intended to obtain a deeper understanding regarding the processes that are fundamentally driving or contributing to the formation of each of these defects, in order to propose possible strategies to alleviate them. Aligned with this purpose, theoretical models and simulative frameworks should be developed to help in further understanding the process and provide tools for predicting the appearance of defects in a given steered tow which is laid down at specific process conditions.

1.3 Thesis Outline

A review of the relevant literature is presented in chapter 2. Automated technologies of manufacturing composite materials and specifically automated fiber placement are briefly discussed. The concept of prepreg tack, its fundamental origins, historical development, and application in the context of b-stage prepreg materials is presented. Finally, the existing studies and models of the defects that appear in steered tows are reviewed.

Chapter 3 presents the primary experimental observation of this study. Different defects that can appear during tow steering are identified and the effect of most influential process parameters on each of them is described. Moreover, time dependent formation and growth of the out-of-plane winkles (as one of the most commonplace defects formed in steered tows) is experimentally

investigated. Interpreting the experimental results presented in this chapter (and chapter 6) are predominantly dependent on observing the layup images. Therefore, using the electronic version of the thesis can be more beneficial.

Two novel modeling approaches, namely the local and global modeling approaches, are developed in chapter 4. Moreover, the experimental procedures utilized for characterizing the mechanical properties of uncured prepregs are described in this chapter. Chapter 5 presents the results of the models and their experimental validation. Moreover, relevant discussions and implications of the models are discussed.

A more in-depth experimental investigation into the effect of compaction roller used for depositing prepreg tows is presented in chapter 6. Contribution of roller material and architecture to the formation of defects is discussed and the optimal strategy for mitigating layup defects and increasing productivity is identified.

Finally, major findings and accomplishments of the thesis are summarized in chapter 7. Taking into account the versatility of the scope of research related to the automated manufacturing of thermosetting composite materials, possible worthwhile opportunities and research directions are presented.

2 LITERATURE REVIEW

2.1 AUTOMATED MANUFACTURING OF COMPOSITES

Manufacturing of composite materials started with the wet hand layup process (Figure 2.1). Wet hand layup is a relatively simple process, suitable for low cost composite applications, in which reinforcements or fibers are laid down on the mold by hand. Subsequently, catalyzed resin is added to the fibers through the application of a hand roller or a spray. This process is repeated for the desired number of layers until the required thickness and laminate stacking sequence are achieved. Alternatively, prepreg materials can be used in a similar manufacturing setup in a process called dry hand layup process. Prepreg materials are tacky viscoelastic deformable sheets constituting continuous fibers that are already impregnated by b-stage (or partially cured) resin systems, usually epoxy. Utilizing prepreg materials can significantly improve the mechanical properties and final part quality, as well as quality consistency by for instance, increasing fiber volume fraction (~ 65% in prepregs), improving fiber/resin interface (as a result of a better controlled, separate specialized process), reducing resin rich areas, void content and irregularities. Furthermore, prepregs can improve material handling issues and provide a better control on thickness of the final parts [1].

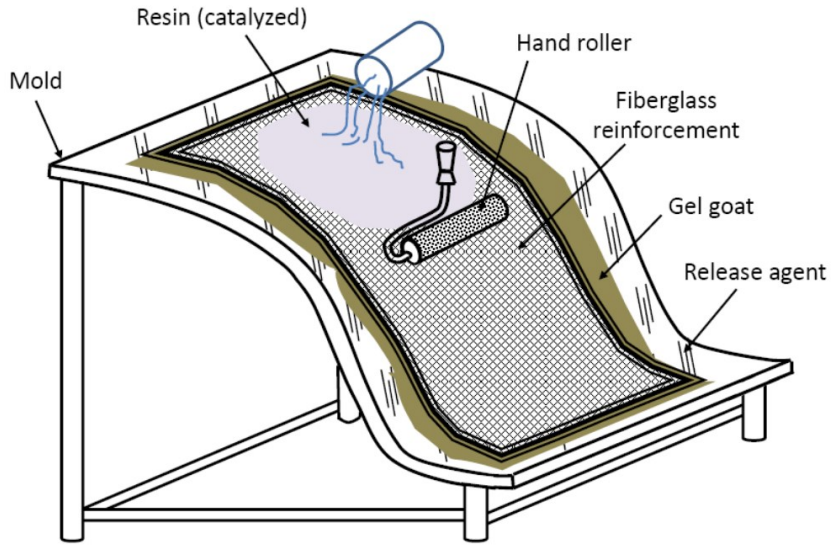

Figure 2.1 Wet hand layup process [1].

Both hand layup processes are, in general, time-consuming, low in productivity and labor intensive. The best dry hand layup technicians can merely laminate about 1.1 kg of material per hour [2]. Moreover, the quality of the final part is highly dependent on the skills of the operator which makes them even more prone to repeatability, quality consistency and accuracy issues. Additionally, emission of hazardous chemicals from the resins and curing agents raises serious health and environment related issues that make the wet layup further inconvenient.

With the increasing demand for higher productivity and quality consistency on one hand, and technological advancements in the robotic industry on the other hand, automation has paved its way into the composites manufacturing. Automated Fiber Placement (AFP) in conjunction with the Automated Tape Layup (ATL) are two of the automated technologies in composite manufacturing that has recently gained significant importance in the aerospace industry as well as the automotive and renewable energy industries. In these technologies, some type of a robotic arm, mimicking the layer-by-layer deposition of prepregs in dry hand layup, stacks prepreg laminas on the mold. AFP and ATL has been used to manufacture large-scale parts such as the section 41 (forward fuselage) of Boeing 787 in one piece (Figure 2.2).

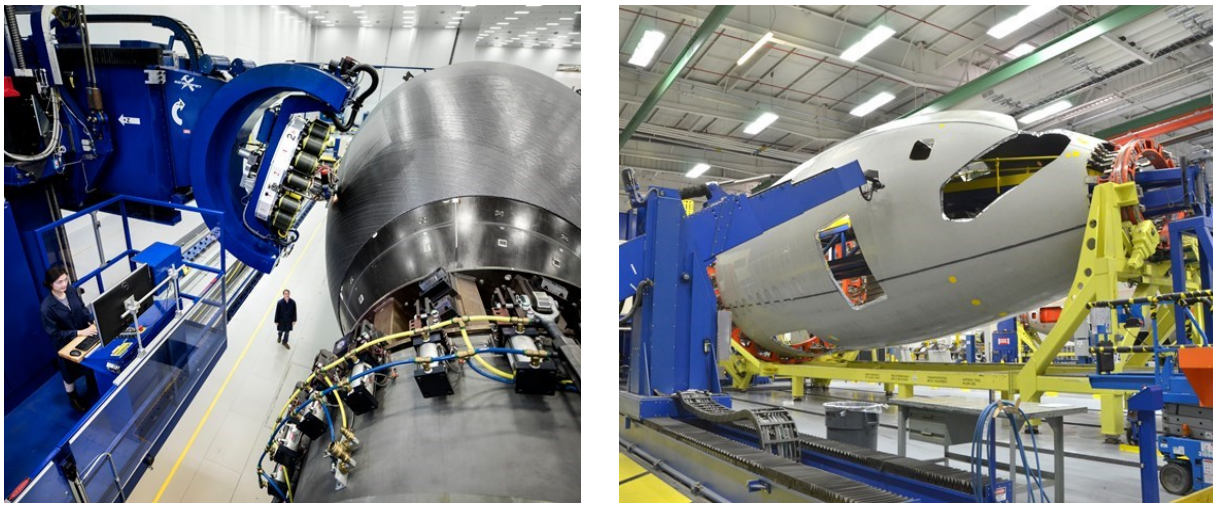

Figure 2.2 Forward fuselage of Boeing 787 [3].

Narrow prepreg tows or slit prepreg tapes of width 3.2, 6.4 or 12.7 mm are usually used in the AFP. Individual tows are pulled from the spools located on top of the AFP head. The backing paper protecting one side of the prepreg is separated and the prepreg is fed through a fiber delivery system to the AFP head. Several tows (up to 32 tows in parallel) are collimated on the compaction roller to form a wider band, called a course, and are placed onto the mold surface.

ATL on the other hand utilizes wide prepreg tapes of 75 to 300 mm and hence has a higher productivity in comparison to the AFP. Consequently, ATL is an efficient way for manufacturing large and non-complex structures where wide tapes can be used. Due to the large mass and dimensions of the parts as well as materials, ATL systems are usually mounted on horizontal gantries or vertical column system. Whereas, in AFP, parts and materials are usually mounted on an articulated robot arm. Tapes are heated on the layup delivery system or in front of the ATL head, and they are placed onto the mold by the application of compaction force at a predefined speed. Finally, at the end of each layer, tapes are cut by rotating or pinching blades.

Among two different automated technologies available for composite manufacturing that are currently commercially available, Automated Fiber Placement is particularly of interest in the present work since it is able to perform tow steering and ergo laminate more complex geometries. A typical AFP head with a modular design consisting of eight functioning modules is depicted in Figure 2.3. The head demonstrated below has an on-board creel as the material supply unit. The on-board creel reduces the traveling distance of the prepreg tow which in turn reduces problems such as fuzzball formation and twisting tows. Contrary to the external creels that are typically employed in ATL systems. The backing paper is removed as soon as the tow is unwinded from its bobbin and it is stored on the adjacent spool (red spools in Figure 2.3). Additionally, the application of a tension control generates the fiber tension required to keep the fibers straight and also compensates for the dynamical effects of the process.

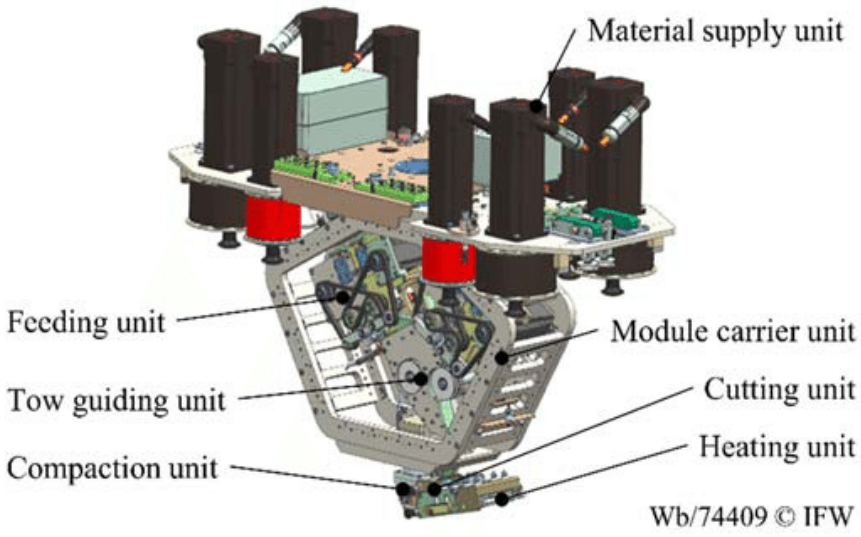

Figure 2.3 A typical AFP head with modular design [4].

The feeding unit continuously provides the tape with the required feeding rate. Furthermore, it is responsible for restarting the process. A tow guiding unit is placed between the cutting unit and the feeding unit, in order to provide a direct passage of materials. Hot flow of gas, torch, infrared lamps, laser or ultrasonic heaters can be utilized in the heating unit of the head in order to heat up the tow. Hot gas torch is the most popular heat source used in the automated manufacturing of composites. Nitrogen can be used to avoid oxidation of the surface at elevated temperatures. The choice of technology used might to some degree depend on whether the head was designed for thermosetting or thermoplastic tows. In addition, the temperature of thermosetting prepreg tows inside the AFP feeding mechanism is usually kept around $5°C$ in order to prevent residual resin to adhere to the mechanical parts (particularly in humid environments where the prepreg tack is enhanced).

Knife-edge cutting and laser cutting can be utilized in the cutting unit. The importance of this unit resides in the fact that a considerable number of cutting scenarios are expected to be performed "on-the-fly", i.e. without stopping the prepreg deposition process. By increasing the speed of deposition process, expectably, the cutting quality decreases, as a result of which secondary operations on the uncured laminate become necessary.

Compaction unit of the AFP head may consist of different segments for dispensing large number of tows, each segment having a flexible roller that can conform to different features of molds. A pneumatic actuator provides the required level of compaction force, with a force sensor controlling the value of the force applied. Additionally, a process monitoring unit comprised of several positioning, temperature and force sensors might be available within the head to gather data regarding different process parameters such as the temperature distribution in the laid down tow [5-7].

Various advantages AFP offers, has led to its increasing application in the aerospace industry to manufacture high-quality aerospace parts. Higher productivity and part quality with fewer variations and uncertainties, as well as a decrease of labor intensity and minimization of the number of the required parts (through integration as can be seen in Figure 2.2) can be obtained through this technology. AFP offers some unique features that specifically make it desirable for manufacturing complex parts with superior material properties. One of the key features of the AFP is that each tow in a course can have a different speed, and can be dispensed, cut and restarted individually. Therefore openings and holes can be produced without requiring major additional manufacturing steps.

The ability to deliver tows with different speeds, also called differential tow pay-out, enables the AFP machines to laminate complex geometries and perform tow steering. In parts with complex geometries (including structures as simple as a cylinder or a sphere), steering the fiber path away from the geodesic path of the tool surface to maintain the desired fiber orientation is unavoidable. In addition, the steering ability opens a new much more flexible design space for further tailoring the mechanical behavior of composite structures with using curvilinear fiber paths. This results in exploiting the full potential of the directionality of composites [6, 8], hence developing more efficient and optimized composite structures.

2.2 TACK

2.2.1 Fundamentals

Two bodies are essentially said to be adhered when some work needs to be performed in order to separate them. Historically, tack has been *subjectively* defined as the feeling of stickiness or adhesion one feels upon retracting one's finger when touching an adhesive material. Even to date, prepreg manufacturers use adjective descriptions such as low, medium and high to describe the prepreg tack. This is due to some intrinsic difficulties in studying and objectively characterizing tack that has led to lack of reliable and standardized measurement methods. In this section, while reviewing some fundamentals of adhesion, available experimental methods for characterizing tack and previous works on prepreg tack will be presented.

In nature, four fields are understood to be fundamentally responsible for holding atoms and molecules together [9]. They are known as strong, week, electromagnetic and gravitational fields. Strong and week forces are confined to the nucleus of atoms. Moreover, gravitational fields are usually ignored in small scales, as will be demonstrated in the following, since they are negligible in comparison to atomic forces. Electromagnetic forces are resulted from polarization of atoms or molecules through rearrangement of electrons and include covalent and ionic bonds, and Van der Waals forces. Among these forces, ionic and covalent forces are relatively very strong *intramolecular* interactions that generate chemical bonds. Van der Waals force, however, are not a result of any chemical electronic bond and vanish at larger distances. Strong Van der Waals forces are induced when the gap between the materials is below 10 nm, therefore, very close and intimate contact is required for obtaining considerable adhesive interactions [10]. Additionally, coulomb forces that are purely a result of charged bodies can play a role in attracting (or repelling) surfaces and might be used in future to enhance prepreg tack for materials that can hold static charges.

A useful way of thinking about adhesive active forces is through the adiabatic work which is performed by these forces during attraction. The reversible thermodynamic work required to pull contacting surfaces apart is given by the Dupré equation, $W = \gamma_1 + \gamma_2 - \gamma_{12}$; where γ_1, γ_2 and γ_{12} are the *solid-vapor interfacial energies* of solid 1 and 2, and the interfacial energy of contact

between solids 1 and 2, respectively. The Dupré work of adhesion is often used in order to incorporate adhesion into quantitative models of contact.

The molecular level of adhesion is not simply scalable to the macroscopic engineering scale. Other physical phenomena such as surface roughness and non-adiabatic processes involved should be considered for engineering purposes. Surface roughness generally (although not always and across all scales) works against the adiabatic work of adhesion, W, and reduces it. While non-adiabatic processes, for instance viscoelastic dissipations or plastic deformations involved in the detachment mechanism, can significantly increase the effective work of adhesion in soft rubbers [11].

As an example, considering merely Van der Waals forces, about the weight of a car is required to separate two flat surfaces with 1 cm^2 cross-section in contact [12]. This is in contrast to everyday life where adhesion usually does not interfere in an enormously negative way. The reason for negligible adhesion in large scales (often called "adhesion paradox") is that in large surfaces, separation progresses through crack propagation, while in small surfaces (order of 100 μm or smaller) bond breaking occurs uniformly, at once. Additionally, the surface roughness in real situations causes the "true" contact area to be much lower than the ideal or nominal one. More importantly, in order to bring surfaces into contact, the local asperities must deform. During the pull-off, the stored elastic energy will contribute and help in separating the surfaces.

Figure 2.4 (from [10]) shows a comparison between the gravity and the force required to separate two identical spheres that are in contact with each other and the gravitational force acting on them. For a small bearing (1 μm in diameter) the adhesion force is more than a million times greater than the force of gravity. While for larger spheres, the adhesion force becomes negligible in comparison to gravity. Contact models including JKR [13], DMT [14], Maugis [15] and Bradley [16] models predict a linear relationship between the required pull-off force and diameters of sphere: $F = kWD$. Where, k is a constant different in each model, W is the Dupré work of adhesion and D is diameter of spheres in contact. However, gravitational force scales with order three (related to volume). Considering the negative effect of surface roughness on true contact area and the energy distribution at contact surface, in conjunction with the comparison with the force of gravity, demonstrates why scale is very important in the analyses regarding adhesion.

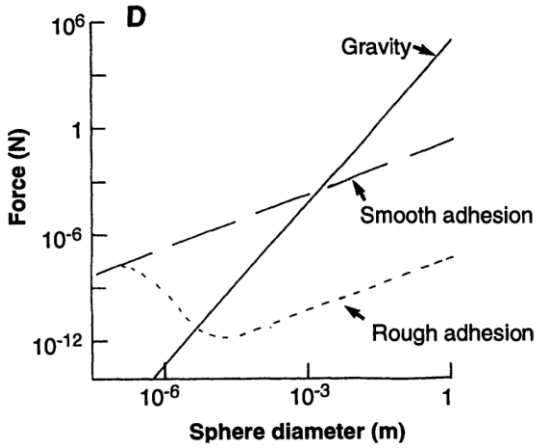

Figure 2.4 Two identical spheres in contact: comparing the gravity and Van der Waals forces.

2.2.2 Development of the Concept of Tack

Tack is not an inherent property of materials. The final application determines what the exact meaning of tack is, in each application and makes the design of appropriate test methods possible. From the chronological perspective, tack has been an important property in ink and Pressure Sensitive Adhesive (PSA) industries, and more recently, it has gained significant importance in automated manufacturing of composite.

In the ink industry, tack is defined as the pull resistance of the viscous liquid to an oppositely directed force. Consequently, it is tested through application of force to two parallel plates, between which the liquid is inserted. This property is very closely related to the viscosity of the liquid and can be predicted through the application of modified viscous flow theory [17].

Pressure sensitive adhesives should be able to form a firm bond instantaneously upon contact with a solid surface [18]. In application to adhesives, Dahlquist in 1969 showed for the first time that tack is not a fundamental physical property such as viscosity or elastic modulus. Rather it is influenced by the viscoelastic properties of the adhesive. Moreover, several researchers demonstrated that the adhesive tack follows the time-temperature superposition (TTS) principle, indicating its relation to the viscoelasticity of materials [19]. The American Society for Testing and Materials (ASTM) defines tack as the force required to separate an adherend and an adhesive

at the interface shortly after they have been brought rapidly into contact under light load over a short duration.

Several methods are available for the quantitative analysis of PSA tack (see for e.g. [20]), some of which are demonstrated in Figure 2.5. In the rolling ball test, a 7/16 in-diameter standard ball is set on a standard inclined plane (according to ASTM D3121-94), in front of which the PSA is located (green tape in the picture). The length the ball can travel on the PSA as a result of its potential energy is an indicator of PSA tack which provides a quantitative basis for comparing different adhesives. SATRA test is a test method developed specifically for shoe industry where they need to know how long the adhesive can keep its *tackiness*. Loop tack test is another method of testing which provides a value for the "quick stick" value of tack. These testing methods provide values related to a specific end-use performance, by mimicking the application. They tend to measure different phenomena that are rather influenced by tack and provide little control over conditions that can influence tack.

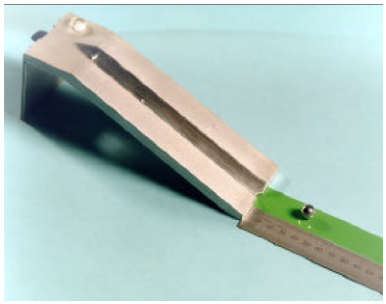

a. Rolling ball test

b. SATRA test method

c. Loop tack test

Figure 2.5 Tack test methods [20].

Two test methods that have been very important in increasing our understanding of adhesives are probe tack test method and peel test. Peel test [21, 22] is used often to measure the strength of adhesive joints and PSAs. Depending on the application and stiffness of the adhesive substrate, different fixtures and different peeling angles might be used for this test (Figure 2.6 (a)). For instance, when using PSAs on substrates with higher stiffness, a mandrel might be installed at the peel front where the interface is expected to fail in order to facilitate load transmission. In this test, the force required to peel the PSA, normalized by the width of the substrate is used to quantify adhesion. This measured quantity represents the *non-equilibrium* work of adhesion and is useful in providing engineering estimates for adhesion in different applications. Moreover, the fracture energy (i.e. the critical energy release rate) of the adhesive can also be obtained through analyzing the data measured from peel test, using fracture mechanic [23] methods (see for example [24-26].

Another very important tack measurement method is the probe tack test apparatus which is essentially the rational extension of the historical definition of tack (finger touch) in order to perform the experiment with more controllable and quantifiable variables. Figure 2.6 (b) demonstrates a typical systems consisting of the fixtures, a probe and a camera and mirror setup (or some other setup) to monitor the deformations at the interface.

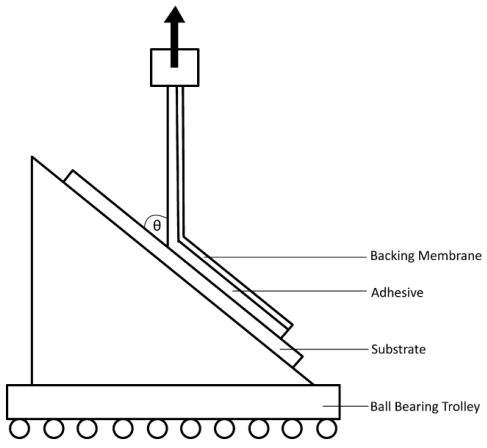

a. Peel test with angle θ [22]

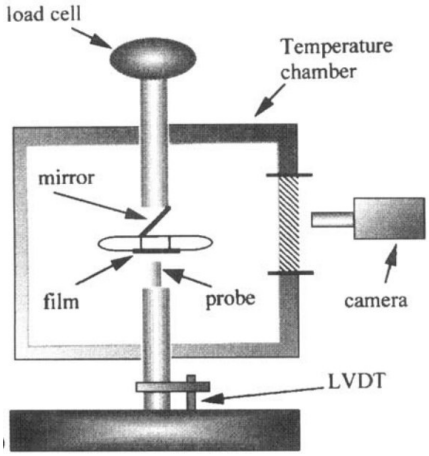

b. A detailed probe tack test setup [27]

Figure 2.6 Tack test methods, continued.

In the probe tack test, a flat-faced probe comes into contact with the material in question until a certain prescribed pressure is reached. The probe remains in contact with the PSA for a specified time, then it is drawn away at a specified rate. The stress (or force) versus displacement curve is recorded during the retraction of the probe. Two most important data this method provides is the total fracture energy (area below the curve) and the maximum stress at which the softening of the adhesive strength initiates.

From the perspective of adhesives behavior, probe tack test is comprised of five separate stages (Figure 2.7) [28]. The first step is the formation of interface which occurs when the probe is kept in contact with the adhesive material. Various parameters such as the specifics of the material, surface roughness and materials of the probe, temperature, humidity, contact time and pressure affect formation of the intimate contact as well as the strength of the interface. Second stage is the initiation of debonding process through formation of cavities. Debonding stage starts before the maximum stress is reached as it is clear from the microscopic images. This is subsequently followed by the lateral growth of the cavities which is manifested in the stress-strain curve by a steep drop in stress levels. The fourth stage accompanies growth of the cavities in the direction normal to the plane of the adhesive film (fibril formation) which results in a plateau in the stress vs. strain curve. Finally, surfaces become separated. Two different modes of failure, namely adhesive failure or cohesive failure might occur. In the adhesive failure, strength of the interface is the limiting factor. Consequently, the plane of failure is exactly at the probe-adhesive interface which can be identified by inspecting the clean probe surface. In the cohesive failure, on the other hand, the interface is stronger than the cohesive strength of the adhesive material. Therefore, the failure occurs in the bulk of material, resulting in some level of residual resin on the probe surface.

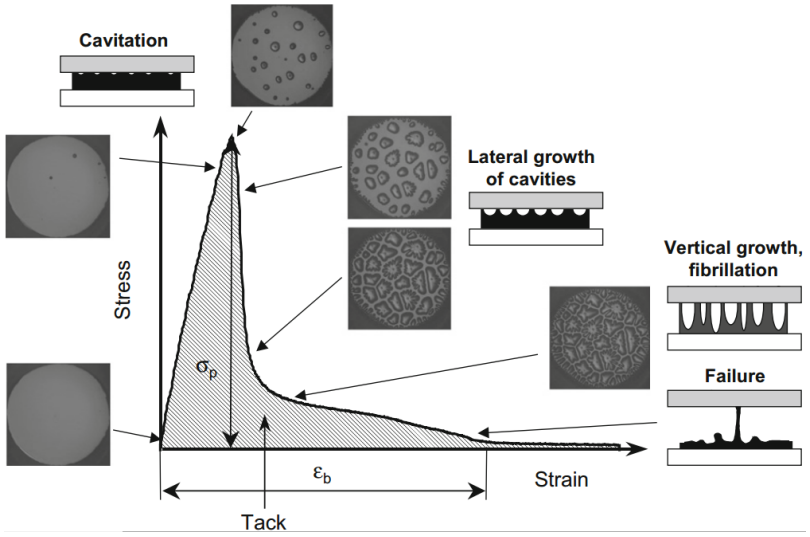

Figure 2.7 Result of tack test for PSAs; separation of stages [28].

Having reliable testing apparatus and protocols such as the probe tack and peel tests which were able to produce replicable results allowed researchers to study the properties of adhesives more extensively. Using linear and nonlinear rheology, effects of different rheological, molecular and mechanical properties as well as application conditions (e.g. surface roughness, temperature and rate of application) have been studied on and correlated to the adhesion of PSAs. This is because rheological properties such as the elastic modulus, loss modulus and the phase angle can well represent the solid like and liquid like behaviors of a viscoelastic material at a given rate and temperature. Comprehensive reviews of these topics are available and the interested reader is encouraged to pursue [9, 23, 27, 29, 30].

In essence, however, an adhesive is effective if it possesses both liquid properties, to wet the surface when the surfaces has came to contact, and solid properties, to sustain and resist a certain level of stress during the process of debonding. Structural adhesives can more easily accomplish this by a chemical reaction, typically a polymerization, which transforms a liquid mixture of oligomers into a crosslinked polymer. But for PSAs or prepregs, they should be able to exhibit appropriate properties in the corresponding stage of application to be able perform.

2.2.3 Prepreg Tack

Tack and drape of prepregs are two primary concepts that describe material's suitability for layup. Prepreg tack is the property that allows prepreg sheets (or tows) to adhere to the preceding plies, or to the tool surface, so that multiple plies can be stacked and maintained at a desired fiber orientation. Tack should be strong enough to keep the prepreg tows on the prescribed surface which is especially important when laminating on curved tools or steering the fiber path away from the geodesic path of the tool surface. On the other hand, tack should not be too strong, so when a ply is misplaced it can be easily peeled off and relocated without damaging the preceding plies. Moreover, in the AFP process, tack between the prepreg and application rollers needs to be minimal to prevent resin from building up on the rollers, or prepreg sticking to and eventually wrapping around the rollers.

High rate of material deposition is crucial for maintaining the desired level of process productivity. Hence, tack should be formed in a very short amount of time. Prepreg tack, as explained, is similar to PSA tack. However, characterization and analysis of prepreg tack is more complicated since prepregs consist of continuous reinforcing fibers that introduce some significant changes to the structure and surfaces of prepreg sheets.

In industrial settings, prepreg tack used to be characterized by measuring the time it could stick to a support in a vertical position at room temperature. The tack would be considered acceptable if the prepreg specimen remained in position for a specified duration [31].

More rigorous analysis of prepreg tack began by the work of Seferis et al. [19, 32, 33]. Tack was assumed to be merely a bulk property (among prepreg layers) rather than a product of the interplay between bulk prepreg behavior and interface interactions. They devised a method for measuring tack (per their specific definition) and developed a viscoelastic model for predicting the measured quantity. Figure 2.8 demonstrates the developed setup as well as a typical stress-strain curve resulted from this experiment. Compression to tension test developed in their work comprised of two tabs between which a stack of prepregs is placed. The moving tab (upper one in the picture) comes down into contact with the stack of prepregs until the prescribed level of pressure is achieved (stage A). It maintains that level of pressure for a given amount of time, while the prepreg stack is further compressed as a result of the dissipation of voids between prepregs and prepregs

viscoelastic creep response (stage B). Finally, the upper tab is retracted and the prepreg stack is unloaded stage C).

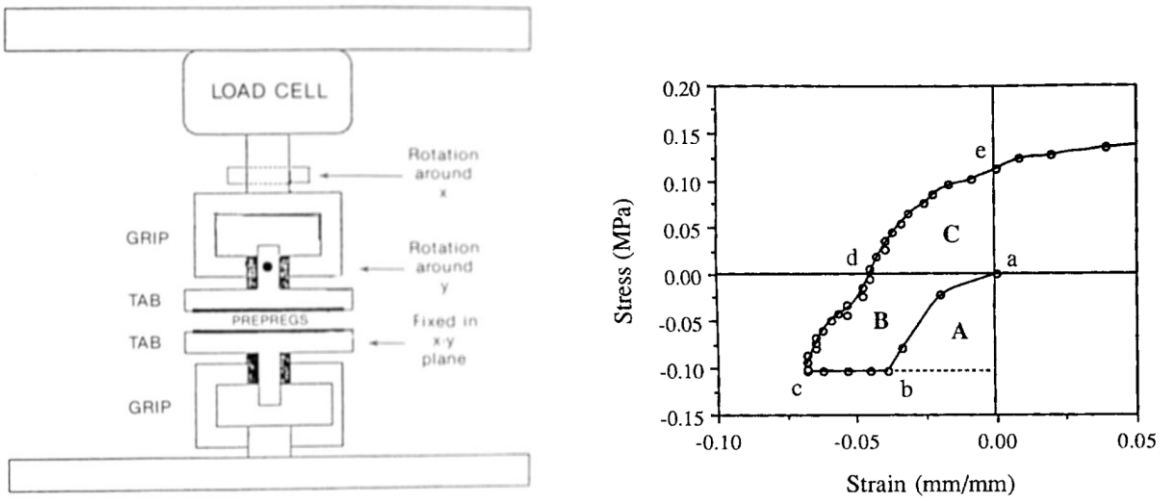

(a) (b)

Figure 2.8 Compression to tension test for prepreg tack.
a. Schematic of the compression to tension test [32]; b. typical stress-strain curve [19].

A dimensionless number namely Compression Tack Index (CTI) is defined as the quantitative value for tack. This index is the ratio the energy outputted from the prepreg stack during tensile unloading (C) to the energy inputted to the prepreg stack during compressive loading (A+B). Considering that after the compression the stack of prepregs form a uniform medium, they were able to develop a viscoelastic model to describe the energies in each stage of the experiment and finally calculate the theoretical value for the CTI.

Gillanders et al. [34] developed a probe test for investigating tack of single plies of prepreg for the first time. Dubois et al. [31] used a more technologically advanced setup which was able to produce more replicable results. The setup was utilized to characterize the tack of prepreg and pure resin. The maximum debonding force was *chosen* as the measure of tack and effects of different

parameters on tack were studied. As it is evident from a comparison between Figure 2.9 and Figure 2.7, the force-displacement response of pure resin is similar to that of PSAs. The primary difference between the two stems from the lack of the fibrillation process in pure resin. Therefore the stress plateau stage during which the PSA fibrils would grow uniaxially while keeping the same stress levels, is replaced with another steep reduction of stress (B-C stage) in the response of pure resin.

For the prepregs, on the other hand, the force-displacement response is dominated and completely changed as a result of structural changes caused by the introduction of fiber reinforcements into the resin. The addition of fibers prevents phenomena such as fibrillation to occur within the bulk of the prepreg. Moreover it alters the surface roughness, and causes resin content to vary from point to point. Consequently, three separate stages that were identified for the detachment phase of the pure resin are replaced with a monolithic reduction of the force in prepreg materials.

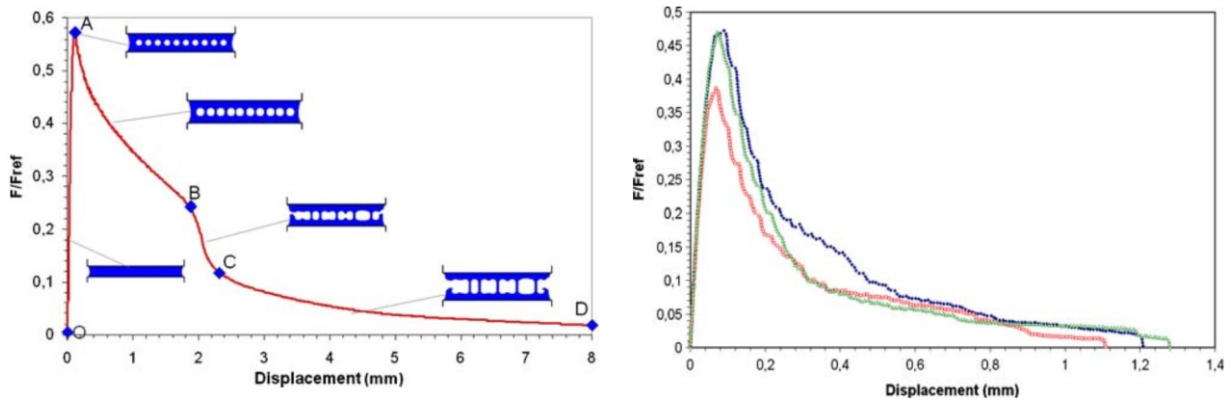

a. pure resin b. Prepreg

Figure 2.9 A typical normalized force vs displacement curve in probe test [31].

They have investigated effects of contact time and pressure, probe temperature and debonding rate on the prepreg tack. A threshold at 30 seconds of contact with 15 N force (over probe of 10 mm in diameter) was reported above which the tack was not dependent on contact time and pressure. These values were used for their remaining analyses to avoid incomplete contact between the

prepreg and probe. Moreover, it was found that an increase in the probe temperature results in lower tack levels. Higher temperature, causes the viscosity of the resin to decrease, hence facilitating the resin to flow away from the probe surface. As a consequence, the resin content at the probe-prepreg interface decreases, thus reducing the maximum debonding force (this could be considered as one of the drawbacks of the probe test). Increasing the debonding rate, on the other hand, increased the debonding force by amplifying the viscoelastic response of the resin.

Wohl et al. [35] developed a specific fixture for performing the probe test inside a rheometer which is capable of providing better control over the experimental factors (especially over relative humidity and temperature). A design of experiment approach was adopted to investigate the multivariate design space. Most observations in their general trends were consistent with those of Dubois. However, a local peak at moderate values of contact force was observed which was attributed to the resin being able to redistribute and flow away from the contact surface with probe. This point can be understood considering the prepreg sample is heated up inside the rheometer, contrary to the local heating of prepreg through the probe in [31]. More interestingly, a peak in tack was observed in intermediate values of relative humidity which was attributed to the viscoelastic properties of the resin.

Some researchers have used the standard floating roller peel fixture (Figure 2.10) to measure the prepreg tack according to ASTM D3167. This standard was initially developed for the measurement of PSA tack, and it has been used as a guide to for obtaining prepreg tack [36, 37]. In this test, the normalized peel force indicates prepreg tack. Banks et al. applied the prepreg to the rigid adherend manually. But, Rao et al. developed a fixture containing a roller for the head of a CNC machine, in order to simulate the AFP process for laying down the prepregs. Hence, conducted a more controlled study.

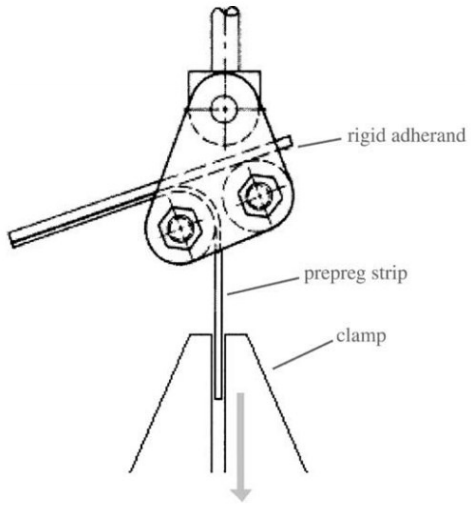

Figure 2.10 Floating roller test fixture.

One of the primary shortcomings of the probe test is the inability of the machines to perform the bonding and debonding stages at rates comparable to the rate of AFP process. In the conventional peel tests, two separate stages of material application and peeling are involved. Consequently, controlled application of prepregs to the adherend plate is challenging. The contact time between the two stages is generally long and hard to control. Furthermore, the final measured peel force in this method consists of different phenomena that are involved in the peel mechanism in addition to the prepreg-adherend interactions. Especially, it should be noted that, in the PSA industry which is the primary application of conventional peel tests, the adhesive is applied on very thin and compliant papers for the testing. Prepregs, on the other hand, have a significant stiffness as a result of the continuous fiber reinforcements. Therefore, bending effects profoundly contribute to the peel resistance of prepregs and the peel force does not solely represent prepreg tack.

Crossley et al. [9, 38] developed a single stage peel test to overcome the drawbacks of previous characterization methods. The schematic of this method is presented in Figure 2.11. The primary difference of this method from conventional peel tests is that in the proposed method, prepreg sheet is bonded to and peeled from the substrate in a *single continuous motion* and *almost simultaneously*. The first two rollers, on the left, provide a guidance for the translational movement of the rigid substrate. The top right roller is fixed and comes into contact with the prepreg. This

roller essentially simulate the prepreg deposition process and at the same time acts as the guide for the 90° (mandrel assisted) peel test. The bottom right roller is loaded with springs. Spring deflection is assigned such that the desired compaction force is obtained between the prepreg and rigid substrate. One end of the prepreg specimen is clamped to the cross-head of a universal testing machine. The cross-head moves vertically, and the vertical movement of the prepreg is translated into horizontal movement of the specimen and the rigid substrate. The force required to perform the experiment is measured through the load cell as a function of the cross-head displacement.

In order to separate effects of the dynamic stiffness, a piece of the backing paper is used in the beginning to cover the tacky surface of prepreg for a part of the experiment. Consequently, the force measured in the first part of the experiment is prepreg's dynamic stiffness (as well as the friction involved in the equipment). For the rest of the experiment, prepreg is directly in contact with the rigid plate. Tack is quantified as the normalized peel force of the second part, after the contributions from the dynamic stiffness and friction are deduced. This value is believed to be analogous to the fracture energy obtained in the probe tack test, since it solely represents tack.

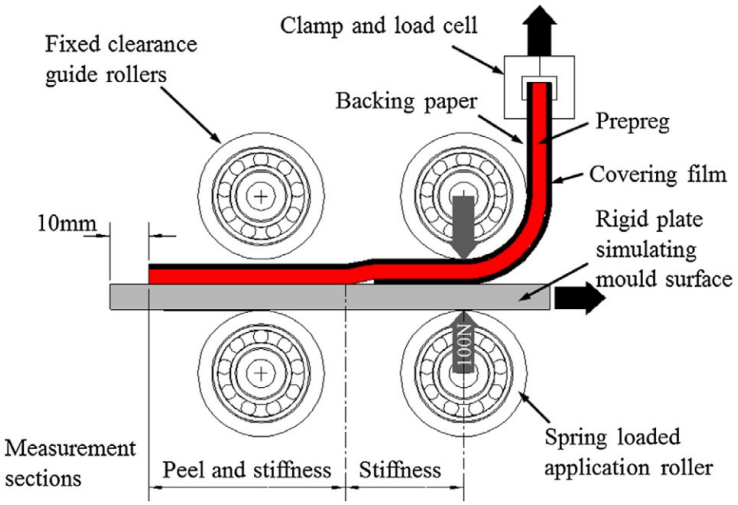

Figure 2.11 Schematic of the single-stage peel test [39].

Using the developed method, Crossley et al. [39] demonstrated that prepreg tack follows the TTS (time-temperature superposition) principle. Moreover, it was shown that constant parameters of the WLF equation (TTS principle) [40] obtained from the small amplitude oscillatory shear of the pure resins can be used to construct the master curves of the peel resistance of prepregs. This is further an evidence of the fact that prepreg tack is highly influenced by the resins viscoelastic properties. The master curves both quantitatively, and in a conceptual or intuitive manner can help in achieving the desired tack levels.

Based on various experiments, two major types of failure were identified (Figure 2.12). At low temperature and high rates of bonding, the peel tack is highly controlled by the surface properties. Therefore, failure is adhesive, which is identified by minimal residual resin on the rigid substrate. On the other hand, at high temperatures and low rates, the prepreg-substrate interface is very strong. Therefore, viscoelastic resin properties control the failure in peel test. This mode of failure can be identified by the formation of fibrils and considerable amount of residual resin after the test (Figure 2.13).

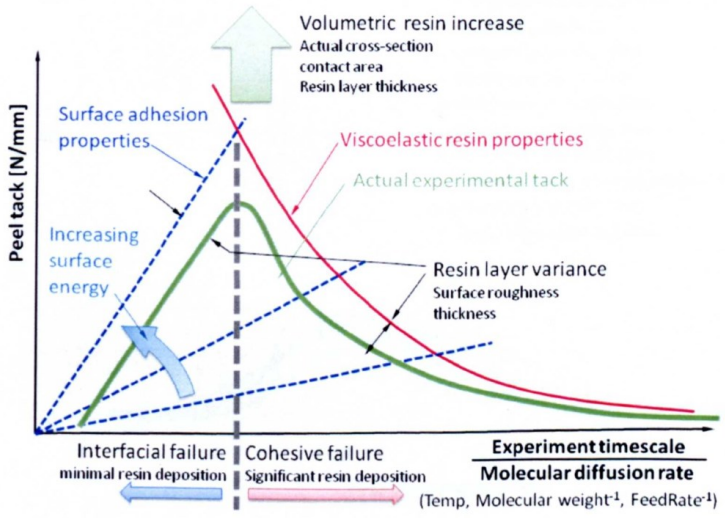

Figure 2.12 Dominant factors in each failure mode of the single stage peel test [9].

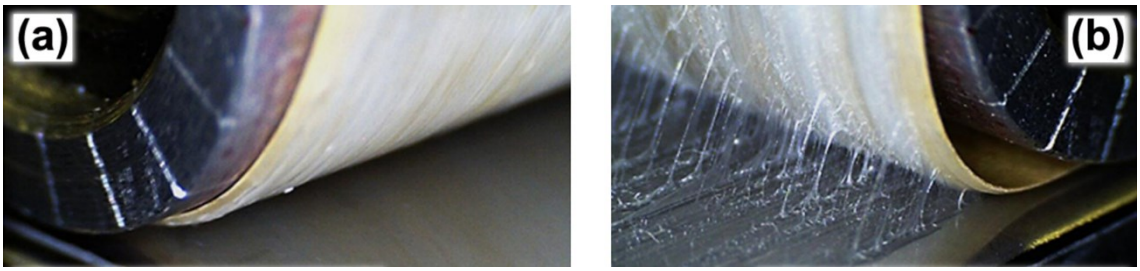

Figure 2.13 Peel test failure modes: (a) adhesive failure; (b) cohesive failure [39].

2.3 PROCESS-INDUCED DEFECTS

Despite AFP's numerous advantages and capabilities that were discussed in 2.1, this technology comes with its own limitations. The productivity of the lamination process and the quality of final parts are significantly influenced by the complexity of the part, as well as the process parameters such as lay-up temperature, speed, compaction force and fiber tension. More importantly, several different defects may appear while using AFP (especially during fiber steering) such as gaps and overlaps between tows, out-of-plane wrinkles and tow pull ups. By creating resin rich areas and deviation in fiber orientation, these defects decrease the part quality and reproducibility [6, 41].

The minimum achievable steering radius of prepreg tow is constrained by the development of defects within individual tows. Number of problems may arise if the defects are not controlled. For instance, it has been pointed out before that most works on the variable stiffness composites consider theoretical optimization of the structure, overlooking the manufacturing realities and constraints. As a result, manufacturability of the available designs in the literature are generally not guaranteed and variable stiffness panels are not being used in major industries [41]. Therefore, gaining a more comprehensive view of the defects that appear in the process and increasing our understanding regarding the fundamental processes governing the defect formation is indispensable for utilizing the full potential AFP technology to manufacture variable stiffness composites as well as laminating traditional parts. In the following, the published literature on these process-induced defects will be presented.

2.3.1 Course Level

Number of issues arise as a result of constructing plies employing steered tows. To completely cover the entire tool surface, several courses shall be laid down. Different strategies including *parallel* and *shifted* methods may be used to attain this objective (Figure 2.14). In the parallel method, each course is laid down such that it exactly follows the edges of the previous course which results in plies with uniform thickness and no gap. However, this method requires smaller steering radii for subsequent courses since with each course the available space becomes narrower. Consequently, parallel method is significantly constrained by the minimum possible steering radius of the AFP head (especially for large structures where more number of courses are required).

The latter strategy is to keep the original (i.e. reference) course's path definition, and merely shift each course with a distance perpendicular to the variation direction. Due to the curvature of the path, the bottom of one course does not line up with the top of the adjacent course at all locations. Therefore, this method results in gaps and overlaps between the courses

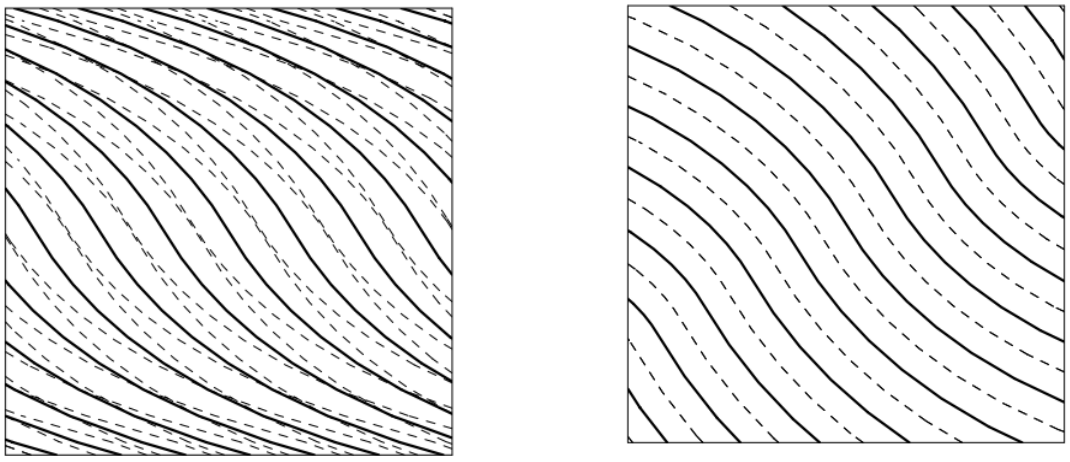

Shifted method

Parallel method (notice the reduction in steering radius from middle to the sides.)

Figure 2.14 Strategies to construct plies employing steered tows [42].

Within the shifted strategy, the individual tow cutting and restarting capability of the machine can be used to eliminate overlaps (i.e. 0% coverage, tow-drop method) or to allow overlaps to some extent, $0\% < \text{coverage} \leq 100\%$, which is known as tow-overlap method. The overlap method causes inhomogeneity in the thickness of the part. Staggering technique, can be used to smoothen the overlaps or spread out the irregularities of thickness. In this technique, plies with the same orientation are shifted with respect to each other so that gaps and overlaps between the courses do not occur in the same plane [43, 44]. In addition, various studies have used different modeling and experimental approaches to investigate effects of gaps and overlaps resulted from each of the described manufacturing techniques on the quality of the final part properties (see for e.g. [45-47]).

2.3.2 Individual Tow Level

Number of different defects appear within steered prepreg tows, however, they are not well documented in the literature. Two types of defects that are recognized in the literature are wrinkles and in-plane fiber waviness at the inside edge of the steered tows, both of which will be reviewed, in the following.

2.3.2.1 In-plane Fiber Waviness

Figure 2.15 (a) demonstrates three courses that are produced by the concept of parallel method. As the tows move towards outer radii, steering radius increases. Moreover, it is clear in the steered section that within each tow, there is a difference in length between a tow's edges due to bending. Consequently, the fibers should microbuckle at the inside edge to accommodate the excessive fiber length that is available in the inner side of the tows.

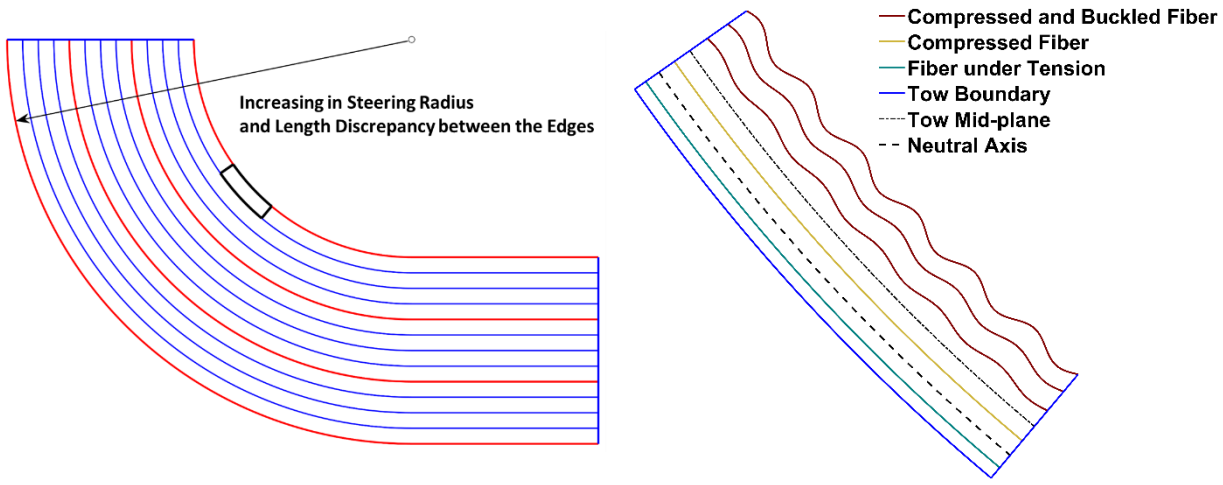

a. Three courses (borders indicated with red lines), each containing four tows (blue lines), are constructed via parallel method.

b. Idealized model of in-plane waviness for the bolded region.

Figure 2.15 Steering prepreg tows and in-plane fiber waviness.

As a result of the manufacturing process of prepregs, the fibers inside prepreg tows are not strictly straight, rather, they inherently possess some degree of waviness. In order to produce mathematical models that can reasonably predict the degree of fiber waviness and subsequently, mechanical properties of a part containing fiber waviness, an idealized condition is assumed. In the idealized models, the fibers are initially straight, then, buckle under the compressive load induced as a result of tow steering.

The phenomenon of fiber microbuckling has been extensively studied (for example [48-50]) since it is very common in composites with a highly compliant matrix phase (such as elastic memory composites). In the context of present work, epoxy resin is mostly used in the aerospace-grade prepregs. Although epoxy is relatively stiff post-cure and in the working conditions, as a b-stage material and in the relatively elevated temperatures of AFP process it exhibits a rather compliant behavior. Consequently, the soft matrix allows the fibers to microbuckle without breaking. This process acts as a stress relief mechanism during tow steering, and allows the material to reach high curvatures during the process.

A mathematical treatment of the in-plane fiber waviness formation is presented based on the work of Hörmann [51]. In this works energy arguments are developed based on Kirchhoff-love beam theory to describe the deformation of fibers. When a prepreg tow with ideally straight fibers is steered, three regions are formed in an arbitrary section of the steered tow. Fibers that are initially under compression (from the inner edge to the mid-plane of the tow, which *at the time* is the neutral axis) microbuckle and form the region 3. At the outer edge, fibers are under tension and consequently remain straight (region 1). A small segment develops between the two regions (i.e. region 2) in which fibers are under compression. However, the compressive stress is not high enough to cause microbuckling of fibers (see Figure 2.15 (b)). Region 2 is the small part between the actual neutral axis of the tow, where the strains are equal to zero, and its mid-plane. In a tow with microbuckled fibers, the neutral axis and mid-plane do not coincide. The reason is that when the fibers microbuckle they *lose* their stiffness. Therefore, the outer side of the steered tow has higher stiffness, which causes the neutral axis to shift towards the outer edge.

Concept of Representative Volume Element (RVE) is used to develop energies. For the first and second regions where the fibers are under tension or compression without any buckling, the Kirchhoff-love beam theory provides the elastic energy stored as a result of bending W_{Be}^{i}:

$$W_{Be}^{i} = \frac{1}{2} E_1 \left(\frac{1}{12} \xi \, h_i^3 + \xi \, h_i \, d_i^2 \right) l_i \, \kappa_{NA}^2 \tag{2.1}$$

In this equation, E_1 is the longitudinal elastic modulus of the prepreg, ξ is the prepreg thickness (equal to that of any RVE), d_i is the distance of *i-th* RVE from the neutral axis, l_i is the length of RVE, κ_{NA} is the curvature of the neutral axis (which is equal to the inverse of steering radius) and finally h_i is the width of the *i-th* RVE. In the first and second regions this is the same as the width of the respective regions. Since the fibers are able to maintain their integrity, their stiffness is much higher than the stiffness of matrix. Consequently, the tensile and compressive energies stored inside the matrix of these regions can be neglected.

For the third region, buckled fibers of the *i-th* region are assumed to take the following sinusoidal shape $y_i = a_i \sin(\pi \, x_i / \lambda_i)$ where a_i is the amplitude of the buckled fiber and λ_i is half its wavelength (see Figure 2.16). Moreover, the length of RVEs is considered to be one full wave of a buckled fiber ($l_i = 2\lambda_i$) and the width is considered to be twice the amplitude of the buckled fibers ($h_i = 2a_i$). Therefore, as many RVEs as required should be used until the whole width of the region is covered.

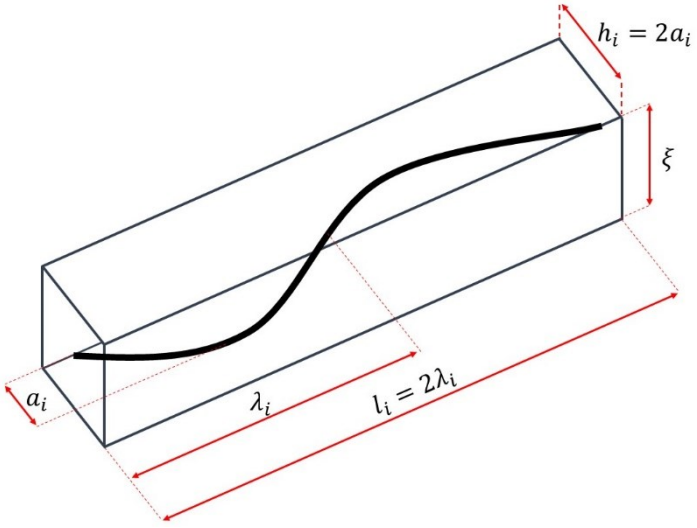

Figure 2.16 Geometry of the *i-th* representative volume element (RVE).

When the fibers microbuckle, they loose their stiffness. Therefore, it is important to consider the energy stored inside the matrix in addition to the energy stored in the buckled fiber. Fiber microbuckling can subject the resin to either tension or shear loading (Figure 2.17). If the fibers buckle in phase, the resin will be subjected to shear. On the other hand, if the fibers buckle out of phase the resin will be subjected to extension. Rosen [52] demonstrated that the shear mode is the one requiring lower energy levels.

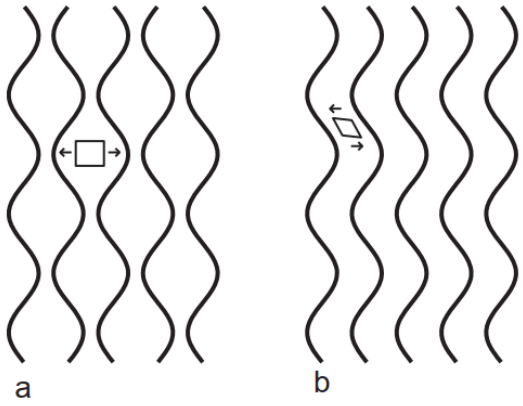

Figure 2.17 Resin deformation under fiber microbuckling [50].
a. Extension mode; b. Shear mode.

The energy required for the fibers to bend into the sinusoidal microbuckled form, per unit area is $w_{F,Bu}^{i}$:

$$w_{F,Bu}^{i} = \frac{1}{2}\frac{V_F}{\pi\, R_F^2}\int_0^{l_i} E_F\, I_F\, \frac{\partial^2 y_i}{\partial x_i^2}\, dx_i \tag{2.2}$$

where R_F, V_F, E_F and I_F are, respectively, radius, volume fraction, elastic modulus and second moment of area of a fiber. Substituting, the second differentiation of the deformation, and integrating $w_{F,Bu}^{i}$ over the dimensions of an arbitrary RVE, results in the strain energy of the buckled fiber:

$$W_{F,Bu}^{i} = \frac{1}{4}\frac{\pi^3\, E_F\, I_F\, V_F}{R_F^2}\frac{a_i^2}{\lambda_i^4}\, l_i\, \xi\, h_i \tag{2.3}$$

For the sheared matrix, the strain energy reads:

$$W_{Sh}^{i} = \frac{1}{2} \iiint_{RVE_i \; volume, \Omega_i} G_{xy} \; \varepsilon_{xy,i} \; d\Omega_i \tag{2.4}$$

The deformation of fibers is governing the deformation of the resin. Consequently, by differentiating the sinusoidal shape, the shear strain of the matrix is found. Finally, the strain energy stored inside the matrix is found by calculating the integration over the volume of a RVE.

$$W_{Sh}^{i} = \frac{1}{4} \; G_{xy} \left(\frac{\pi \; a_i}{\lambda_i}\right)^2 \; l_i \; \xi \; h_i \tag{2.5}$$

The total strain energy of a buckled RVE (inside region three), is comprised of the energy of a buckled fiber and sheared matrix: $W_{Bu}^{i} = W_{F,Bu}^{i} + \; W_{Sh}^{i}$. As many representative volume elements as required should be used to cover the whole width of a region. Finally, the total energy inside the tow, W_{total}, is obtained.

$$W_{total} = \sum_{i=1}^{n_{R_1}} W_{Be}^{i} + \sum_{i=1}^{n_{R_2}} W_{Be}^{i} + \sum_{i=1}^{n_{R_3}} W_{Bu}^{i} \tag{2.6}$$

In this equation, n_{R_1}, n_{R_2} and n_{R_3} are the number of RVEs required. The total energy should be minimized to obtain the degree of fiber waviness (amplitude over wavelength of waviness) and *position of the neutral axis* of steered tow.

2.3.2.2 Out-of-plane Wrinkles

The other type of defect that has been considerably studied is the out-of-plane wrinkle. One of the main challenges in the steering of tows are the out-of-plane buckling at the inside edge of the prepreg tow, which significantly constrain the minimum possible steering radius. The length discrepancy between the inside and outside edges of the steered tow results in a compressive force at the tow's inside edge. If the steering curvature is higher than a critical curvature, the compressive force at the inside edges surpasses the critical buckling load of the representative plate and the out-of-plane wrinkles form in the tow, accordingly.

Based on visual examinations, Negendra [53] suggested the minimum steering radius of 635 mm for 3.2 mm wide tows to avoid local fiber buckling. This value has been often used in the literature as the criteria for minimum steering radius [41] and has also been recommended by AFP manufacturers [54, 55]. In another attempt, Wiehn and Hale [56] successfully steered the tows with the minimum radius of 508 mm.

Smith et al. [57] optimized the AFP process parameters to obtain the minimum achievable defect-free steering radius (critical radius). They reported the minimum radii of 1250 and 500 mm for 6.35 and 3.2 mm tows, respectively. The critical buckling radius has also been implemented as an index to predict the layup quality over complex geometries [58]. Zhao et al. experimentally investigated the influence of different process parameters on the critical buckling radius. They reported that good layup quality is achievable when the trajectory's geodesic radius is larger than the critical buckling radius.

It has been widely acknowledged that the prepreg tack, which exhibits time-dependent viscoelastic behaviors, significantly affect the critical radius for having a wrinkle-free layup; hence, controls the tow's ability to be successfully laid up [31, 58]. Problems that arise during the AFP as a result of the inappropriate tack levels are frequently tackled by experimenting with process parameters such as lay-up temperature, lay-up speed and compaction load. Such trial and error methods are time-consuming, expensive and result in material wastage [37]. Since tack levels significantly alter as a function of process parameters, proposing a general, experimentally defined value for the critical radius may not be adequate for thoroughly understanding the defect formation processes and possibly finding means to avoid them. Consequently, in addition to experimental investigations, modelling approaches are crucial to gain a deeper understanding of the problem, as also pointed out by Lukaszewicz [6].

Available Models [59-61] utilize a local approach for representing wrinkles. The overall view of the progression of local models is presented here. However, the details of the models are not discussed since a more general model is developed in section 4.1 of the present study and the preceding models are obtained as a simplified version of the new model.

In general, the local modeling approach considers the formation of individual wrinkles to be the buckling of a plate which is resting on an elastic foundation and is subjected to in-plane loading

conditions. The plate represents the prepreg tow and it is described using orthotropic elastic material properties. Different *elastic* foundation models have been used to represent the prepreg tack, or the prepreg-tool interface. In practice, the material system as well as the process parameters used in the process, determine the mechanical properties of the foundation model. The critical buckling load of the representative plate can be related to a "critical steering radius" which describes the minimum steering radius required for the prepreg tow to be free of wrinkles. Moreover, if the steering radius is smaller than the critical value, the length of the plate can be calculated from the models which would be the wavelength of the wrinkles for that specific set of process parameters and material system.

Beakou [59] considered the representative plate to be resting on *independent spring elements* (i.e. Winkler foundation). The plate's boundary conditions consisted of a free edge, at which the buckling occurs, and three simply supported edges (SSSF plate). Matveev [60] improved the previous model by introducing, the more realistic, clamped boundary conditions for the lateral edges of the plate (CCSF plate). By providing more support, the clamped boundaries produce a better estimate of the real process (Figure 2.18). Furthermore, Matveev et al., for the first time, provided experimental evidence from AFP trials that the local model is capable of predicting the critical steering radius and wrinkle wavelength (wavelength is the length of prepreg tow divided by the number of appeared wrinkles). Recently, Belhaj and Hojjati [61] introduced a shear layer between the spring elements and the plate (i.e. Pasternak foundation). It was experimentally demonstrated that considering a level of interaction equivalent to the shear modulus of the prepreg, considerably enhances the model's accuracy.

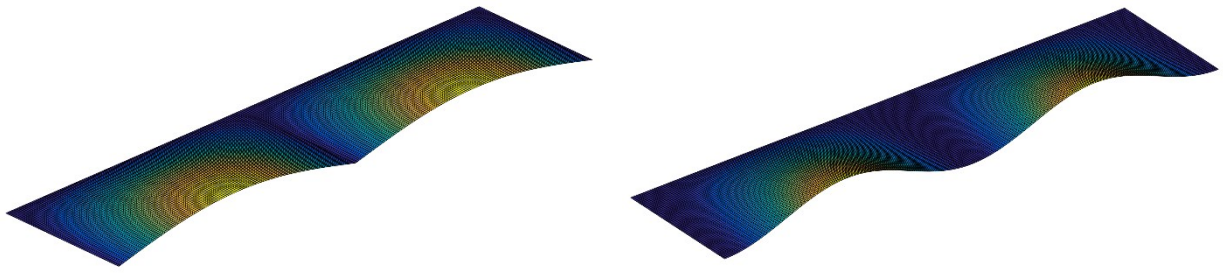

SSSF Plate CCSF Plate

Figure 2.18 Influence of the boundary conditions on the models of wrinkle formation.

It should also be noted that the prepreg deposition method substantially affects the residual stresses in the laid down tow. Conventional AFP heads incrementally form the steering radius by forcing the tow to follow the prescribed trajectory, hence, bending the tows. Alternative forming mechanisms such as Continues Tow Shearing [62] could be helpful in reducing process-induced defects. CTS, as an example, helps in steering the tow by changing the primary mode of deformation from in-plane bending of the prepreg tow to in-plane shear deformation (Figure 2.19).

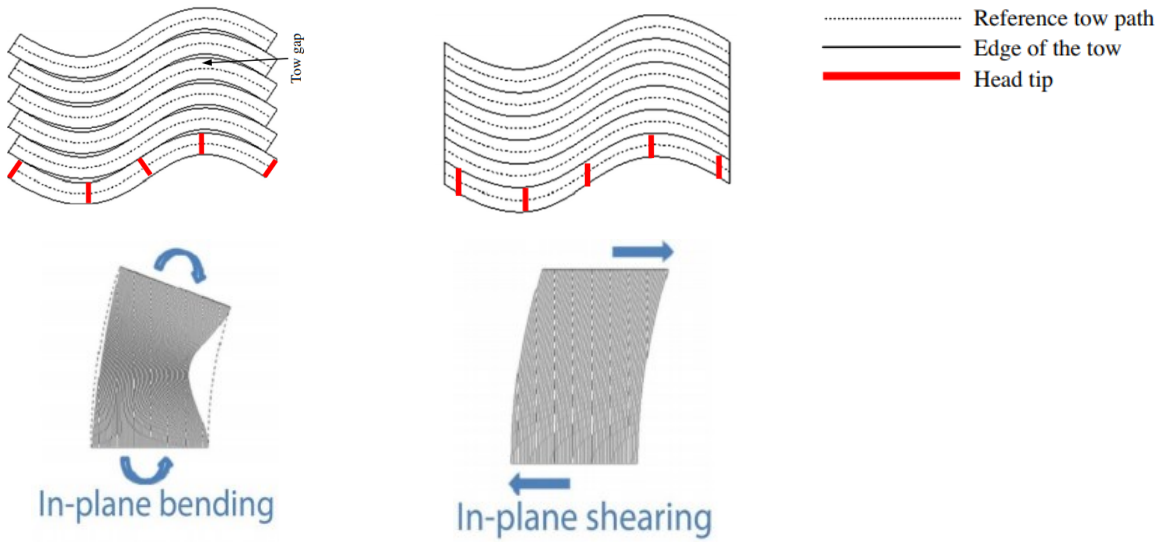

Figure 2.19 Comparison between CTS and conventional head: deformation mode and resulting layup.

3 EXPERIMENTAL OBSERVATIONS

3.1 METHODOLOGY

The machine used for performing the AFP trials is the XTP-500 supplied by Automated Dynamics and is depicted in Figure 3.1. This machine has six degrees of freedom and with the appropriate head, it can layup both thermoset and thermoplastic composite materials. The head used here, which can be seen in Figure 3.1, delivers up to 4 tows with individual tow width of 6.35 mm. The individual tows can be started and cut at any time during the tow deposition in order to increase or decrease the width of the course and to produce openings in the laminate. The heating mechanism in this head consists of hot Nitrogen gas with controllable temperature and flow rate. The nozzle which delivers the hot gas is directed at the tool surface. As a result, it indirectly warms up the prepreg, which in turn increases the prepreg tack.

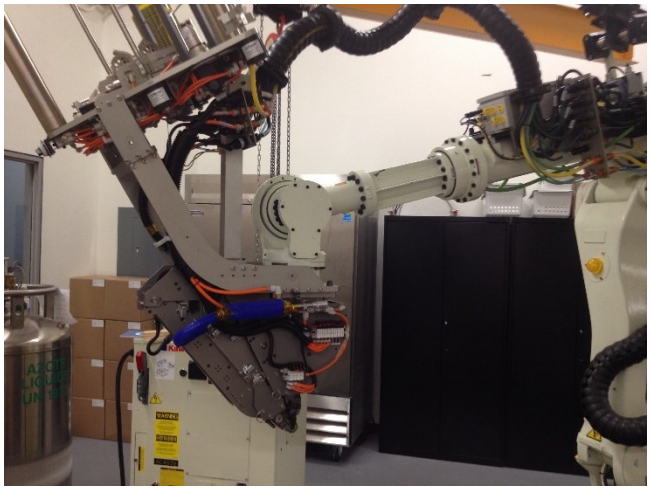

Figure 3.1 The XTP-500 machine used for performing AFP trials.

An important component of every AFP machine is the compaction roller. The key responsibility of the compaction rollers is to provide an even and controlled amount of pressure on the prepreg tow/tape which is being laid down, in order to consolidate the prepregs, reduce surface

irregularities and trapped air between the plies. Strategies devised to maintain the even pressure include those involving different shapes and structure of the roller, and those involving adaptive mechanisms connecting independent segmented rollers. The roller used in the preset study (Figure 3.2) is comprised of a perforated flexible polyurethane rubber. The holes in the architecture of the rubber, help it to deform uniformly over complex tools, hence proving a good and relatively even pressure distribution over the whole surface covered by the roller.

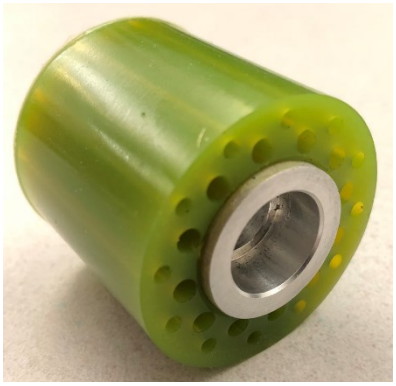

Figure 3.2 The standard compaction roller of XTP-500.

The material system used here was aged 6.35 mm (1/4 in) 977-2/35-12K HTS-145 unidirectional prepreg. In this material system, 12K of high-strength grade carbon fibers (HTS-145) are impregnated in the CYCOM 977-2 epoxy resin system which is designed for autoclave curing or press molding [63]. The prepreg fiber weight fraction prior to cure is 35% and the prepreg thickness (ξ) was measured and found to be 0.2 mm.

During the experiments, steering radius, layup speed, compaction force, Nitrogen temperature and flow rate were altered to identify their complex and intertwined effects on the steered tow quality and specifically and different defects that appeared in the steered tows. Before the layup process, the material was kept at room temperature for 30 minutes. Then, it was directly mounted on the cardboard bobbins (spools) to be steered on the Aluminum tool. Before each trial, the tool was cleaned with acetone to ensure that there is no residual resin or oil on the Aluminum tool surface that might affect the strength of the prepreg/tool interface.

For this section, the prepreg tows were steered in the range of 558.8-2032 mm (22-80 in) radius, the head speed was between 50 and 140 mm/s, the compaction force was between 111-311 N (25-70 lb), the Nitrogen temperature was 210-270 °C and Nitrogen flow rate was 75-100 lit/s.

Major experimental findings regarding the lay-up defects in steered tows are presented in the next section.

3.2 EXPERIMENTAL OBSERVATIONS [64]

A total of 60 AFP trials were performed with different process parameters and steering radii. It was aimed to first, gain a more comprehensive understanding of the steered tow quality, types of defects and the various parameters that affect the quality. Second, to use the experimental results to verify the accuracy of the models that will be developed later in this study.

As a result of viscoelastic behavior of the resin, prepregs exhibit time-dependent behavior which in turn derives the growth of defects with time. While section 3.2.1 presents the defects in steered tows, section 3.2.2 is dedicated to the time-dependent growth of wrinkles.

3.2.1 Defects in Steered Tows

Experimenting with different process parameters, five major types of defects namely fiber waviness, sheared fibers, tow pull ups, blisters, and wrinkles were identified in the steered tows. Seven sample cases with the resulting defect types are presented in Table 3.1. Since different defects may simultaneously occur in the steered tows (e.g. in-plane fiber waviness occurs, to some degree, in all cases), the most prominent defect type is reported for each case. It is worthwhile to mention that each of the configurations, which contained a significant trend, were performed twice to ensure the existence of the patterns.

Table 3.1 Process Parameters and resulting Layup quality.

Case #	Steering Radius (mm)	Nitrogen Gas		Head Speed (mm/s)	Compaction Force (N)	Defect Type	Sample Picture
		Temperature (°C)	Flow Rate (lit/s)				
1	889	250	75	114	222.4	No defect	Fig. 3.3
2	635	220	100	88	266.9	In-plane waviness	Fig. 3.4
3	635	220	100	76	266.9	Sheared fiber	Fig. 3.5
4	558.8	250	75	114	311.4	Tow pull up	Fig. 3.6
5	558.8	250	75	114	222.4	Wrinkle and blister	Fig. 3.7
6	558.8	260	85	140	222.4		
7	558.8	250	75	114	111.2	Did not stick	-

In the first case presented here, the tow is steered with the radius of 889 mm (35 in). The appropriate process parameters in conjunction with relatively large steering radius result in a very good quality, with a very slight degree of fiber waviness. The picture of the sample is presented in Figure 3.3.

Figure 3.3 889 mm steering radius: No significant defect is observable.

The most primitive result of length discrepancies between the inside and outside edges of a steered tow is the formation of in-plane fiber waviness at the inside edge of the tow (Figure 3.4), to

compensate for the excessive fiber length (in comparison with the prescribed fiber path). Since the process temperature is increased to achieve appropriate tack levels, the resin viscosity is decreased. Consequently, the fibers can elastically micro-buckle under compression and form a sinusoidal shape. It has been shown that in-plane fiber waviness remains throughout the autoclave process. Moreover, both theoretical models and experimental investigations demonstrate that they can impact the mechanical properties of the final part [51]. As such, depending on the overall design requirements, the tolerable degree of fiber waviness should be defined prior to the manufacturing of the parts.

It is also interesting to notice the pattern of fiber microbuckling as one moves from the inner edge towards the outer edge of the tow. The buckling has clearly occurred in-phase. Which confirms that the in phase microbuckling (shear deformation of resin) has lower energy levels compared to the out of phase microbuckling (extension of resin), hence naturally takes place in the process.

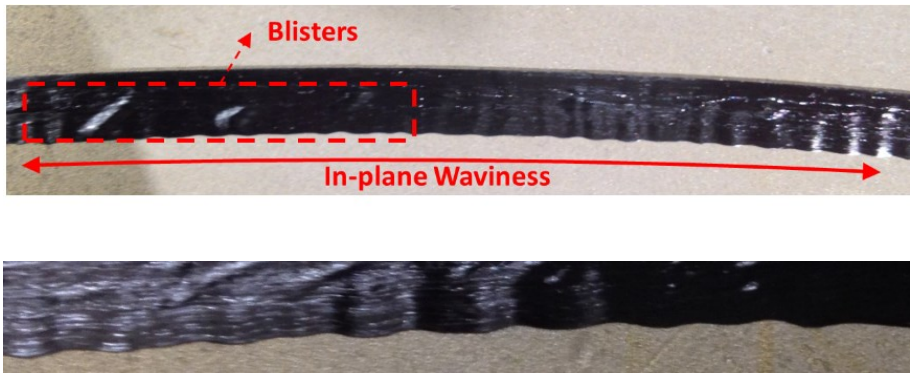

Figure 3.4 Blisters and in-plane fiber waviness are appeared in the steered tow.

It was found that having a relatively too high temperature and too low speed at the same time does not result in a perfect layup quality. The low viscosity of the resin and the low speed would give the fibers the opportunity to slightly deviate from the prescribed curvilinear path and cause shearing in the resin and fibers, which consequently, results in a poor overall quality. It was found that these sheared fibers which are demonstrated in Figure 3.5, could be resolved by slightly increasing the speed or decreasing the temperature. For instance, by increasing the speed in case

2, the sheared fiber problem of case 3 is refined. This suggests that at a given temperature, a certain velocity is required to allow for the fiber microbuckling.

Figure 3.5 Sheared fibers.

Tow pull up or the bridging of the tow at the outside edge is another process induced defect (Figure 3.6). The steering produces a tensile stress at the outside edge of the tow. If the tensile stress is higher than what the prepreg tack can support, the tow bridges to reach lower energy levels.

Figure 3.6 Tow pull up.

Compaction force was found to be most influential on the appearance of tow pull ups. Note that the only difference between the cases 4, 5 and 7 is in the amount of compaction pressure applied

to the tow. Low compaction force does not provide the intimate contact required for achieving the adequate tack levels. Therefore, low compaction force causes the tow to bridge (or does not stick at all). On the other hand, too high compaction force makes the prepreg resin to excessively stretch during the deposition process. After the load is released (compaction roller is passed), the resin wants to contract which causes the shear contribution of the mixed mode failure occurring at the interface to increase, and therefore, the tow bridges again (Figure 3.7). For the material system in the present study, the optimum compaction force was found to be in the proximity of 222.4 N.

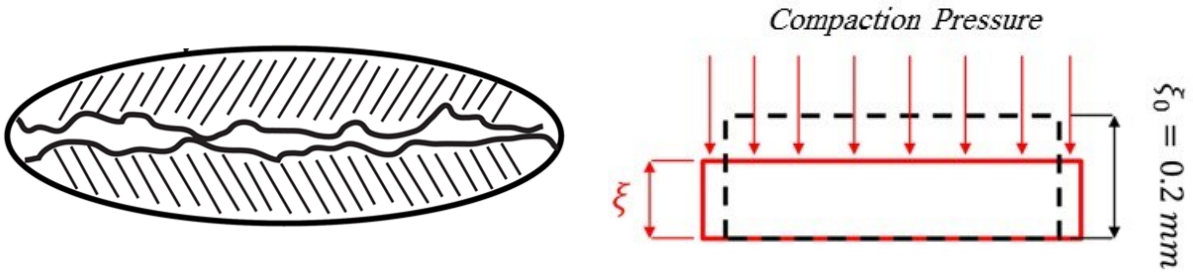

a. Low compaction force: intimate contact is not achieved.

b. Too high compaction force, causes redistribution of resin content and change in the mode of failure.

Figure 3.7 Effect of compaction roller on tow pull-ups.

Very commonplace type of defects formed during tow steering is the out-of-plane wrinkles at the inside edge of the prepreg tow, and blisters at the middle of the tow-width (Figure 3.8). As discussed earlier, for a given set of process parameters, as the steering radius decreases, the compressive stress at the inside edge of the prepreg tow increases. This causes the fibers at the inside edge of the tow to micro-buckle in order to accommodate the excessive length of fiber and release some of the strain energy stored in the compressed fibers (in-plane fiber waviness formation). As the steering radius decreases, the in-plane buckling mechanism will be insufficient as lower energy levels through out-of-plane buckling of the prepreg tow become available. Consequently, prepreg tow buckles out of its plane and locally, which causes the appearance of wrinkles in the layup. In this regard, in-plane buckling is considered to be the precursor to the out-of-plane buckling. Generally, a critical steering radius exists at which the prepreg tack cannot

support the compressed fibers and maintain them on the tool surface anymore and out-of-plane buckling occurs to drop the excessive amounts of the stored internal energy.

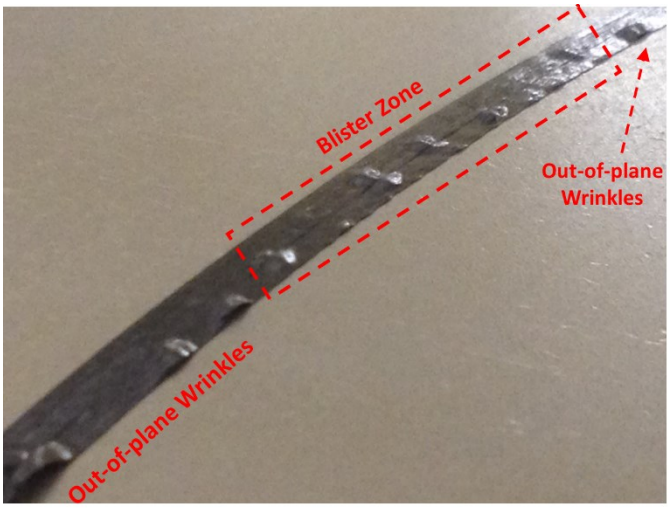

Figure 3.8 Wrinkles and blisters at 558.8 mm steering radius.

The last type of defect that will be discussed here is blister. Initially, it was postulated that the blisters are appearing due to the high flow rate of the hot Nitrogen gas (case 6). However, decreasing the flow rate (case 5) proved to be ineffective in preventing their formation. It will be demonstrated in section 5 that the blisters are originating as a result of a damaged interface and pressure differences resulted from the architecture of the roller. The formation of blisters and wrinkles will be further discussed in the remaining of the thesis. In addition to the contribution of mechanical stresses induced from steering, influence of other factors such as the compaction roller will be investigated later. Appropriate process parameters should be determined for steering the fibers with the desired radius to avoid the prevalent process induced defects during steering.

3.2.2 Time-dependent Growth of Wrinkles [65]

As mentioned before, prepreg tack is a product of prepreg-tool interaction, and is highly influenced by prepreg's resin properties. Viscoelastic properties of the resin causes stress relaxation effects to take place during the process and hence, different defects may grow with time. In the present section, a deeper investigation is conducted in order to demonstrate this fact. The process parameters tabulated in Table 3.2 were identified in the trial and error performed in section 3.2.1. For the material system used during the present studies (the same as the previous section), these parameters could best highlight the viscoelastic nature of the prepreg tack.

Table 3.2 AFP process conditions for having time-dependent growth of wrinkles.

Steering radius (mm)	Nitrogen gas (HGT heating system)		Head Speed (mm/s)	Compaction Force (N)
	Temperature (°C)	Flow Rate (lit/s)		
558.8	260	85	140	222.4

Prepreg was deposited with the reported process parameters four times to ensure the reproducibility of the results. An arbitrary section of the tow was chosen for detailed measurement of the wrinkle length, as shown in Figure 3.9. A camera was set to take pictures at 5 seconds intervals; the first picture being taken immediately after the compaction roller had laid down the prepreg tow. Figure 3.10, shows some of the results for a single layup at different times. Clearly, the wrinkle is growing with time. The length of the wrinkles were measured from the pictures and will be later used for corroborating the developed models.

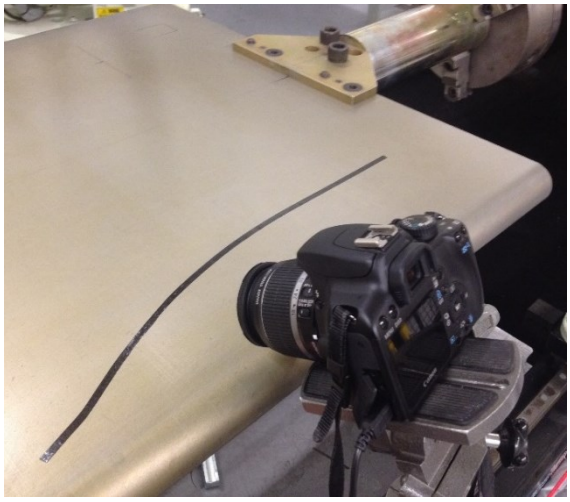

Figure 3.9 The experimental setup for the time-dependent growth of wrinkles.

t = 0 (sec)

t = 5 (sec)

t = 15 (sec)

t = 25 (sec)

t = 40 (sec)

Figure 3.10 An example of time-dependent growth of a wrinkle at t = 0, 5, 15, 25 and 40 (seconds).

4 DEFECT MODELING

Different prepreg material systems along with different process conditions produce too many variables for experimental identification of appropriate AFP process conditions. For a particular material system, usually, trial and error with various process parameters should be used to find the most appropriate layup quality for a given steering radius. This process is obviously, very expensive and time-consuming since it requires numerous trials, it is labor intensive and causes substantial amount of material wastage. Consequently, it is indispensable to explore alternative theoretical and simulative modeling approaches in order to limit the searching space.

Among various defects that appear in the Automated Fiber Placement, especially during tow steering, in-plane fiber waviness and wrinkles at the inside edge of the tows have been theoretically studied before. This might be in part due to the high frequency of appearance of these defects and more straightforward methods that can be implemented to model them. In this section, first a novel time-dependent local model that accounts for the viscoelastic nature of prepreg tack is developed. Previously available local models are subsequently derived as especial cases of the more general model that was presented as a part of the study. Furthermore, a new global simulation framework is developed in order to simulate the whole prepreg deposition process in order to capture the wrinkles and blisters that may appear in prepreg tows during tow steering in AFP.

4.1 LOCAL MODELING APPROACH [65]

As discussed in the previous chapters, it is very well established that the prepreg tack exhibits time-dependent viscoelastic behavior. However, all of the available models (see section 2.3.2) treat the defect formation problem as the buckling of an *elastic plate* resting on an *elastic foundation* (which represents the interface or prepreg tack). Indeed, it has been pointed out [6] that one reason for inconsistencies between the theoretical models and AFP experiments is the inability of the models to account for the viscoelastic material behavior.

Out-of-plane wrinkles appearing at the inside edge of the prepreg tows are one of the major defects that occur during the tow steering in AFP. In this section a more general, time-dependent model in the context of local modeling approach is presented as a theoretical model accounting for these

wrinkles. Succinctly, the local modeling approach takes advantage of the incremental deposition of prepregs during the AFP process, to consider each wrinkle individually. Hence allowing the wrinkle formation process to be considered the buckling of an orthotropic plate, representing the prepreg tow, which is resting on a foundation (representing the prepreg/too interface, i.e. prepreg tack). Subsequently, the critical buckling load of the representative plate can be related to the minimum achievable defect-free steering radius, or when the steering radius is smaller than the critical radius, it can shed light into the frequency of appearance of wrinkles. Details regarding the fundamental assumptions of this method will be discussed in section 4.1.3.

In the remaining of this section, first, different available approaches for introducing viscoelasticity to elastic problems are presented with application to the problem of *time-dependent buckling*. Subsequently, model assumptions are discussed and the model is developed.

4.1.1 Viscoelasticity

Generally, two different approaches for introducing viscoelastic effects into the boundary value problems of the theory of elasticity are available [66]. The first approach, which helps visualizing the molecular structure of the material, uses spring and dashpot mechanical analogs for incorporating the rate-dependent effects into the model. In this method, Newtonian dashpots can be added to the regular elastic material representation, which is a Hookean spring, in various different configurations to represent the stress-strain and stress-strain rate relationships in a viscoelastic medium. Three typical cases of this approach are presented in Figure 4.1. In this figure, (a) is the most general form of linear viscoelasticity which is called Wiechert model. (b) is the Kelvin-Voigt model which consists of a spring and a dashpot connected in parallel. This model can be used to demonstrate the creep behavior of polymers. Finally, (c) is the Maxwell model consisting of a spring and a dashpot connected in series which can be used to represent *uncrosslinked* polymers. It is worthwhile to mention that the Maxwell model in parallel with a spring is called the standard solid model (i.e. Wiechert model with $j = 1$) which is the simplest model that can describe both creep and stress relaxation of viscoelastic materials.

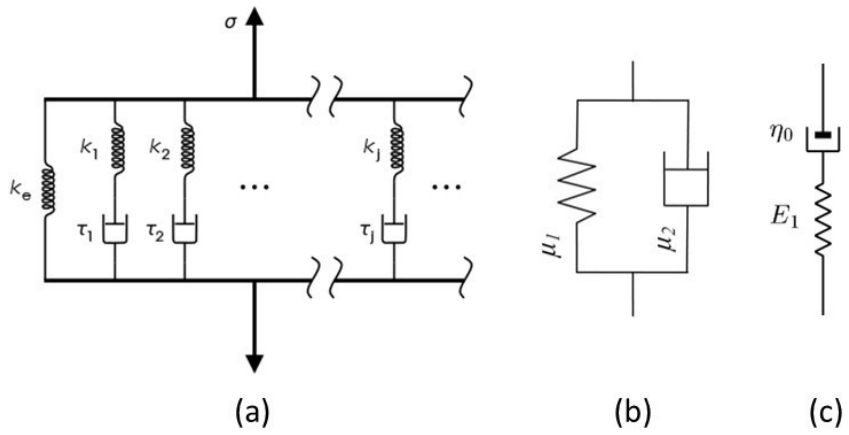

Figure 4.1 Graphical representations of viscoelastic mediums:
(a) Wiechert model; (b) Kelvin-Voigt model; (c) Maxwell model.

In a one-dimensional stress relaxation test, the coupon is subjected to a sudden strain and while keeping the strain constant, the stress response is measured. The initial state of stress is due to the elastic and viscoelastic response of the material. Subsequently, the stress relaxes with time due to the viscous effects. Prony series is a general equation that can be fitted to stress vs. time data (corresponds to the Wiechert model).

$$\mathrm{k(t)} = k_\infty + \sum_{i=1}^{N} k_i \exp(-t/\tau_i) \tag{4.1}$$

In equation (4.1), k_∞ is the long term modulus of the material once it is fully relaxed. t is time and τ_i are the relaxation times of the material, the larger they are, the longer it takes for the viscous effects to take place and relax the stress. k_∞, k_i and τ_i should be fitted to the data to minimize error. It follows from the equation that the initial response of the material is $k_0 = k_\infty + \Sigma k_i$.

This method of representing viscoelasticity is interesting and straightforward in that they demonstrate a schematic representation of the molecular structure. Furthermore, it is fairly easy to obtain governing equations of a problem using relative methods that are used in the theory of elasticity. A review of the different viscoelastic foundations that utilize similar representations is provided by Kerr [67].

The second approach is to use the constitutive integral relations for a linear viscoelastic material. The convolution-like integrals account for the *history dependency* of the stress/strain at any arbitrary time. This can be achieved by using the Stieltjes integrals.

$$\sigma_{ij} = \int_0^t R_{ijkl}(t-\vartheta)\, d\varepsilon_{kl}(\vartheta) \equiv R_{ijkl} * d\varepsilon_{kl} \tag{4.2}$$

$$\varepsilon_{ij} = \int_0^t \Pi_{ijkl}(t-\vartheta)\, d\sigma_{kl}(\vartheta) \equiv \Pi_{ijkl} * d\sigma_{kl} \tag{4.3}$$

In equations (4.2) and (4.3), σ_{ij} and ε_{ij} are respectively, the components of the second order tensors of stress and strain, R_{ijkl} and Π_{ijkl} are respectively, the components of the fourth order tensors of anisotropic stress relaxation and creep. t is time and ϑ is the integral's dummy variable. The integrals are denoted by $*$ operator. It should be noted that in a viscoelastic material $R \neq 1/\Pi$, hence, the operators are treated using $1/\Pi \rightarrow R$ and $1/\mathrm{R} \rightarrow \Pi$.

As pointed out before, the mechanical representation of viscoelasticity provides a straightforward tool for modelling foundation problems, as demonstrated by Kerr [67]. However, this method is limited in that for every new required material representation one needs to re-formulate the whole problem. On the other hand, although the Stieltjes integrals introduce much more complexity to the formulation, they are a more fundamental approach. Given the versatility of the latter method, it will be adopted in the following sections to model the viscoelastic behavior of the tool-prepreg interface.

4.1.2 Time-Dependent Buckling

Previously, buckling stability of viscoelastic structures have been particularly of interest for the application of steel columns at high temperatures due to fire, and polymer matrix composite materials in hygrothermal environments. When a viscoelastic structure is subjected to a force, the application of forces is responded by the instantaneous modulus of the material. As time makes progress, stress relaxation effects take place which cause the modulus to decline. This, in turn, decreases the critical buckling load of the structure which is a function of the *time-dependent modulus*. As soon as the critical buckling load is decreased to the level of applied load, the structure buckles.

In the context of composite plates exhibiting some degree of anisotropy and viscoelasticity, two approaches are available for solving the buckling problems. Firstly, is the viscoelasticity method which is also known as the *quasi-static* solution. Although variables are time-dependent it should be noted that the solution is different from dynamic buckling, in that inertia effects are neglected (hence the name quasi-static). The method utilizes Laplace or Laplace-Carson transformations to circumvent the integral equations in the governing viscoelastic differential equations by mapping them into regular multiplications.

The second method is the *quasi-elastic* solution. This approximation method ignores the stress variations with time and assumes that internal forces and moments are time-wise constant. By doing so, the time-varying viscoelastic properties can be directly substituted in the elastic solution. This method was first introduced by Schepary in 1965 [68] and it has been proved to be an effective assumption for various cases involving buckling of viscoelastic composite plates (see e.g. [69]).

4.1.3 Model Development

4.1.3.1 Description of the Model

During the prepreg deposition process, prepreg materials are transferred from the spools to the compaction roller, through the AFP head's feeding mechanism. The compaction roller incrementally lays down the prepreg onto the surface of the tool, while forcing the prepreg to follow the prescribed trajectory of the AFP head. Since the tow lay-up is a continuous process, wrinkles are often formed one by one during the steering of tows. As the layup process makes progress, the length of the laid-down tow increases and strain energy is stored in the tow. The strain energy is stored as a result of the tensile force which is applied to keep the tows straight, and the bending moment which is induced as a result of the AFP head following the prescribed curvilinear trajectory. Consequently, compressive stress builds up at the inside edge of the prepreg tow. After reaching a certain threshold, at which the prepreg tackiness cannot support the steered tow anymore, the tow buckles (in the form of wrinkles) and hence, excessive strain energy is dropped. It is worthwhile to mention that at least in sever cases, the wrinkles are, roughly, formed uniformly through the length of the steered tow.

The phenomenological explanation of the wrinkle formation process in conjunction with experimental observations presented above, suggest that each wrinkle could be analyzed individually in isolation from the others. In this case, small parts of the steered prepreg tow that are being analyzed for one individual wrinkle, can be considered as rectangular plates. The presence of continues unidirectional fibers embedded inside the viscoelastic resin causes the prepregs to exhibit an orthotropic viscoelastic behavior. Meaning that the prepreg's response to stress depends on the material direction, as well as the rate of deformation, loading and temperature histories. Among different directions, the on-axis fiber direction is least dependent on these parameters since its behavior is governed by the highly stiff and elastic fibers. On the other hand, the transverse direction and in-plane shear modulus are dominated by the resin's characteristics and hence, they exhibit directional viscoelastic behavior. A major difficulty of considering the prepreg fully viscoelastic is that the complete loading, rate and temperature histories of the materials during the process are too complex to be incorporated into the model (analytical closed-form solutions would not be viable). More importantly, during the steering, the primary mode of deformation of prepreg tows in industrial AFP heads is in-plane bending which is governed by linearly elastic fiber behavior. Therefore, the prepreg tow is considered to be a linearly elastic orthotropic plate. Major part of the inaccuracies introduced as a result of this reductionist assumption are accounted for by characterizing the prepreg materials at appropriate rates and temperatures that are comparable with the real AFP process. This will be further discussed in the section regarding material characterization. Additionally, if any stress relaxation effects take place while the prepreg is laid-down on the tool, by reducing the compressive stresses built-up at the inside edge of the tow, they act in favor of having a better quality and a defect-free layup.

Buckling of the prepreg tow (formation of wrinkles) is opposed by prepreg tack. Tack is they main mechanism resisting against various forms of defects. Therefore, viscoelastic representation of tack is of great importance and cannot be ignored. Prepreg tack is modeled as a foundation on which the prepreg tow is resting. General viscoelastic elements ($k(t)$) are considered for the normal response of the foundation model. Additionally, a unit-thickness shear layer is introduced between the viscoelastic elements and the plate to produce some level of interaction between the foundation elements. Belhaj and Hojjati previously demonstrated in the context of elastic local models that the shear layer (G) is capable of improving the model by representing a more realistic behavior for the tack. Figure 4.2 is the schematic representation of the problem.

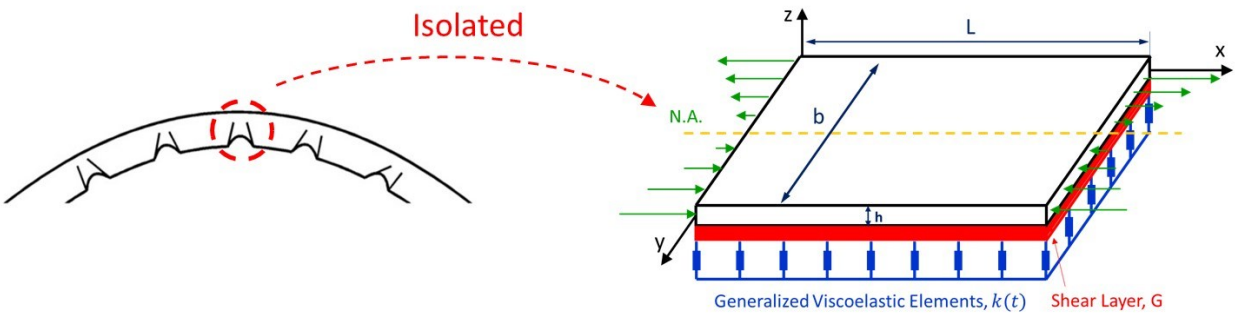

Figure 4.2 Problem definition.

4.1.3.2 Formulation of the Model

Firstly, the response of the foundation should be found. The free body diagram of the plate resting on the generalized viscoelastic Pasternak foundation, with an infinitesimal element of the shear layer with dimensions $dx \times dy \times 1$ are depicted in Figure 4.3. Writing the balance of forces along the z direction will result in the force that is exerted from the foundation (prepreg/tool interface) to the plate (prepreg tow).

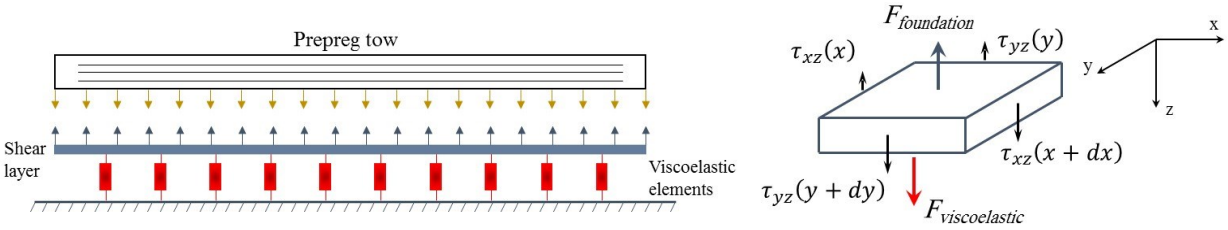

Figure 4.3 Left: free body diagram of a plate resting on viscoelastic Pasternak foundation Right: infinitesimal element from the shear layer; shear force as a function of position.

$$\Sigma F_z = 0: \quad F_{visco} \cdot dx \cdot dy - F_{foundation} \cdot dx \cdot dy + \tau_{xz}(x+dx) \cdot dy \cdot (1) - \tau_{xz}(x) \cdot dy \cdot (1) + \tau_{yz}(y+dy) \cdot dx \cdot (1) - \tau_{yz}(y) \cdot dx \cdot (1) = 0 \tag{4.4}$$

Using the definition of differentiation and the stress-strain relation for the isotropic shear layer, the foundation force is obtained.

$$F_{foundation} = F_{visco} + G\left(w_{,xx} + w_{,yy}\right) \tag{4.5}$$

Comma in the subscripts denotes partial differentiation, G is the shear modulus of the isotropic shear layer and w is the displacement of the plate along the z direction. Now, the viscoelastic force-displacement response of the base is expressed in terms of the Stieltjes integral.

$$F_{visco} = -K * dw \equiv -\int_0^t K(t-\vartheta)\, dw(\vartheta) \tag{4.6}$$

K is the equivalent of the stress relaxation function for the force-displacement relation. The negative sign demonstrates the resistive nature of the foundation response.

As mentioned earlier, each wrinkle can be treated individually since they are formed in isolation from one another and roughly appear regularly. The time-dependent wrinkle formation in the steered prepregs during the automated fiber placement process is modelled as the time-dependent buckling problem of a rectangular plate resting on a viscoelastic foundation which is subjected to an in-plane distributed axial load. The viscoelastic foundation accounts for the time-dependent tack of the prepreg tow which in turn is a function of various process parameters, material properties, and tool and environment conditions. The equations governing the buckling of the plate are developed, now.

Given the large length and width to thickness ratio of a prepreg tape, the model will be predicated on the Kirchhoff hypothesis. In addition, large transverse deformations with moderate rotations and small strains are considered to account for the out-of-plane buckling. Under these assumptions, both elastic and viscoelastic materials remain in the linear region of the stress-strain relationship. Significant components of the Green-Lagrange strain tensor that will remain after applying these assumptions are presented in equation (4.7).

$$\varepsilon_{xx} = u_{,x} + \frac{1}{2}\left(w_{,x}\right)^2 \qquad \varepsilon_{xy} = \frac{1}{2}\left(u_{,y} + v_{,x} + w_{,x}w_{,y}\right)$$

$$\varepsilon_{yy} = v_{,y} + \frac{1}{2}\left(w_{,y}\right)^2 \qquad \varepsilon_{xz} = \frac{1}{2}\left(u_{,z} + w_{,x}\right) \tag{4.7}$$

$$\varepsilon_{zz} = w_{,z} \qquad \varepsilon_{yz} = \frac{1}{2}\left(v_{,z} + w_{,y}\right)$$

Substituting the displacement field for the Kirchhoff plate into equation (4.7), and neglecting the in-plane displacements of the mid-plane results in the strain-displacement relations.

$$\begin{gathered}
\varepsilon_{xx} = \frac{1}{2}\left(w_{0,x}\right)^2 - zw_{0,xx} \equiv \varepsilon_{xx}^0 + z\varepsilon_{xx}^1 \\
\varepsilon_{yy} = \frac{1}{2}\left(w_{0,y}\right)^2 - zw_{0,yy} \equiv \varepsilon_{yy}^0 + z\varepsilon_{yy}^1 \\
\varepsilon_{xy} = \frac{1}{2}w_{0,x}w_{0,y} - zw_{0,xy} \equiv \varepsilon_{xy}^0 + z\varepsilon_{xy}^1 \\
\varepsilon_{zz} = \varepsilon_{xz} = \varepsilon_{yz} = 0
\end{gathered} \tag{4.8}$$

These equations are also known as the *von Kármán* strains. In this equation, a new notation is also introduced. The 0 superscript denotes the *membrane strains* while the 1 superscript denotes the *flexural or bending strains.*

The buckling problem is formulated through the application of the quasi-static principle of virtual displacements. This principle states that:

$$\delta W_I + \delta W_E \equiv \delta W = 0 \tag{4.9}$$

This principle holds *independent* of the constitutive law used to describe the material properties. In this equation δW_I and δW_E are the internal and external virtual works, respectively. The internal virtual displacements are defined by:

$$\delta W_I = \int_\Omega \sigma : \delta\varepsilon \, d\Omega \tag{4.10}$$

where Ω is the volume of the plate. Using equation (4.8), equation (4.10) is expanded.

$$\delta W_I = \int_A \int_{-\xi/2}^{\xi/2} \left[\sigma_{xx}(\delta\varepsilon_{xx}^0 + z\delta\varepsilon_{xx}^1) + \sigma_y\left(\delta\varepsilon_{yy}^0 + z\delta\varepsilon_{yy}^1\right) + 2\sigma_{xy}\left(\delta\varepsilon_{xy}^0 + z\delta\varepsilon_{xy}^1\right)\right] dz\, dA \tag{4.11}$$

At this point, the definition of stress resultants and moments are introduced:

$$N_{ij} = \int_{-\xi/2}^{\xi/2} \sigma_{ij}\, dz \quad M_{ij} = \int_{-\xi/2}^{\xi/2} \sigma_{ij} z\, dz \tag{4.12}$$

Integrating (4.11) over the thickness and using the moment-curvature relation for an orthotropic material, results in:

$$\delta W_I = \int_A \begin{bmatrix} N_{xx}w_{0,x}\delta w_{0,x} + N_{yy}w_{0,y}\delta w_{0,y} + N_{xy}\left(w_{0,x}\delta w_{0,y} + w_{0,y}\delta w_{0,x}\right) \\ +D_{11}w_{0,xx}\delta w_{0,xx} + D_{12}\left(w_{0,xx}\delta w_{0,yy} + w_{0,yy}\delta w_{0,xx}\right) \\ +D_{22}w_{0,yy}\delta w_{0,yy} + 4D_{66}w_{0,xy}\delta w_{0,xy} \end{bmatrix} dA \tag{4.13}$$

where D_{ij} are the components of the flexural stiffness matrix relating moments and curvatures. In this study, the only available external load is the one exerted from the viscoelastic foundation on the bottom of the plate. The virtual work of the actual (external) foundation force, undergoing virtual displacements is presented in equation (4.14).

$$\delta W_E = -\int_A F_{foundation}\delta w_0\, dA = -\int_A \left(-K * dw + Gw_{0,xx} + Gw_{0,yy}\right)\delta w_0\, dA \tag{4.14}$$

In an attempt to balance the differentiations, integration by parts is performed on the terms that are contributed from the shear layer (coefficients of G). After omitting the boundary terms resulted from this procedure, equation (4.14) reads:

$$\delta W_E = \int_A \left(K * dw\, \delta w_0 + Gw_{0,x}\delta w_{0,x} + Gw_{0,y}\delta w_{0,y}\right) dA \tag{4.15}$$

Equations (4.9), (4.13) and (4.15), together, fully define the buckling of an orthotropic plate resting on a generalized viscoelastic Pasternak foundation which is subjected to in-plane loadings. In the next section, the strategy to solve these equations is elaborated upon.

4.1.4 Solution Strategy

The first mode of buckling at the inner edge of the prepreg tow is considered. In order to better simulate the wrinkles, the side edges of the plate are considered to be clamped. The inside edge is free so the buckling occurs at this edge. The outside edge is simply supported to be able to rotate and facilitate buckling. The boundary conditions and loading of the plate are presented in Figure 4.4. The internal force that is induced in the prepreg tow as a result of the steering process and extension can be expressed as a distributed axial load applied at the side edges:

$$N_{xx}(y) = P_0\left(1 - \frac{\alpha y}{b}\right) \tag{4.16}$$

where P_0 is the maximum load applied at the inner edge of the plate, b is the width of the tow and α is the parameter governing the shape of the load distribution (e.g. $\alpha = 2$ produces pure bending condition).

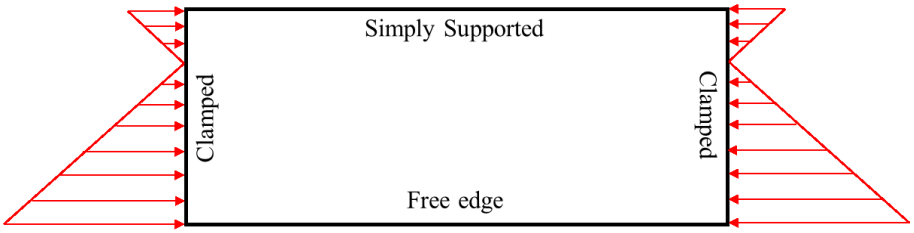

Figure 4.4 Boundary conditions and loading.

The governing equation of the out-of-plane deformation of the plane (as derived in the previous section) can be solved to obtain the buckling load. Rayleigh-Ritz method can be implemented to solve the governing equations. In this method the out of plane deformation is represented in terms of a complete series of linearly independent basis functions of variable amplitude. Fourier Transform has bee widely used as a standard representation which satisfies all required qualities. A problem that arises is that large number of terms is required for obtaining good results. Once, more than a few terms are required in such series, the resulting expression will not be appropriate for deriving closed form solutions. It was previously shown (see e.g. [70]) using appropriate one-

term deformation functions that can effectively capture the overall form of the plate, can be sufficient for representing the deformation. The appropriate deformation can be postulated based on observing the buckling patterns in a rigorous finite element analysis. A one-term displacement series has the distinct advantage over an infinite series in that an approximate *closed-form* solution becomes viable. For the loading and boundary conditions that are considered in the present study, the following shape functions are proposed [60, 70]:

$$u = \sum_{j=1}^{N} c_j(t)\varphi_j(x,y) \qquad \delta u = \sum_{i=1}^{N} \delta c_i(t)\varphi_i(x,y) \tag{4.17}$$

$$\varphi_j(x,y) = \left(1 - \frac{y}{b}\right)^{j+1}\left(1 - \cos\frac{2\pi m}{l}x\right)$$

In equation (4.17), j determines the buckling mode number. For the specific application of the present study, i.e. wrinkle formation, buckling always occurs in the first mode ($j=1$). Now, substituting the proposed shape functions of equation (4.17) into the governing equations (4.9), (4.13) and (4.15):

$$\begin{aligned} 0 = \int_{\mathrm{A}} \big[& -P_0(1-\alpha y/b)\Sigma c_j(t)\varphi_{j,x}\,\Sigma\delta c_i(t)\varphi_{i,x} + D_{11}\,\Sigma c_j(t)\varphi_{j,xx}\,\Sigma\delta c_i(t)\varphi_{i,xx} \\ & + D_{12}\big(\Sigma c_j(t)\varphi_{j,yy}\,\Sigma\delta c_i(t)\varphi_{i,yy} + \Sigma c_j(t)\varphi_{j,xx}\,\Sigma\delta c_i(t)\varphi_{i,xx}\big) \\ & + D_{22}\,\Sigma c_j(t)\varphi_{j,yy}\,\Sigma\delta c_i(t)\varphi_{i,yy} + 4D_{66}\,\Sigma c_j(t)\varphi_{j,xy}\,\Sigma\delta c_i(t)\varphi_{i,xy} \\ & + G\,\Sigma c_j(t)\varphi_{j,x}\,\Sigma\delta c_i(t)\varphi_{i,x} + G\,\Sigma c_j(t)\varphi_{j,y}\,\Sigma\delta c_i(t)\varphi_{i,y} + K \\ & * d\big(\Sigma c_j(t)\varphi_j\big)\,\Sigma\delta c_i(t)\varphi_i\big] dA \end{aligned} \tag{4.18}$$

The last term of equation (4.18), corresponding to the viscoelastic response of the interface which is dictating the time dependency of the approximation coefficients (c). The δc_i which is common among all terms is factorized. It is noted that this equation must hold for all admissible variations of the coefficient (δc_i). Therefore, in order for this to stay true, the coefficients of δc_i must be equal to zero. Then, the Laplace-Carson transformation is performed on the equation (consult the Appendix A: Transformations; for an overview of the transformations) to replace the convolution integral with multiplication in the Laplace-Carson space.

After mapping the time-dependent functions to the Laplace-Carson space, equation (4.18) is re-arranged in the matrix form to simplify the notation. Equation (4.19) is the final equation of the Eigenvalue problem.

$$\left([\tilde{R}(s)] - \widetilde{P_0}[B]\right)\{\widetilde{c_j}(s)\} = \{0\} \tag{4.19}$$

where *s* is the Laplace-Carson variable and tilde represents the transformed function. Components of the matrices $[B]$ and $[R]$ can be found by equations (4.20) and (4.21):

$$B_{ij} = \int_A \varphi_{j,x}\varphi_{i,x}\left(1 - \frac{\alpha y}{b}\right) dA \tag{4.20}$$

$$\widetilde{R_{ij}}(s) = \int_A \begin{bmatrix} D_{11}\varphi_{i,xx}\varphi_{j,xx} + D_{12}\left(\varphi_{j,yy}\varphi_{i,xx} + \varphi_{j,xx}\varphi_{i,yy}\right) + D_{22}\varphi_{j,yy}\varphi_{i,yy} + \\ 4D_{66}\varphi_{j,xy}\varphi_{i,xy} + G\varphi_{j,x}\varphi_{i,x} + G\varphi_{j,y}\varphi_{i,y} + \tilde{K}(s)\,\varphi_i\varphi_j \end{bmatrix} dA \tag{4.21}$$

Finally, the critical time-dependent buckling load can be obtained by solving equation (4.19).

$$P_{cr}(t) = \mathcal{L}^{-1}\left\{\frac{1}{s}\frac{[\widetilde{R(s)}]}{[B]}\right\} \tag{4.22}$$

where $\mathcal{L}^{-1}$ is inverse Laplace transform. The term $1/s$ in this equation maps the Laplace-Carson space to the Laplace space.

Now, the analytical expression for the time-dependent buckling load of a simple case where $N = i = j = 1$ is obtained. All of the terms in equation (4.21) are time-independent (since the prepreg is assumed to be elastic) except for the last one. Therefore, the critical load is comprised of time-independent component (P_{cr}^1) and a time-dependent one (P_{cr}^2). Substituting (4.17) into (4.20) and (4.21), and then evaluating (4.22) results in:

$$P_{cr}^1 = \frac{1}{6-\alpha}\left[24D_{11}\left(\frac{\pi m}{L}\right)^2 + 90D_{22}\left(\frac{L}{\pi m b^2}\right)^2 + 160D_{66}\left(\frac{1}{b^2}\right) - 40D_{12}\left(\frac{1}{b^2}\right) + 6G + 30G\left(\frac{L}{\pi m b}\right)^2\right] \tag{4.23}$$

$$P_{cr}^2 = \mathcal{L}^{-1}\left\{\frac{1}{s}\frac{\int_A \tilde{K}(s)\,\varphi_1\varphi_1\,dA}{\int_A \varphi_{1,x}\varphi_{1,x}(1-\alpha y/b)\,dA}\right\} = \frac{\int_A \varphi_1\varphi_1\,dA}{\int_A \varphi_{1,x}\varphi_{1,x}(1-\alpha y/b)\,dA}\mathcal{L}^{-1}\left\{\frac{\tilde{K}(s)}{s}\right\} \tag{4.24}$$

Considering $\mathcal{L}^{-1}\{\widetilde{K}(s)/s\} = \mathcal{L}^{-1}\{\overline{K}(s)\} = K(t)$, and evaluating the integrals will lead to the final time-dependent critical buckling load.

$$P_{cr}(t) = \frac{1}{6-\alpha}\left[\begin{array}{c} 24D_{11}\left(\frac{\pi m}{L}\right)^2 + 90D_{22}\left(\frac{L}{\pi m b^2}\right)^2 + 160D_{66}\left(\frac{1}{b}\right)^2 - 40D_{12}\left(\frac{1}{b}\right)^2 \\ +G\left(6 + 30\left(\frac{L}{\pi m b}\right)^2\right) + \frac{K(t)}{2}\left(\frac{3L}{\pi m}\right)^2 \end{array}\right] \tag{4.25}$$

It is noteworthy to mention that in the simplest explicit form where the solution is evaluated having only one term in the series (4.17), the solution is equivalent to the case of quasi-elastic solution where the elastic modulus shall be replaced by the time-dependent stress relaxation function. Moreover, the value of m shall be considered to be one, since the first mode of buckling occurs.

4.1.5 Relating to the Steering Geometry

Equation (4.25) gives the time-dependent buckling load of an orthotropic plate resting on a generalized viscoelastic Pasternak foundation which is subjected to non-uniform loading. However, in a steered prepreg tow the distributed load is constant and depends merely on the mismatch of tow length resulted from the prescribed trajectory and prepreg mechanical properties. Assuming the path radius R over the angle θ (Figure 4.5), results in the path length $R\theta$ for the neutral axis of the tow. The load distribution coefficient, α, controls the position of the neutral axis. Using α, the length of the inner edge of the tow is found to be $(R - b/\alpha)\theta$ and hence, the strain arose from this mismatch is $b/\alpha R$. Consequently, the maximum load induced at the inner edge of the tow is found:

$$P_{induced} = \frac{E_1 \xi b}{\alpha R} \tag{4.26}$$

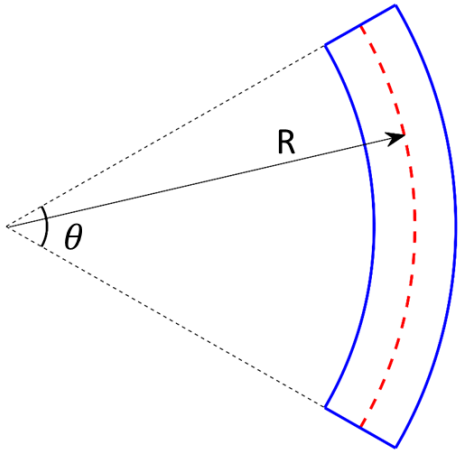

Figure 4.5 Steered tow geometry;
Red dashed line: reference path (or neutral axis of prepreg tow).

Conceptually, if the instantaneous critical buckling load, P_{cr}^{inst}, is less than the maximum induced load (equation (4.26)) the local wrinkles form as soon as the prepreg tow is laid down on the tool. On the other hand, if the relaxed buckling load, P_{cr}^{∞}, is more than the maximum induced load, the layup will be defect free. A special case of interest in the present study is where the prepreg tack is strong enough to resist the out-of-plane deflections temporarily. Hence, the wrinkles form and grow as a function of time (see section 3.2.2) once the viscoelastic relaxation effects take place in the interface (Figure 4.6). In this case, the wrinkle length can be found by solving equations (4.25) and (4.26), simultaneously, at any given time.

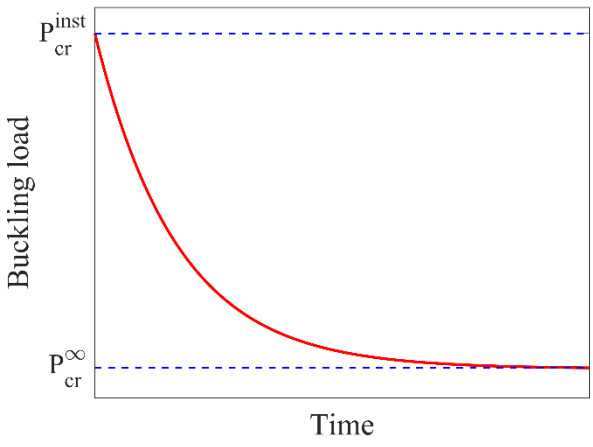

Figure 4.6 Critical buckling load.

4.1.6 Simplification to Elastic Models

4.1.6.1 Elastic Local Modeling of Wrinkles

By using elastic spring elements, instead of the general viscoelastic ones equation (4.6) should be replaced with $F_{spring} = -kw$. Where k is the stiffness of the spring elements and w is the lateral displacement of the plate. Consequently, the work of external loads performed on the plate will be independent of time. The total potential energy of the plate resting on elastic Pasternak foundation reads:

$$\delta\Pi = \iint_A \left[N_{xx}w_{,x}\delta w_{,x} + D_{11}w_{,xx}\delta w_{,xx} + D_{12}\left(w_{,yy}\delta w_{,xx} + w_{,xx}\delta w_{yy}\right) + D_{22}w_{,yy}\delta w_{,yy} + 4D_{66}w_{,xy}\delta w_{,xy} + kw\delta w + G(w_{,x}\delta w_{,x} + w_{,y}\delta w_{,y})\right]dA \tag{4.27}$$

Finally, in the quasi-static critical buckling load of the plate, equation (4.25), the time dependent term should be replaced with constant stiffness. When using elastic models, it is possible to further develop the solution to obtain the critical steering radius, or in the radii smaller than the critical one, the wavelength of occurrence of wrinkles.

$$P_{cr} = \frac{1}{6-\alpha}\left[24D_{11}\left(\frac{\pi m}{L}\right)^2 + 90D_{22}\left(\frac{L}{\pi m b^2}\right)^2 + 160D_{66}\left(\frac{1}{b}\right)^2 - 40D_{12}\left(\frac{1}{b}\right)^2 + G\left(6 + 30\left(\frac{L}{\pi m b}\right)^2\right) + \frac{k}{2}\left(\frac{3L}{\pi m}\right)^2\right] \tag{4.28}$$

Similar to the previous section, m can only take the value one since the first mode of buckling is the only possible scenario. A critical buckling load exists for any plate with a given length. However, with the incremental accumulation of steered tow, the excess amount of energy would be *naturally released* at the wrinkle wavelength (corresponding to the plate length) that minimizes energy levels of the structure. In order to find that wavelength the critical buckling load is differentiated with respect to wavelength, L, and its local extremum of the function is found. The load correspond to that wavelength, i.e. the minimum load, is of interest here and presented in (4.29):

$$P_{min} = \frac{2}{(6-\alpha)b^2\chi_1}\begin{bmatrix}360\sqrt{3}D_{22}D_{11} + 18\sqrt{3}kb^4D_{11} + 120\sqrt{3}Gb^2D_{11} \\ +2\chi_1(40D_{66} - 10D_{12}) + 3Gb^2\chi_1\end{bmatrix} \tag{4.29}$$

where:

$$\chi_1 = \sqrt{D_{11}(180D_{22} + 9kb^4 + 60Gb^2)} \tag{4.30}$$

Solving the induced load equation (4.26), along with the minimum load equation (4.29), the critical steering radius is obtained ($R_{cr} = E_1\xi b/\alpha P_{min}$).

$$R_{cr} = \frac{(6-\alpha)E_1\xi b^3\chi_1}{2\alpha\begin{bmatrix}360\sqrt{3}D_{22}D_{11} + 18\sqrt{3}kb^4D_{11} + 120\sqrt{3}Gb^2D_{11} \\ +2\chi_1(40D_{66} - 10D_{12}) + 3Gb^2\chi_1\end{bmatrix}} \tag{4.31}$$

In the instances where the steering radius is smaller than the critical value, the local model predicts the occurrence of wrinkles. Moreover, the number of wrinkles appeared is predicted with the wrinkle wavelength. The wavelength is found by solving equations (4.26) and (4.28) for L. These two equations can be arranged in form of a quadratic equation:

$$\begin{aligned}&L^4\left[90D_{22}\left(\frac{1}{\pi b^2}\right)^2 + \frac{9}{2}\frac{1}{\pi^2}\,k + 30G\left(\frac{1}{\pi b}\right)^2\right] \\ &+L^2\left[160D_{66}\left(\frac{1}{b^2}\right) - 40D_{12}\left(\frac{1}{b^2}\right) - (6-\alpha)\left(\frac{E_1hb}{\alpha R}\right) + 6G\right] + 24\pi^2D_{11} = 0\end{aligned} \tag{4.32}$$

Equations (4.28) to (4.32) represent the elastic local mode that was obtained by Belhaj [61]. Furthermore, by assuming that the foundation is solely comprised of spring elements (Wrinkle foundation), hence, substituting $G = 0$ in the mentioned equations, formulation of Matveev et al. [60] for the local wrinkle modeling is deduced.

4.1.6.2 Elastic Local Modeling of Blisters

In this section, the possibility of extending the local models for predicting blisters are explored. Based on the shape of the blisters observed during the experiments, two different boundary conditions for a plate which represents blisters will be presented, namely a clamped plate (CCCC) and a simply supported plate (SSSS). The shapes of the buckled representative plates under these two boundary conditions are presented in Figure 4.7.

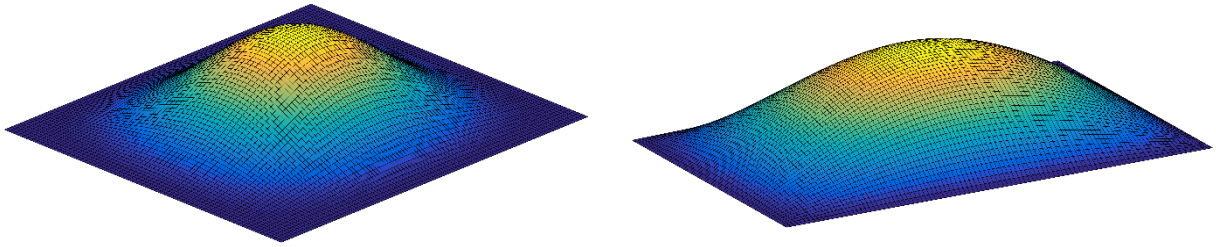

a. CCCC plate b. SSSS plate

Figure 4.7 Boundary conditions for local blister modeling.

For a clamped plate the following shape functions can be assumed in the Ritz solution to obtain the critical buckling load of the representative plate.

$$w(x,y)=\sum_{m=1}^{M}\sum_{n=1}^{N}w_{mn}\left(1-\cos\left(\frac{2\pi m}{L}x\right)\right)\left(1-\cos\left(\frac{2\pi n}{b}y\right)\right)\equiv\sum_{m=1}^{M}\sum_{n=1}^{N}c_{mn}X_m(x)Y_n(y) \tag{4.33}$$

$$\delta w(x,y)=\delta c_{pq}\left(1-\cos\left(\frac{2\pi p}{L}x\right)\right)\left(1-\cos\left(\frac{2\pi q}{b}y\right)\right)\equiv\delta c_{pq}X_p(x)Y_q(y) \tag{4.34}$$

Using the proposed functions as the lateral deformation of the plate, total potential energy of the clamped orthotropic plate resting on the Pasternak foundation, equation (4.27), is expanded.

$$\begin{aligned}\delta\Pi=\sum_{m=1}^{M}\sum_{n=1}^{N}c_{mn}\iint_A\Bigg[&-P_0\left(1-\alpha\frac{y}{b}\right)\frac{dX_m}{dx}Y_n\frac{dX_p}{dx}Y_q+D_{11}\frac{d^2X_m}{dx^2}Y_n\frac{d^2X_p}{dx^2}Y_q\\&+D_{12}\left(X_m\frac{d^2Y_n}{dy^2}\frac{d^2X_p}{dx^2}Y_q+\frac{d^2X_m}{dX^2}Y_nX_p\frac{d^2Y_q}{dy^2}\right)+D_{22}X_m\frac{d^2Y_n}{dy^2}X_p\frac{d^2Y_q}{dy^2}\\&+4D_{66}\frac{dX_m}{dx}\frac{dY_n}{dy}\frac{dX_p}{dx}\frac{dY_q}{dy}+kX_mY_nX_pY_q+G\left(\frac{dX_m}{dx}Y_n\frac{dX_p}{dx}Y_q+X_m\frac{dY_n}{dy}X_p\frac{dY_q}{dy}\right)\Bigg]dA\end{aligned} \tag{4.35}$$

In the present problem, it can be assumed that the first mode of buckling occurs. Using $m=n=p=q=1$, the critical buckling load is found.

$$P_{cr}=\frac{1}{2-\alpha}\left[8D_{11}\left(\frac{\pi}{L}\right)^2+\frac{16}{3}D_{12}\left(\frac{\pi}{b}\right)^2+8D_{22}\left(\frac{\pi L}{b^2}\right)^2+\frac{32}{3}D_{66}\left(\frac{\pi}{b}\right)^2+\frac{3}{2}k\left(\frac{l}{\pi}\right)^2+2G\left(1+\left(\frac{L}{b}\right)^2\right)\right] \tag{4.36}$$

Similar, to the wrinkle formation, one needs to find the minimum critical buckling load with respect to the blister's wavelength (L). This is obtained by finding the extremum of equation (4.36) as a function of length. The minimum critical buckling load for the minimum wavelength and, subsequently, the critical steering radius for having blister-free tows are found (see the above section for a more detailed reasoning).

$$P_{min} = \frac{1}{2-\alpha}\left[4\frac{D_{11}}{\chi_2} + \frac{16}{3}\left(\frac{\pi}{b}\right)^2 D_{12} + \frac{32}{3}\left(\frac{\pi}{b}\right)^2 \mathrm{D}_{66} + 2G\right] \tag{4.37}$$

$$R_{cr} = \frac{(2-\alpha)E_1\xi b}{\alpha\left[4\frac{D_{11}}{\chi_2} + \frac{16}{3}\left(\frac{\pi}{b}\right)^2 D_{12} + \frac{32}{3}\left(\frac{\pi}{b}\right)^2 \mathrm{D}_{66} + 2G\right]} \tag{4.38}$$

where:

$$\chi_2 = \sqrt{\frac{D_{11}\mathrm{b}^4}{16\pi^4 D_{22} + 3b^4 k + 4\pi^2 b^2 G}} \tag{4.39}$$

As the second configuration, a simply supported plate is considered. The solution of Ritz method can be assumed in the following form which satisfies all the essential boundary conditions.

$$\begin{gathered} w(x,y) = \sum_{m=1}^{M}\sum_{n=1}^{N} c_{mn}\sin\left(\frac{m\pi}{L}x\right)\sin\left(\frac{n\pi}{b}y\right) \\ \delta w = c_{pq}\sin\left(\frac{p\pi}{L}x\right)\sin\left(\frac{q\pi}{b}y\right) \end{gathered} \tag{4.40}$$

Evaluating (4.35) with the new sine functions as X_m, Y_n, X_p and Y_q the critical buckling load of the simply supported plate is obtained.

$$P_{cr} = \frac{1}{2-\alpha}\left[2D_{11}\left(\frac{\pi}{L}\right)^2 + 4D_{12}\left(\frac{\pi}{b}\right)^2 + 2D_{22}\left(\frac{\pi L}{b^2}\right)^2 + 8D_{66}\left(\frac{\pi}{b}\right)^2 + 2k\left(\frac{L}{\pi}\right)^2 + 2G\left(1+\left(\frac{L}{b}\right)^2\right)\right] \tag{4.41}$$

Similarly, the critical buckling load is minimized for extremum length of buckling and subsequently, the critical steering radius for attaining blister-free tows based on the simply supported plate is found.

$$P_{min} = \frac{1}{2-\alpha}\left[4\frac{D_{11}}{\chi_3} - 4\left(\frac{\pi}{b}\right)^2 D_{12} + 8\left(\frac{\pi}{b}\right)^2 D_{66} + 2G\right] \tag{4.42}$$

$$R_{cr} = \frac{(2-\alpha)E_1\xi b}{\alpha\left[4\frac{D_{11}}{\chi_3} - 4\left(\frac{\pi}{b}\right)^2 D_{12} + 8\left(\frac{\pi}{b}\right)^2 D_{66} + 2G\right]} \tag{4.43}$$

where:

$$\chi_3 = \sqrt{\frac{b^4 D_{11}}{\pi^4 D_{22} + b^4 k + b^2 \pi^2 G}} \tag{4.44}$$

4.2 GLOBAL MODELING APPROACH [64]

Local defect modeling approaches assume that defects occur with a constant frequency which does not necessarily comply with the experimental observations all the time (see for instance, Figure 3.8). Moreover, local modeling approach is restrained to modeling the wrinkles that are merely driven by plate buckling mechanism. Most defects are produced as a result of a series of complex interactions between the tool, prepreg, compaction roller and AFP process parameters. Obviously, the local modeling approach cannot be generalized to incorporate all these different parameters into the models.

Alternatively, in the present work, a novel modeling framework using *finite element analysis* in the commercial package Abaqus is presented. This framework, called global modeling approach, simulates the prepreg deposition process of AFP and enables the user to gain a more comprehensive understanding of the stress distribution and defect formation processes. Furthermore, it can be generalized to more advanced models for studying and simulating various effects on the process and ultimately, on the layup quality.

4.2.1 General Model Information

The Abaqus model constitutes five parts: A rigid tool, a rigid bar which simulates the steering path, a deformable compaction roller, a rigid guide for the movement of prepreg tow, and finally the prepreg tow. The width of the compaction roller is 35 mm, outer diameter is 36.83 mm and inner diameter is 16 mm. The assembled model with the used boundary conditions is presented in Figure 4.8. The reference point of the rigid bar is set to rotate at a constant speed (corresponding to the linear speed of the head), it is allowed to move in the y-direction where the compaction force is applied. All other degrees of freedom of the rigid bar's reference point are constrained. A constant compaction pressure of 0.8 MPa is applied on top of the bar over 17.5 mm, simulating the actual value of the compaction force applied in the process.

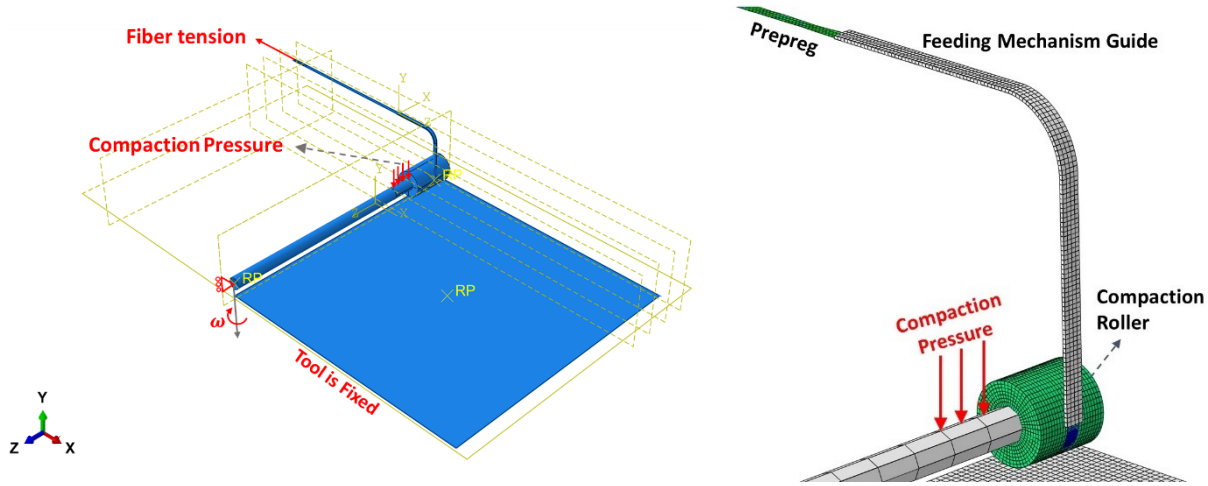

Figure 4.8 The assembled model.

Kinematic coupling constraints are created between the free end of the prepreg tow and the guide, to facilitate the movement of prepreg tow inside the guide. Additionally, a 10 N/mm force is applied to the free end of the tow to simulate the fiber tension which helps keeping the tows straight during the simulation. Prepreg tow is meshed using linear S4R shell elements. Three-dimensional C3D8R brick elements are used to generate the roller's mesh and discrete rigid shell elements were used for the rigid bodies.

For the majority of the different combinations of process conditions that were performed, defects were appeared as soon as the prepreg was laid-up, i.e. there was almost no growth of defects with time. When time-dependent deformation is not considerable or of interest, elastic material behavior can be attributed to the prepreg and interface (tack) elements. In this situation, by characterizing the material at relevant conditions, the application of elastic behavior is valid and can simulate the actual process. The reason is that by providing model inputs that were measured at appropriate rates and temperatures, the right values for mechanical properties are being used in the models. An alternative way could be using the time-temperature superposition along with viscoelastic material properties for both prepreg and interface, in order to eliminate the need for performing characterization tests for each set of process parameters (which is required when the model is sensitive to a specific parameter and that parameter is highly rate- and temperature- dependent).

In the explicit dynamic model developed in this section, the rigid bar (with the length corresponding to the steering radius in the AFP process), rotates with the angular velocity which simulates the linear speed of the AFP head. As the bar rotates, prepreg tow follows the rigid feeding mechanism and comes into contact with tool surface where the cohesive forces between the prepreg surface and tool surface (simulating prepreg tack) become activated. A sample image from the middle of the simulation is presented in Figure 4.9. Subsequently, the forces that are induced in the prepreg tow as a result of steering want the prepreg tow to buckle, which is resisted by the cohesive interactions. If these internal forces are high enough, they can cause the interface to progressively fail locally, or throughout the tow. This progressive failure will finally result in the process induced defects. Details of the simulation of prepreg tack are presented in the next section.

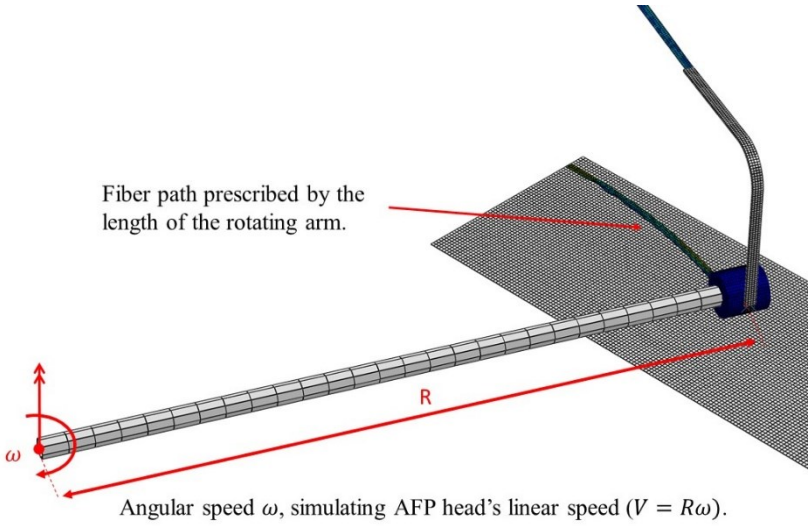

Figure 4.9 Sample image from the middle of the simulation.

4.2.2 Simulating Prepreg Tack

Several different approaches are available for modeling fracture and delamination including continuum mechanics, fracture mechanics, XFEM and damage mechanics. For modeling the prepreg tack, an especial approach in the damage mechanics, called Cohesive Zone Modelling (CZM) is utilized [71]. Tack is merely intended to be modeled as an interfacial property since cohesive failure of prepregs is not feasible when using practical process parameters. Therefore, the delamination surface is known in the AFP process: at the prepreg-tool interface. Finally, since the location of the out-of-plane wrinkles (and more generally, layup defects) are not known, the approaches requiring specification of an initial crack cannot be employed. Considering that CZM complies with all of the modeling requirements of prepreg tack, it has been chosen for the present study. CZM is well established in commercial finite element codes and more importantly, effective methods are available for characterizing the cohesive zone properties.

Fracture mechanics begins with the assumption of energy balance stating that the change in potential energy dW, i.e. the difference between external work dW_E and the internal strain energy dW_I, is equal to the fracture energy $d\Gamma$ over an incremental crack growth dA (equation (4.45)) for a quasi-static, *stable* crack propagation.

$$\frac{dW_E}{dA} - \frac{dW_I}{dA} = \frac{dW}{dA} = \frac{d\Gamma}{dA} \tag{4.45}$$

The irreversible nature of fracture processes result in the rate of fracture energy, $\dot{\Gamma}$, to be always positive ($dW_E > dW_I$). Furthermore, the strain energy release rate may also defined:

$$\text{Energy release rate} = \frac{dW_E}{dA} - \frac{dW_I}{dA} \tag{4.46}$$

Moreover, a *process zone* is defined in the vicinity of the crack tip with elliptic shape and dimensions much smaller than other length scales of the problem. This process zone is capable of incorporating the separation process including inelastic processes involved.

The need to consider a process zone stems from a fundamental difference between the theory of cracking (i.e. fracture mechanics) and the linear theory of elasticity. The first major difference is that when loads applied on a body containing a crack, even if they are very small, the boundary of the crack deforms considerably which in turn causes significant change in the boundary of the whole problem. This is in direct contrast to one of basic assumptions of the theory of elasticity which states that the change in the boundaries of the body under the applied load is small. Consequently, nonlinear deformations should be taken into account in a region close to the crack which is itself unknown and should be found as a part of the solution.

Additionally, when the formal solutions for the elasticity equations are found, the results are in the famous form of $\sigma = SIF/\sqrt{s}$. Where, SIF is the stress intensity factor which is merely a function of the geometry of the problem, and the type of loading applied; and s is the distance from the circumference of the crack. This again leads to a theoretical and an empirical paradox. In the theory of elasticity, free surfaces (including unloaded cracks) are free of stress. Here, however, the stress at the crack surface is found to be infinity. Moreover, since the stress at the crack edge is, in theory, infinitely large, we can not have *any* crack in equilibrium. Meaning that even a small crack under a small loading condition will grow until the part is broken into two pieces; this is obviously not the case in reality as we know defective cracked parts may successfully continue service in various circumstances.

These two paradoxical implications demonstrate the inability and insufficiency of the theory of elasticity to fully describe crack problems. In order to construct an adequate theory of cracking it is crucial to consider the molecular cohesive forces acting in the vicinity of the crack contour where the distance between the opposite faces of the crack is small and they attract one another.

In 1960, for the first time, Dugdale assumed an *ideal* elastic-plastic material model to analyze and trace the spread of plasticity in a plate with an internal slit, both theoretically and experimentally. The idealized material behavior has resulted in considering a constant stress (σ_{yield} of the material) as the traction between the surfaces within the process zone.

In 1962, Barenblatt considered a more realistic traction-separation law within the process zone mimicking the aforementioned molecular cohesive tractions between close surfaces. In this model, the cohesive stresses increase with the applied load up to a critical material value and decrease with the moving crack faces up to zero for the separated surfaces. Following these two classic works, various different traction-separation laws have been considered: The Dugdale (i.e. constant stress), bilinear, trapezoidal and exponential laws (Figure 4.10) are among the mostly used traction separation laws that are employed to describe the cohesive forces inside the cohesive or process zone.

Apart from the Dugdale law, other laws can be roughly divided to two sections: tractions lower than the maximum traction T_{max} where the process is reversible and the same values of traction will be experienced upon cycling. The second part is when the traction has reached and passed T_{max} (or any other measure representing damage initiation) in which an irreversible degrading process occurs. In each of these laws, the values of maximum traction T_{max}, the associated critical separation δ_c^i, maximum separation δ_{max} and critical energy release rate (or fracture energy) Γ_c are required to fully characterize the traction separation law, although it should be noted that depending on the geometry of the law, some of these quantities are inter-dependent and are not independent variables. It is worthwhile to mention that custom *viscoelastic* representations (e.g. Figure 4.1) can also be utilized to describe the time-dependent viscoelasticity for the reversible part of the traction separation laws.

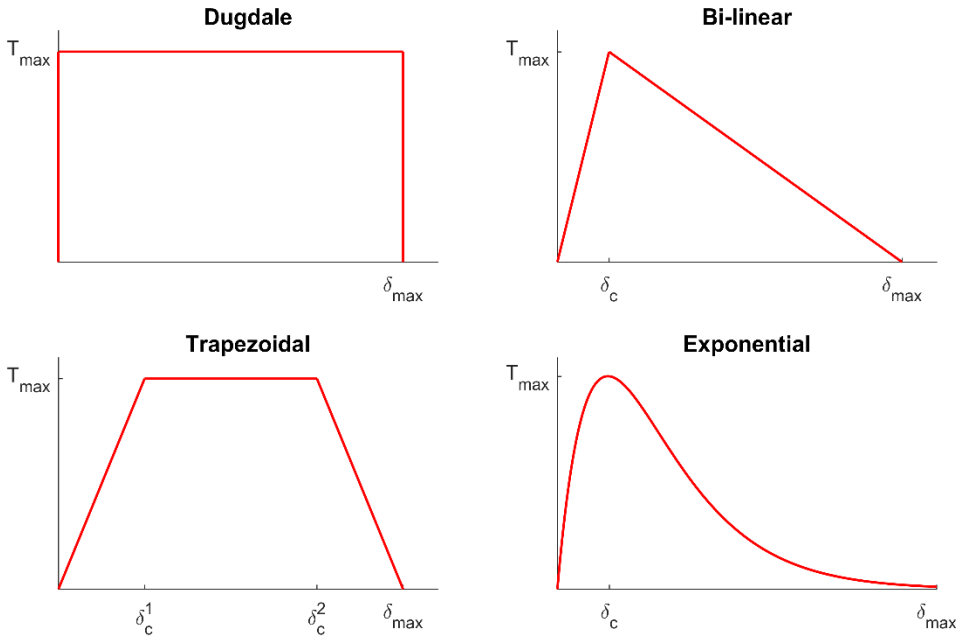

Figure 4.10 Some widely used traction separation laws.

During the fracture process, traction is usually experienced in all three different dimensions (Figure 4.11). Specifically, the normal traction or mode I delamination, the in-plane shear or mode II delamination and the out-of-plane shear or mode III delamination, are the different planes of fracture. In cohesive zone modeling, traction-separation laws can be implemented to describe the behavior of the material/interface in each of the directions.

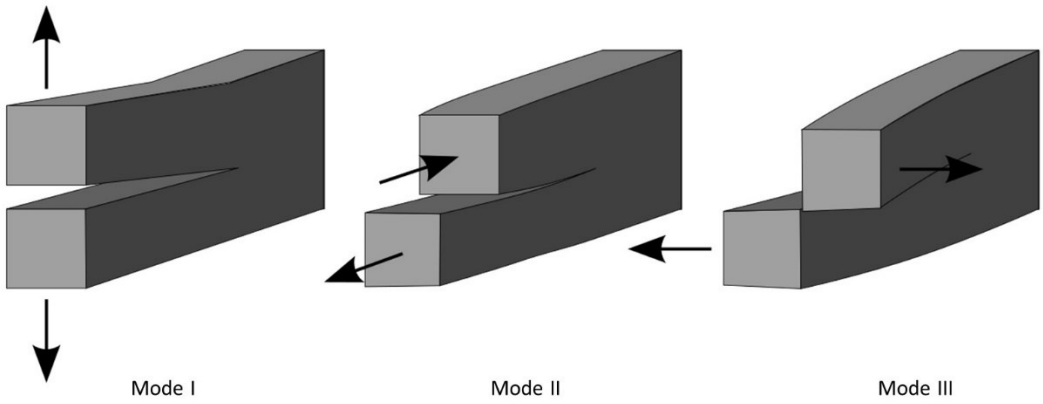

Figure 4.11 Fracture modes [72].

For the current application of simulating prepreg tack, cohesive zone modeling can be introduced into the Abaqus models through surface-based cohesive zone modeling technique. In this technique, the cohesive zone laws are incorporated as contact properties. The cohesive contact is defined such that as soon as a node on the prepreg surface comes into contact with the tool surface the cohesive interactions become activated. Subsequently, when the forces induced in the prepreg tow (as a result of the steered path) are driving the prepreg tow towards slippage or delamination, cohesive forces will be applied to the tow surface. These cohesive forces are a function of the separation between the tow surface and the tool surface at any node as per description of the traction separation law.

A review of the literature (see section 2.2.3) revealed that the most straightforward and ubiquitous method for characterizing *tack* in pressure sensitive adhesives and prepregs is the probe tack test method. Performing the probe test method at controlled prepreg temperatures, dwell times, probe compression and retraction speeds can simulate prepreg tack during the deposition process. Additionally, by enclosing the probe test in an environmental chamber the effects of relative humidity and environment temperature can be understood.

A typical force versus separation diagram obtained through this method was depicted in Figure 2.9. The curve in Figure 2.9 suggests that prepreg tack could be approximated with two linear sections. Consequently, the bilinear traction-separation law is chosen to describe the interactions within the cohesive zone. Figure 4.12 presents a more detailed description of this law. The first section (reversibly elastic section) is defined through the slope of the line identifying the stiffness of the interface (tack). The elastic constitutive matrix representing the stiffness in a mixed mode fracture is presented in (4.47).

$$\boldsymbol{T} = \begin{Bmatrix} T_1 \\ T_2 \\ T_3 \end{Bmatrix} = \begin{bmatrix} K_{11} & K_{12} & K_{13} \\ K_{12} & K_{22} & K_{23} \\ K_{13} & K_{23} & K_{33} \end{bmatrix} \begin{Bmatrix} \delta_n \\ \delta_s \\ \delta_t \end{Bmatrix} = \boldsymbol{K\delta} \tag{4.47}$$

In (4.47) $\boldsymbol{T}$ and $\boldsymbol{\delta}$ are the vectors of tractions and separations, respectively. While 1, 2 and 3 represent the mode I, II and III of delaminations. $\boldsymbol{K}$ is the matrix of stiffness. In simulating prepreg tack, it is assumed that the behavior along each orthogonal direction is independent of the other directions, hence, an *uncoupled behavior* is used and all off-diagonal terms in the $\boldsymbol{K}$ matrix are set to zero.

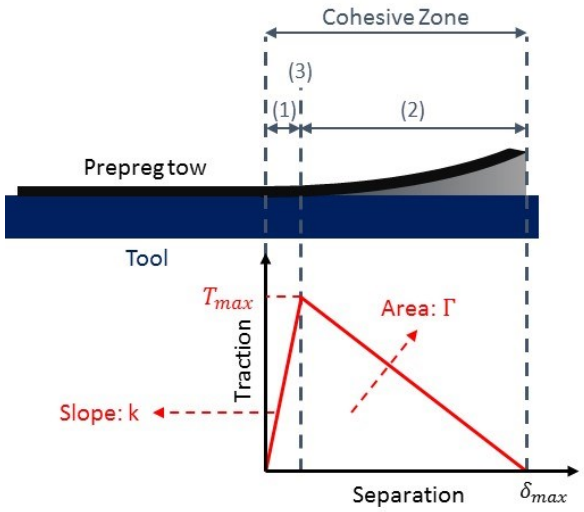

Figure 4.12 Detailed bilinear traction separation law.
(1) Damage initiation (elastic region), (2) Damage propagation (softening region)
(3) Damage initiation criterion (onset of failure).

The second part of the traction separation law, corresponding to the damage evolution, requires a damage initiation criterion and a second measure, for controlling the damage. Maximum nominal stress is chosen to establish the damage initiation and total fracture energy with linear softening is used to define the damage evolution. Total fracture energy method is believed to provide more accurate results as opposed to defining the maximum separation. Based on the total fracture energy, using the stiffness of the elastic portion and the maximum stress the software calculates the maximum separation of the cohesive surface [73]. Failure of the elements is characterized by progressive degradation of the material stiffness, which is driven by a damage process. Consequently, a scalar damage parameter, D, is defined which is representing the overall damage at the contact point. It initially has the value of 0, and monotonically increases up to 1 for the fully damaged and separated interface. Using D, tractions in a damaged interface are provided.

$$T_i = (1 - D)\overline{T_i} \tag{4.48}$$

where, $i = 1$, 2 and 3, corresponding to modes I, II and III of delamination. The overhead bar sign designates the contact stress component predicted by the elastic traction separation behavior for

the current separation without damage; and T_i is the traction for a damaged contact. In a traction separation law with the linear softening the damage parameter is obtained from the separation values.

$$D = \frac{\delta_m^f(\delta_m^{max} - \delta_m^0)}{\delta_m^{max}\left(\delta_m^f - \delta_m^0\right)} \tag{4.49}$$

In (4.49), δ_m is representing effective separation given by (4.50). Superscripts f, 0 and max represent, respectively, effective separation at complete failure, effective separation at damage initiation and the maximum value of the effective separation attained during the loading history. Utilizing the concept of effective separation, Abaqus takes into account the contribution of each failure mode for calculating the damage parameter.

$$\delta_m = \sqrt{\delta_1^2 + \delta_2^2 + \delta_3^2} \tag{4.50}$$

From a more practical stand point, the fact that the maximum separation is, obviously, larger than the separation at which the damage initiates, a simple relation should hold between the fracture energy (i.e. work of adhesion/tack), Γ, the maximum traction, T_{max}, and stiffness (or the slope of the damage initiation part), k:

$$k > T_{max}/2\Gamma \tag{4.51}$$

4.2.3 Solution Method

The Abaqus / Explicit solver is required to solve the explicit dynamic problem at hand. This solver completely takes geometric nonlinearities and the resulting large deformations occurring in the prepreg tows into account. Additionally, it was pointed out before that simulating the damage evolution (i.e. degradation of prepreg tack) is a highly nonlinear process. The explicit solver can handle these nonlinearities very well. It should be noted that on the contrary to the standard solver, the value of stiffness, k, does matter in the explicit solver. It is known that in order to avoid convergence problems, standard Abaqus solver treats the stiffness of the CZ in a manner similar to the penalty method, therefore the stiffness value should be large and it does not affect the final

results significantly. Several models with different prepreg mesh sizes of 2, 1 and 0.5 mm were studied to find the appropriate trade-off between the computation time and resolution of the models. The 2 mm elements proved to provide adequate accuracy. Consequently, the 2 mm elements were primarily used for producing the results of this study.

4.3 MODELS PARAMETERS

4.3.1 Summary of the Required Properties

Both models attribute elastic orthotropic material properties to the uncured prepreg. Therefore, four material constants (E_1, E_2, G_{12} and ν_{12}) are required to solve the models. These data are not readily available in the materials data sheet. Moreover, theoretical models such as the mixture rule cannot be employed to obtain the uncured prepreg property, when that property is fiber-dominated in the post-cure lamina. This is due to the fact that fiber-dominated properties significantly rely on the cured resin to provide load transfer among fibers, which is not considerable in uncured prepregs. Consequently, experiments were conducted [61] to obtain the required parameters.

Since the primary mode of deformation in regular AFP heads is bending of prepreg tow, the longitudinal elastic modulus of prepreg (E_{11}) is of great importance. Moreover, the in-plane shear modulus (G_{12}) could be influential as well and therefore was characterized experimentally. The transverse shear modulus (E_{22}) and Poisson's ratio (ν_{12}) are less consequential and not easily measurable, hence their respective values was obtained from the literature [59], based on Puck's mixture rule.

In addition to the prepreg mechanical properties, prepreg-tool interactions are imperative for the global modeling approach. As discussed in details in section 4.2.2, a bilinear traction separation law is used to represent those interaction. Stiffness of the initial section (k), maximum stress at the onset of failure of the interface (T_{max}) and the total energy required to detach the surfaces, i.e. fracture energy (Γ) are required to solve the simulation. These values are determined based on both in-house experiments [61] and available data in the literature [35].

In the local modeling approach, the properties of the "shear layer" are also needed. Following the work of Belhaj and Hojjati [61] the interaction level between the foundation elements, i.e. the

stiffness of the shear layer, is considered to be equal to the in-plane shear modulus of the prepreg material. Therefore, no further experimentation is required for its characterization.

4.3.2 Experiments

4.3.2.1 Longitudinal Elastic Modulus

The longitudinal elastic modulus of the prepreg was obtained through a tensile test. The prepreg tow was cut in 80 mm-long samples and was let to rest at the room temperature for 30 minutes before the experiments began. The applied tensile load was measured and recorded as a function of displacement which was used to calculate the stress-strain curve. The elastic modulus was determined as the slope of this stress-strain curve.

4.3.2.2 In-plane Shear Modulus

The bias extension test can be used to obtain the in-plane shear modulus of the cross-ply unidirectional composites of [74, 75]. In this test, both ends of the samples are clamped and the composite is subjected to a tensile load with an initial ±45° bias angle with respect to the loading direction. The samples used for this test were 120 mm × 40 mm and had 80 mm un-gripped length. Each sample was made out of two ±45° layers that were pre-consolidated at 70 °C with 0.1 MPa (vacuum pressure) for 30 minutes. A total of three tests were performed using tensile testing machines and non-contracted infrared lamps, to ensure the accuracy and repeatability. The processing temperature at which the tests were performed was 40 °C and the cross-head speed was 100 mm/min.

As depicted in Figure 4.13, each test specimen can be divided into three general regions. In order to obtain a uniform deformation in zone A, the specimens' length should not be less than twice their width. Force and displacement were recorded and data were analyzed to build the normalized shear stress against shear angle diagrams [61]. The slope of the curve prior to the wrinkle formation determines the in-plane shear modulus.

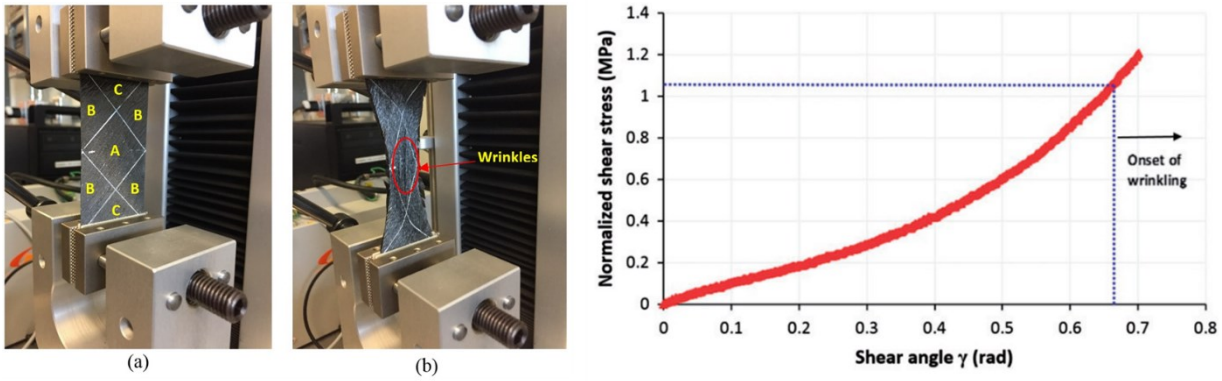

Figure 4.13 The bias extension setup and the sample shear stress – shear angle diagram.

4.3.2.3 Parameters of the Bilinear Traction-Separation Law

As previously discussed in 2.2.3, a commonly used method for quantifying prepreg tack is the probe tack test. Figure 4.14 shows the in-house experimental setup. In this method, a probe comes into contact with the prepreg at a controlled temperature and relative humidity, until a specified contact force is reached. Then, it remains in contact with the prepreg for a given amount of time (dwell time), and subsequently, it is pulled away. During the retraction stage, force and displacement data are recorded to be further analyzed.

Figure 4.15 shows a typical normalized stress-displacement data obtained from the probe tack test (the figure is reproduced from previous work [61]). It can be seen in this figure that the stiffness and maximum traction can be directly measured using probe test. Two different criteria namely the fracture energy or the maximum separation can be used for characterizing the softening behavior of the traction-separation law. The maximum separation is directly measured during the test. Also, the fracture energy (i.e. the work of adhesion) can be easily obtained by calculating the area under the traction data. These three parameters are sufficient for fully defining the bilinear CZ traction-separation law.

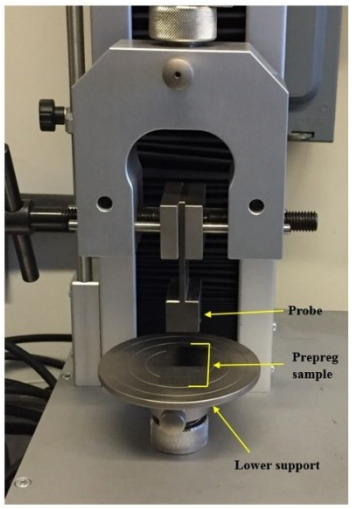

Figure 4.14 Probe tack test setup.

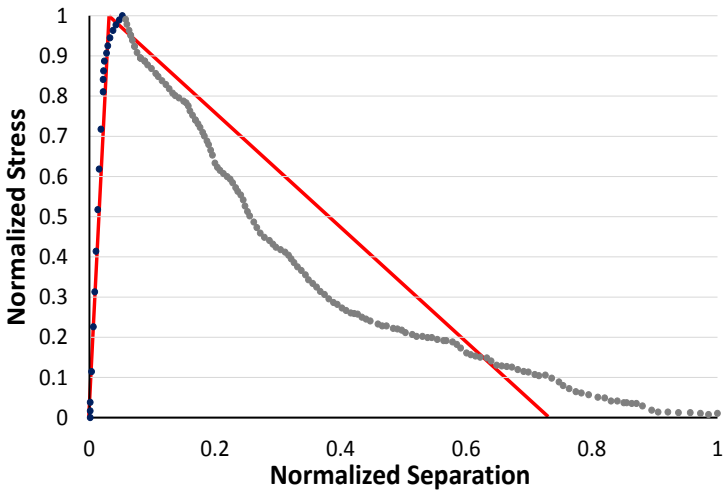

Figure 4.15 Typical result of probe tack test. Data points: experimentally measured data. Red line: fitted bilinear traction-separation law.

An important factor that affects the measured prepreg tack using the probe tack test remarkably is the dwell time during which the intimate contact between the prepreg surface and probe is established. Previous works on the subject [31, 35] have demonstrated the significance of the dwell time. Here, a contact mechanics approach is presented to determine the approximate contact time during which the compaction force is exerted on the prepreg and consequently, determine the appropriate dwell time for the probe test. Hertz theory provides the contact width θ of two solid cylinders in contact (Figure 4.16).

$$\theta = 2\left(\frac{4PR^*}{\pi E^*}\right)^{1/2} \tag{4.52}$$

where P is the compaction pressure per unit width of the compaction roller; R^* is the effective radius of contact given by $R^* = (1/R_1 + 1/R_2)^{-1}$, where R_1 and R_2 are the radii of the two cylinders in contact. E^* is the effective modulus and given by:

$$E^* = \left(\frac{1-\nu_1^2}{E_1} + \frac{1-\nu_2^2}{E_2}\right)^{-1} \tag{4.53}$$

Here, E_1 and E_2 are the elastic moduli of the cylinders in contact. The tool used in this study is flat ($R_2 \to \infty$). Moreover, the elastic modulus of the aluminum tool is much higher than that of the silicon rubber used in the compaction roller. Thereore equation (4.52) can be further simplified.

$$\theta = 4\sqrt{PR_{CR}(1-\nu_{CR}^2)/\pi E_{CR}} \tag{4.54}$$

The CR subscript in this equation stands for the Compaction Roller. This value was corroborated by the pictures taken during the AFP which clearly demonstrated the contact width at a known compaction pressure. Considering the linear speed of the AFP head to be V, the average contact time can be found $t_{ave} = \theta/V$.

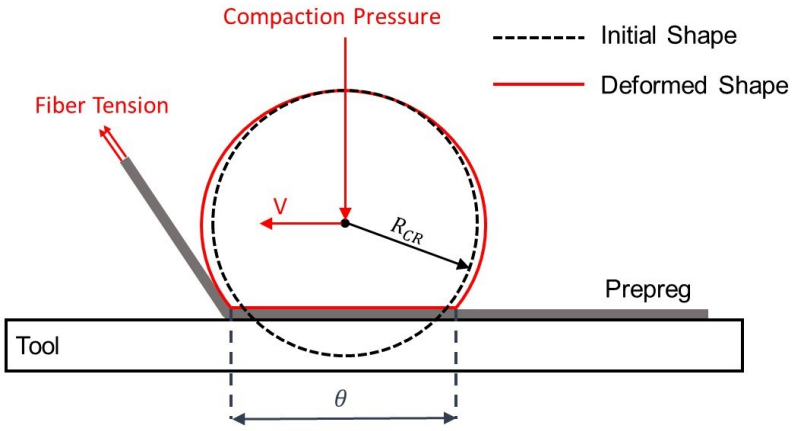

Figure 4.16 Deformed shape of the compaction roller in AFP.

The compression and retraction speeds (which are usually set to be equal) are found to have minimal effects on results of the probe tack test [35]. The more important test parameters are the relative humidity and the temperature. In order to obtain reliable results, the test should be conducted in an environment chamber where the relative humidity is set to be equal to that of AFP workshop, and the temperature is set to be the relevant prepreg temperature during the deposition. It should be noted that, although probe tack test provides a straightforward method for finding the required information for the model, it might be hard to relate some observations during this test to

the actual process parameters. In certain conditions, the effects of temperature on the prepreg tack measured through probe test might have some discrepancies to what actually occurs during the AFP. Increasing the temperature (which results in lowering the resin viscosity) in the probe test might cause the resin to flows away from the probe surface. In addition, during the AFP heat is usually dissipated from the tool shortly after the prepreg is laid down, while this is not the case in the probe test. Consequently, this method can underestimate tack for high temperatures. Developing a more reliable and comprehensive approach for characterizing model parameters of prepreg tack with regards to AFP will remain for future investigations.

5 RESULTS AND DISCUSSIONS

Results from the developed models as well as relevant discussions on the models will be presented in this chapter. As described in section 4.3, uncured prepreg mechanical properties are required for evaluating the models. These properties are characterized as discussed and presented in Table 5.1.

Table 5.1 Mechanical properties of the uncured prepreg and compaction roller (CR) [61].

$\boldsymbol{E_1}$ (GPa)	$\boldsymbol{E_2}$ (MPa)	$\boldsymbol{G_{12}}$ (MPa)	$\boldsymbol{\nu_{12}}$	$\boldsymbol{E_{CR}}$ (Durometer)	$\boldsymbol{\nu_{CR}}$
31	0.046	3.025	0.2	60	0.49

In the table, E_1 is the on-axis or longitudinal modulus, E_2 is the off-axis or transverse modulus, G_{12} is the in-plane modulus and ν_{12} is the in-plane Poisson's ratio that have been characterized as discussed. The longitudinal elastic modulus of the material system used is 31 GPa. Such a low value for the on-axis modulus of the prepreg is a result of in-plane fiber waviness the carbon fiber within prepreg materials *inherently* possess. When subjected to external load, carbon fibers which are embedded in the compliant b-stage resin can easily deform, hence resulting in longitudinal elastic modulus that is significantly smaller than that of cured prepregs. It is the relatively high stiffness of the cured resin that provides the required load transfer among fibers, which in turn makes the composite lamina to have such a high stiffness levels.

Moreover, in the literature, [60] have performed a clamped beam test with a light weight applied at the free end of the prepreg tow. The displacement of the free end of the uncured prepreg tow was measured and Euler-Bernoulli beam theory was used to find the longitudinal elastic modulus from the displacement. $E_1 = 30\ (GPa)$ was reported which is consistent with the value used in the present study.

5.1 LOCAL MODEL

5.1.1 Viscoelastic Model

At any given time, the wrinkle length can be found by solving equations (4.25) and (4.26), simultaneously. The unknown parameters of the Prony series should be found by fitting the theoretical model to the experimentally measured data. Here, the long term modulus was found to be $k_\infty = 3.89\ E9\ (N/m^3)$. Furthermore, one term from the series was sufficient to capture the time-dependent behavior of the wrinkle. The relaxation time was found to be $\tau_1 = 6\ (1/s)$ $and\ k_1 = 70\ E9\ (N/m^3)$. The wrinkle length measured experimentally and the fitted model are presented in Figure 5.1.

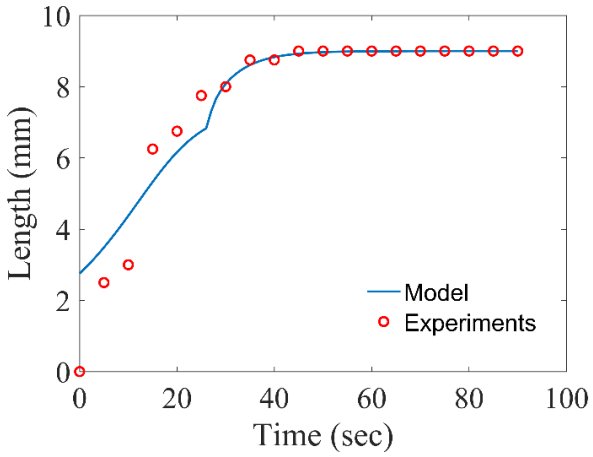

Figure 5.1 The wrinkle length as a function of time.

Figure 5.1 shows that the model developed in this work is well capable of capturing the length of wrinkles with time. The first practical implication of this model is in the characterization of the prepreg tack. As was thoroughly discussed in 4.3, the stiffness of the foundation (tack) is usually characterized with a probe tack test. As a result of the rate-dependency of the viscoelastic properties of the interface (which is described in the present work with Prony series, equation (4.1)), the stiffness measured through the probe test is rate dependent.

The dwell time of the probe test is important in establishing the true area of contact at the interface and hence determining the adhesive strength of the prepreg-tool interface. Therefore, the dwell

time should be determined based on the velocity of the AFP head and stiffness of the compaction roller (see section 4.3.2.3 for more details).

Therefore, the measured quantity is indeed closer to the instantaneous stiffness which is larger than the relaxed stiffness. This increased level of stiffness causes the local models to consistently under-predict the wrinkle wavelength (Figure 5.2) and over-predict the critical steering radius in comparison to the real AFP layups. When the interface is stiffer than what it should be, tighter steering radii can be achieved and in case of local tow buckling, fewer wrinkles would appear. In a given length of prepreg tow, the fewer number of wrinkles means larger wavelength predicted by the model. It is demonstrated through the developed model in the present study that the interface gradually relaxes facilitating the appearance of wrinkles with time.

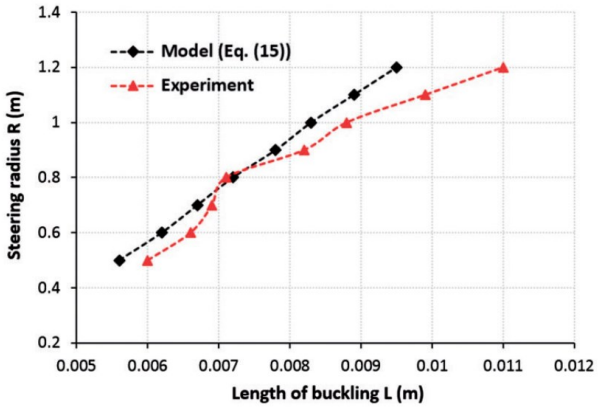

Figure 5.2 Wrinkle wavelength as a function of steering radius: experiment versus elastic local models [61].

Additionally, to further increase the efficiency and productivity in manufacturing of composite materials using the AFP technology, the processing windows should be further extended (e.g. increasing layup speed which potentially results in lower prepreg tack levels, ergo more defect prone layup). One potential way for attaining this objective is better understanding the effect of the deposition of subsequent layers on an initially defective layup, and the interaction of the compaction roller with a wrinkle. The first step was to model the length of the defect. In the future studies, the interaction of subsequent layers and more importantly the compaction roller with the defects will be investigated.

5.1.2 Elastic Modeling of Blisters

In the present section an elaborate discussion will be presented to refute the idea that the formation of blisters, similar to wrinkles, could be driven by a buckling mechanisms to release the excessive levels of energy stored in the tow. More in-depth discussions on the origins of blisters will be presented in sections 5.2 and 6.

5.1.2.1 Setting boundaries for the load parameter

The local models use a linearly distributed load (*stress resultant* in terms of composite laminate terminology) on the edge of the representative plate to simulate the load distribution that is induced in a prepreg tow as a result of tow steering in the AFP process: $N_{xx}(y) = P_0(1 - \alpha y/b)$. Where the P_0 [N/m] is the maximum load, b [m] is the tow width, y is the coordinate along with the tow width and α is an arbitrary parameter ($\alpha \in [0, 2]$) that determines the load distribution. As an example $\alpha = 2$ results in pure bending of the representative plate, $\alpha = 1$ the plate is experiencing no stress at its outside edge and P_0 at the inside edge, and for $\alpha = 0$ the plate is uniformly under compression.

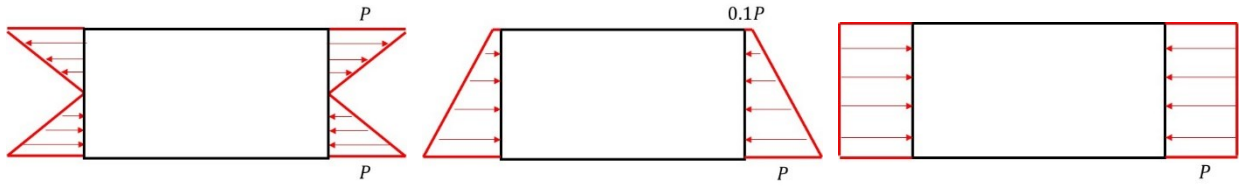

$\alpha = 2$ $\alpha = 0.9$ $\alpha = 0$

Figure 5.3 Load parameter $\boldsymbol{\alpha}$ and the resulting distributions.

Since the dominant mode of deformation during steering of AFP head is incremental tow bending, it can be expected that α should be chosen close to 2 (pure bending condition). Indeed previous studies on *wrinkle formation* have found that $\alpha = 2$ produces the best results in the models and consequently, have used this value in their analyses [59-61].

In order to analyze blisters as a local buckling mechanism a lower bound is required to be found on α (the reason will be elucidated later in the next section). On an idealized prepreg plate, three parameters affect and together determine α. As the prepreg tow is laid down, it is being

incrementally bended by the roller to follow a certain steering radius ($\alpha = 2$ induced). At the same time, the compressed fibers micro-buckle and form in-plane waviness. This causes a reduction of the effective prepreg stiffness at the inside edge of prepreg tow, in comparison to its outside edge which has remained straight (see 2.3.2.1). Finally, AFP head exerts a usually small level of tension on the prepreg tow in order to keep them straight in the prepreg delivery system (i.e. fiber tension). This may also result in some residual tension in the tow. The energy analysis proposed by Hörmann [51] can predict the position of neutral axis of a steered tow containing in-plane fiber waviness. Further, by considering that neutral axis is the axis were the stress is equal to zero, the position of neutral axis can be related to the load parameter:

$$N_{xx}(y) = 0 \;\rightarrow\; \alpha = \frac{b}{y_{N.A.}} \tag{5.1}$$

The model is solved with the material properties relevant to the present work. The final result of the model (Figure 5.4) is presented as a three dimensional graph depicting the total strain energy of the plate as a function of degree of fiber waviness and distance of neutral axis from the symmetry axis (mid-plane). The state of system that can naturally occurs is at neutral axis and degree of fiber waviness were the total strain energy is at its minimum. From this state the position of neutral axis is found which results in $\alpha = 1.33$ for the present problem.

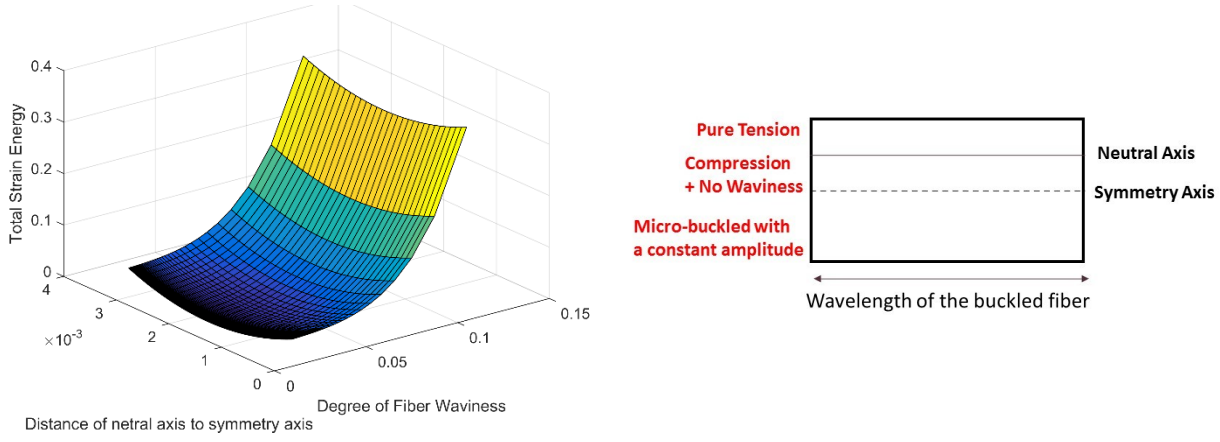

Figure 5.4 Total strain energy of a plate containing in-plane fiber waviness and model summary.

Fiber tension is a small load which further moves the neutral axis *closer* to the inside edge of prepreg (increases α). Moreover, as we are only interested in finding an approximate lower bound for α, the influence of fiber tension is neglected. Consequently, the load parameter can only take values in $[1.33, 2]$ limits.

5.1.2.2 Discussion on the Blister Model

Figure 5.5 demonstrates the variation of critical steering radii against α for wrinkles (CCSF plate) and blisters (CCCC and SSSS plates). As it can be seen, at its optimum value which is typically used, $\alpha = 2$, the local model is predicting critical steering radius of 130 cm, meaning above 130 cm wrinkles do not appear which is consistent with experimental observations in [61]. At this value of α the blister models are predicting the critical steering radius of 0, which means that the model is predicting the blisters never occur. This is in contradiction with experimental observations (e.g. Figure 3.8) where blisters and wrinkles have appeared at the same time.

Considering smaller values of α, the fact that critical steering radius of wrinkles is higher than SSSS blisters (for $0.85 \leq \alpha \leq 2$) indicates that formation of wrinkles are more natural (lower energy levels) to release excessive levels of energy through buckling. It is only for $\alpha < 0.85$ where the critical steering radius of SSSS blisters are larger than that of wrinkles. In these situations, the whole width of the prepreg tow is under compression (see Figure 5.2) which cannot be the case during the AFP process as it is clear from the deformation of prepreg tows and also from the theoretical lower bound established in the previous section.

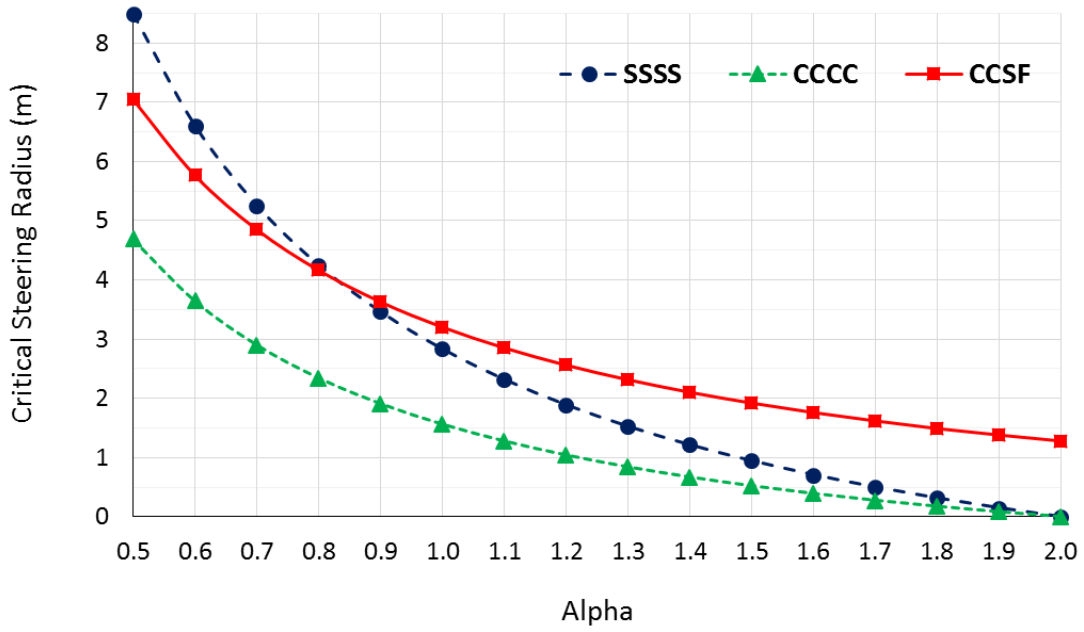

Figure 5.5 Critical steering radii versus alpha.

From the presented discussion, the load distribution on prepreg tows is such that wrinkle formation is the natural way of releasing energy *through buckling*. For blisters to occur as a result of buckling, the whole tow width should be under compression with the magnitude of load at outer diameter to be at least 15% of the magnitude of load at its inner edge, a condition that cannot happen during tow steering in AFP. Essentially, stress levels are not high enough to drive the formation of blisters through a plate buckling mechanism.

5.2 GLOBAL MODEL

Two cases with identical process parameters but different radii are presented in this section to demonstrate the capabilities of the finite element model. The AFP process parameters used for these two configurations and the interface parameters inputted to the finite element models are presented in Table 5.2. Using the roller's mechanical properties, the applied compaction force and equation (4.54), the contact width is calculated to be 14.489 mm. Therefore, given the speed of the deposition process, the average contact time during which any section of prepreg tow experiences pressure is 0.1 (sec). With the relative humidity of 30% and the prepreg surface temperature of 50 °C, the interface parameters are obtained from [35] and presented in Table 5.3. It should be noted that the temperature available in Table 5.2, is the temperature of the Nitrogen gas at the end of the nozzle while the exact temperature of the tow surface in contact with the tool surface is not available. Based on previous experience [61] and considering the high thermal conductivity of the Aluminum tool, it is expected that most of the heat is dissipated promptly and a temperature around 40-50 °C is achieved on the prepreg surface.

Table 5.2 Process conditions.

Nitrogen Temperature (°C)	Nitrogen Flow Rate (lit/s)	Head Speed (mm/s)	Compaction Force (N)
260	85	140	222.4 (50 lb)

Table 5.3 Interface parameters for process conditions of Table 5.2.

K (N/mm^3)	Maximum Stress (MPa)	Fracture Energy (N/mm)
3.2923	0.3852	0.00868

The first case presented here is performed with the steering radius of 889 mm (35 in). As described in 3, a very good layup quality can be achieved for this radius with the presented process parameters (Figure 3.3). The picture of resulting experiment is provided here again for easier comparison. The results of the simulation are depicted in Figure 5.6. The output demonstrated in

this figure is the stress level at the interface which is normalized by the maximum tolerable stress (stress of the damage initiation criteria). The maximum value of the output is 68%, meaning that the interface has indeed remained completely intact. A very good layup quality is obtained in the simulation as was expected considering the experimental results.

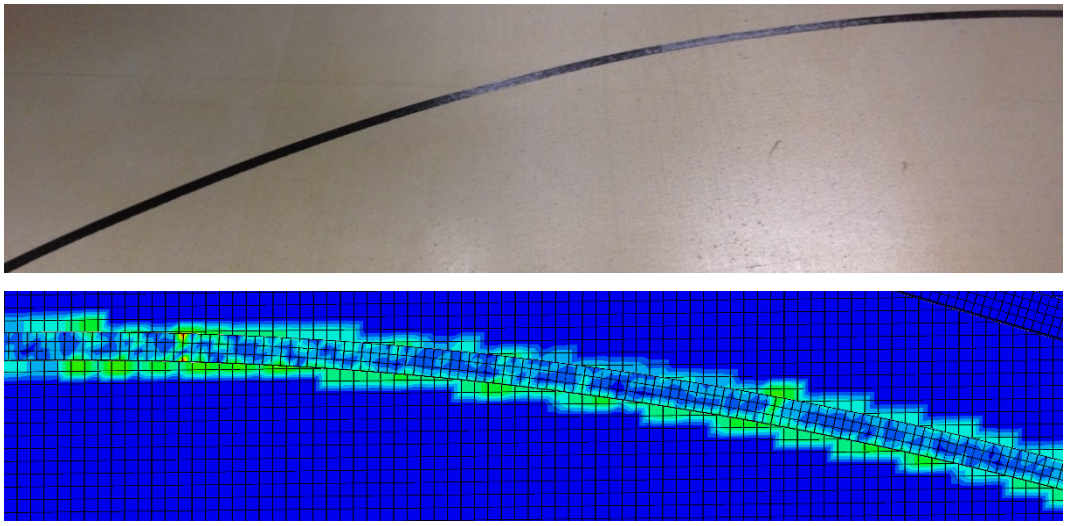

Figure 5.6 Experiment and simulation of prepreg tow steered with 889 mm radius. No significant defect is observable in simulations and experiments.

Keeping the process parameters constant, the steering radius is decreased to further investigate the formation of out-of-plane wrinkles and blisters. The on-axis stress distribution for a commonplace result of the simulations is presented in Figure 5.7. As demonstrated in this figure, the outside edge of the prepreg tow is under severe tensile stress. This tensile stress has two origins: the fiber tension force that is exerted on the free end of the tow which partly helps in keeping the loose tow straight (in reality this load is indeed induced in the prepreg tow in the delivery system), and the tensile stress that is induced as a result of fiber steering (bending stress). In the viewpoint of Figure 5.7, two wrinkles appear. It is evident that compressive stress is built up at the inside edge of the tow between the two wrinkles. More importantly, small low-stress zones are visible in the vicinity of both wrinkles indicating that wrinkles are indeed acting as a stress relief mechanism.

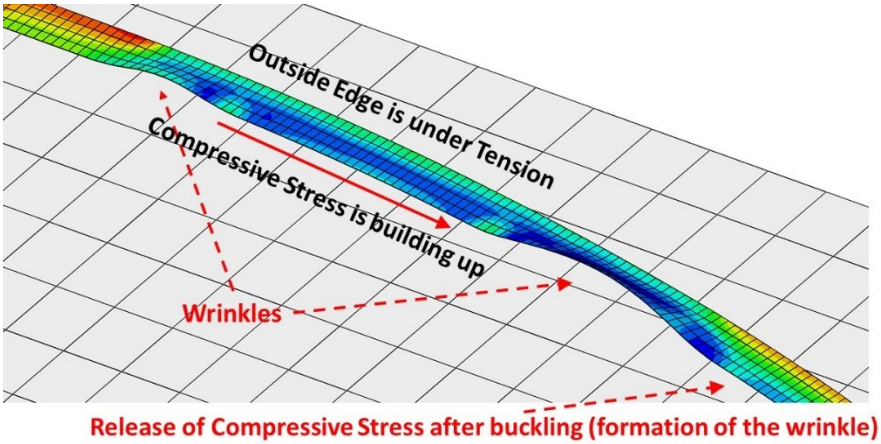

Figure 5.7 Stress distribution in a common place result for the simulations of defective layups.

In order to validate the simulation results, it is performed with the 558.8 mm (22 in) steering radius, corresponding to the case 6 of 3 and Figure 3.8 of the experimental results. The result of the simulation is presented in Figure 5.8 (again the resulting AFP trial is presented for easier comparison). The output presented in this figure is the same as that of Figure 5.6 (normalized stress at the interface). The deformed shape of the prepreg tow elucidates that the proposed global prepreg deposition modeling is capable of capturing the out-of-plane buckling of the tow (i.e. the wrinkles). Furthermore, as it is distinguished in Figure 5.8 by yellow circles, several small zones are formed that have reached the damage initiation criterion, however, the damage in these elements has not progressed more than 10-50%. The red color represents the areas where the damage initiation criterion of the traction-separation law is met. These areas at the middle of the tow-width, that have not completely buckled yet (i.e. the damage has not evolved 100% and consequently, wrinkles are not formed) correspond to the blister zones of experimental results. In the simulation, the wrinkles are clearly distinguished by the large out-of-plane deformation of the tow while the blister zones look intact. The blister zones have a damaged interface which potentially causes the blisters to appear in practice.

A comparison of the simulation results with the experiments, show an excellent agreement in patterns and frequencies of both blisters and wrinkles. Meaning that not only the finite element model is capable of capturing the blisters and wrinkles, but also blisters are in fact mainly

originated from the stress distribution induced as a result of fiber steering, and interface failure (i.e. not sufficient levels of tack).

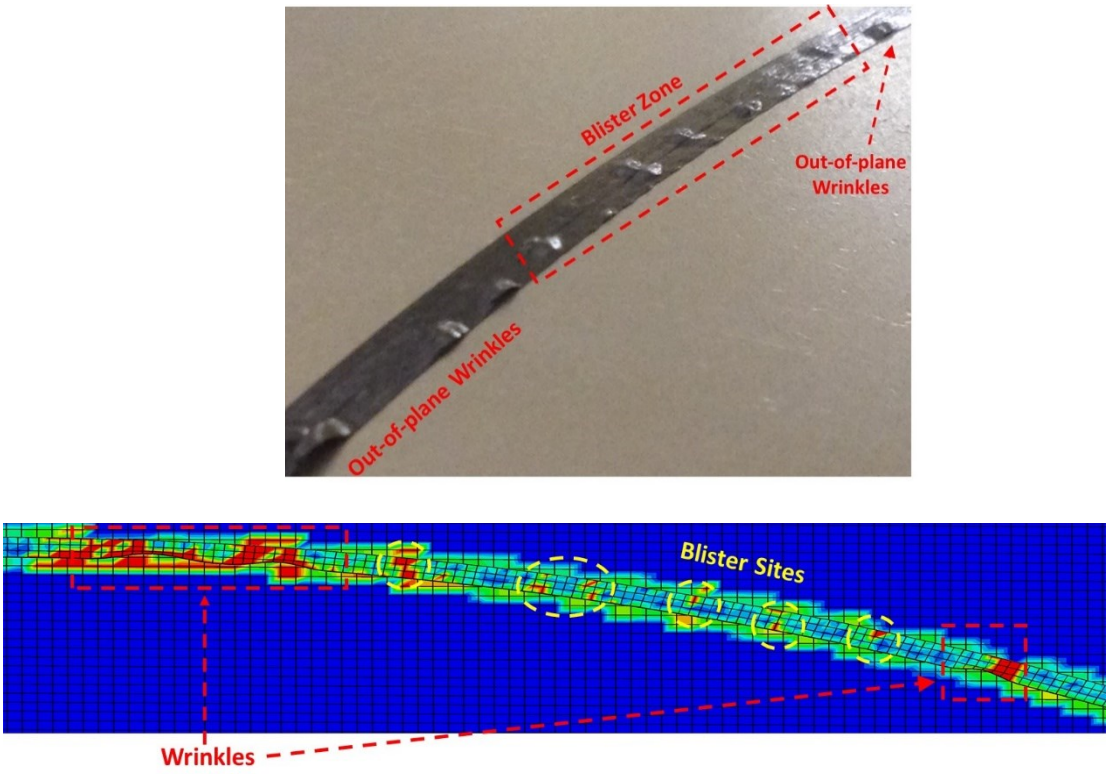

Figure 5.8 Simulation of blisters and out-of-plane wrinkles with 558.8 mm steering radius.

6 EFFECT OF COMPACTION ROLLER

In the previous chapters, the influence of interface stresses in the formation of blisters were discussed. Moreover, it was demonstrated that the stress distribution in the cross section of prepreg tow is such that the *local tow buckling* can only contribute as a stress release mechanism by the formation of out-of-plane wrinkles. In other words, blister formation cannot be driven by buckling of the tow. In the present chapter, the interaction of compaction roller with prepreg tow in the vicinity of tool surface will be considered to further understand the processes contributing to the formation of blisters.

AFP machines utilize a compaction roller to lay down prepreg tows onto the tool surface. For the deposition of thermoplastic tapes, temperatures above 400 °C are required to facilitate molecular interdiffusion, in order to achieve good interplay bonding. Consequently, the roller must be able to sustain high temperatures the tapes are exposed to. Steel is the most widely used material for the processing of thermoplastic matrix composites. For the thermosetting matrix composites, however, AFP or ATL only produce an intermediary product that should be further consolidated and cured inside an oven or an autoclave. During the prepreg tow deposition, process temperature cannot exceed ~60-70 °C in order to prevent initiation of curing inside the resin. The primary function of compaction rollers in the AFP of thermosetting prepregs is to facilitate the development of appropriate levels of tack and to keep the voids between prepreg tows as small as possible. The perfect condition is the fully compacted and void free lay-up.

In addition to using compliant materials that are capable of conforming to the curvature of the tool surface, other strategies have been used to increase the proficiency of rollers. Some rollers have a perforated architecture for further helping them to deform. Moreover, for the rollers in the AFP heads that are able to deliver larger number of tows in each course, *segmented* rollers have be used.

To demonstrate the application of segmented rollers, one design documented in patent [76] is presented as an example. Complete compacting device is depicted in Figure 6.1 (a), with its cross-sectional view in (b). The device is comprised of a frame, a fluid supplying system, a rectangular shaft connecting two ends of the frame and number of narrow roller segments. Each segments has a ball bearing to facilitate its rotation. Outside of the outer race of the bearing, roller's flexible

cover is located. Inside of the bearing, an empty space exists which can accommodate the shaft and two bladders. This space allows each segment to move in and out *on its own*, thus compacting prepreg tows without regard to the adjacent segments. The bladders can be connected to an external source of fluid or pressure, otherwise, they should be filled with a non-compressible fluid such as silicone gel or hydraulic fluid.

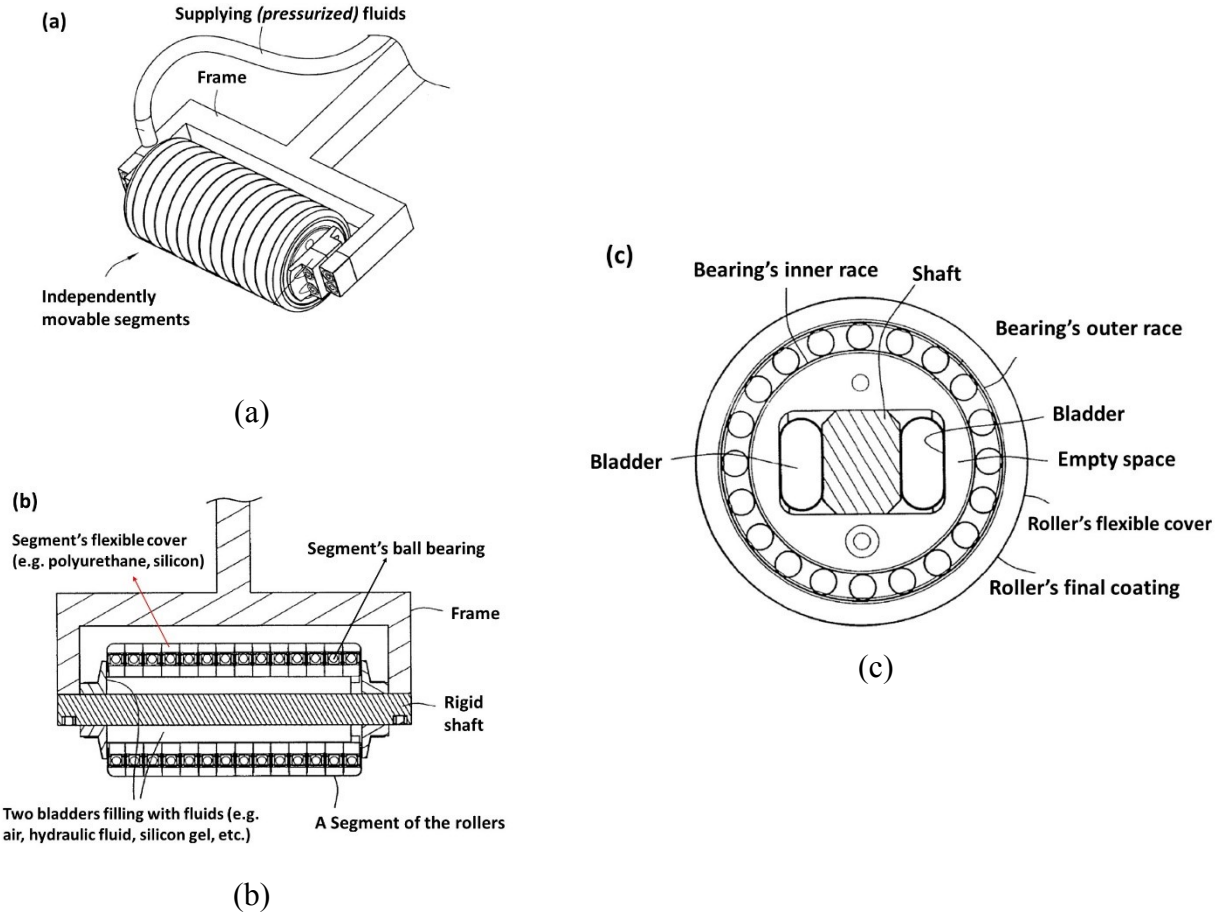

Figure 6.1 An example of segmented compaction rollers
a. isometric view; b. cross-sectional view; c. each roller.

Smaller AFP heads that are not responsible for delivering large courses, typically utilize rollers that are in one piece, solid or perforated. The main objective is to provide a more uniform pressure distribution and enhanced flexibility. The perforated structure of the roller, in theory, should help it to deform more easily, hence providing a larger contact area, increasing the dwell time, and providing a more uniform pressure distribution, all of which should facilitate having a more suitable interface for the formation of tack.

The interaction between roller and prepreg tow is very critical in the initiation and formation of defects. The primary objective in the present chapter is to investigate effects of the roller, its stiffness and its architecture (perforated or solid), on the steering-induced defects particularly blisters that appear in the middle of the prepreg tows during the process. The standard roller used for depositing thermosetting prepreg tows in the Automated Dynamics' Fiber Placement machines is a perforated, 60 durometer polyurethane roller as shown in Figure 6.2. The existing roller is comprised of two different sections, an Aluminum kernel which is mounted on the AFP head and a polyurethane tube that is fitted rigidly on the metal kernel.

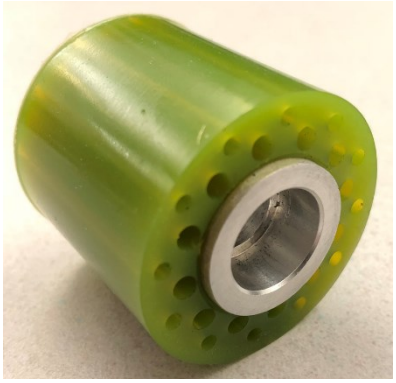

Figure 6.2 A typical perforated roller for placing thermosetting prepreg tows.

Three different polyurethane tubes with inner diameter of 20 mm, outer diameter of 38 mm, and hardness of 35, 60 and 85 durometer were supplied from the Western Roller Corporation. The tubes were cut in 35 mm long pieces, which is the length of the roller, constrained by the geometrical features of the AFP head. The rigid metal kernel is machined out of Aluminum with

the outer diameter of 21 mm, inner diameter of 14 mm and length of 38.8 mm. One hole with 14 mm diameter and 7.8 mm depth is drilled on each side of the kernel which are meant to accommodate the bearings. The kernels are put inside a freezer for about 2 hours so their outer diameter becomes approximately the same as the inner diameter of the polyurethane tubes, and subsequently, they are fitted inside the tubes. In order to mount the rollers on the AFP head, two ball bearings (one simple and one flanged) are put inside the 14 mm holes of each side of the kernel. A threaded pin goes through the ball bearings and the kernel. Finally, the threaded pin will be attached to the bracket of the AFP head using a mechanical screw.

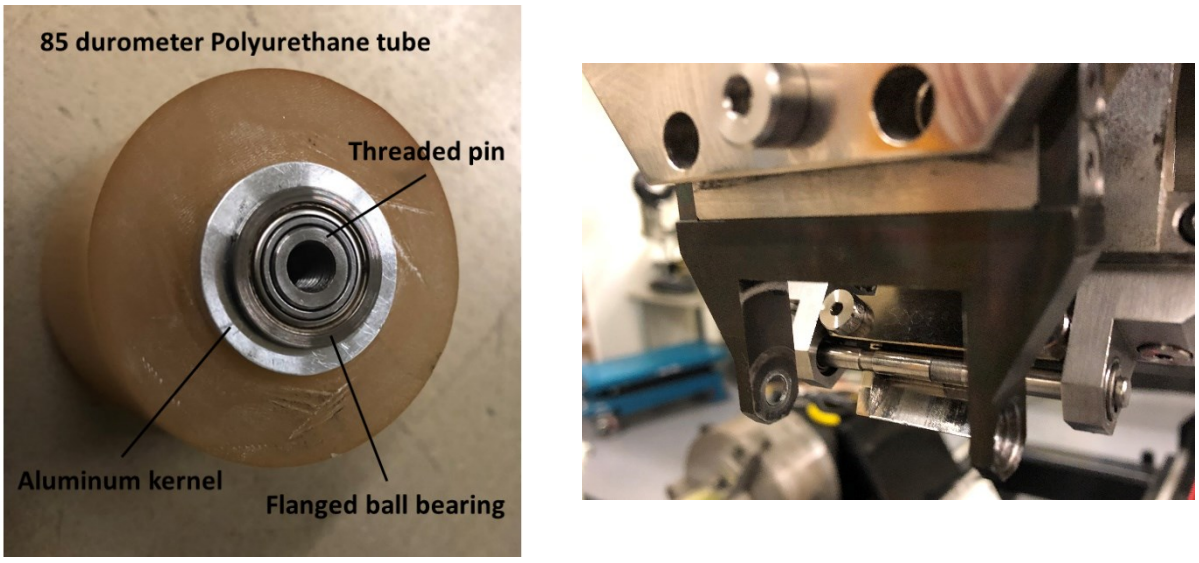

Figure 6.3 Left: assembly of the roller; right: bracket responsible for holding the roller.

In addition to the polyurethane rollers, a fully stainless-steel roller is machined to further study the effect of high roller stiffness and surface material (the drawings are available in Appendix B: Compaction Rollers and picture of rollers are depicted in Figure 6.4). Since the metal roller will not undergo any significant deformations, fiberglass Tooltek tape can be applied to the roller surface to control for the contribution of surface energies in tack between the roller and prepreg.

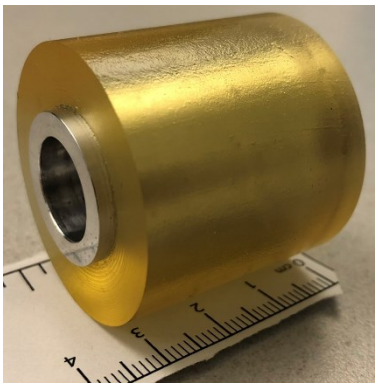

a. 35 durometer

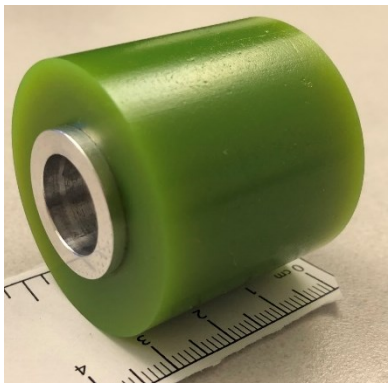

b. Solid 60 durometer

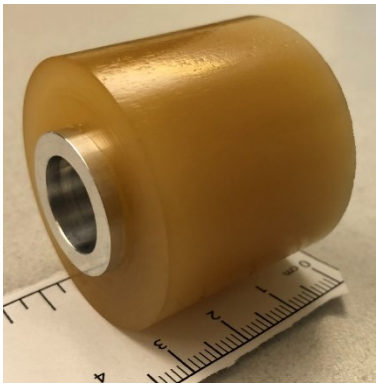

c. 85 durometer

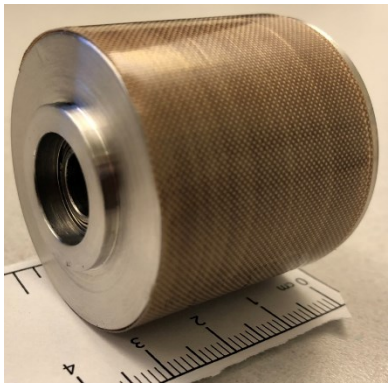

d. Stainless steel roller with tooltek

Figure 6.4 Solid rollers for placing thermosetting prepreg tows.

6.1 STATIC DEFORMATION ANALYSIS

In an AFP head, the tow delivery system feeds the prepreg tow to the roller and the roller, which is following a prescribed path with a given speed, places the material applying a predefined compaction force. In this process, the roller itself can influence the development of prepreg tack through the pressure distribution they produce on the prepreg tows and through influencing the average time during which the pressure is maintained on the tows.

How the AFP head's compaction force is transmitted to the compaction pressure prepreg experiences is determined by the roller material's stiffness and its architecture. For example, a solid stainless steel roller will have a *line contact* with the prepreg which produces a very high and

sharply distributed pressure over a very short distance. On the contrary, under the same amount of force, a more compliant material produces a smoother and lower pressure distributed over a larger area of contact. Moreover, for a given speed, the contact width the roller is able to provide, largely determines the average time during which each segment of a prepreg tow is subjected to the compaction pressure, to develop the intimate contact necessary for having a strong tack. In order to gain deeper insights into the behavior of each roller during the AFP process, their deformations and contact pressure distributions are investigated through performing static tests and developing finite element simulations.

6.1.1 Static Testing

A tensile testing machine with a 1 kN load cell is used to measure the contact width of the rollers and to obtain their force displacement behavior. Figure 6.5 depicts how the roller is mounted on the top fixture and is pressed against a rigid flat fixture.

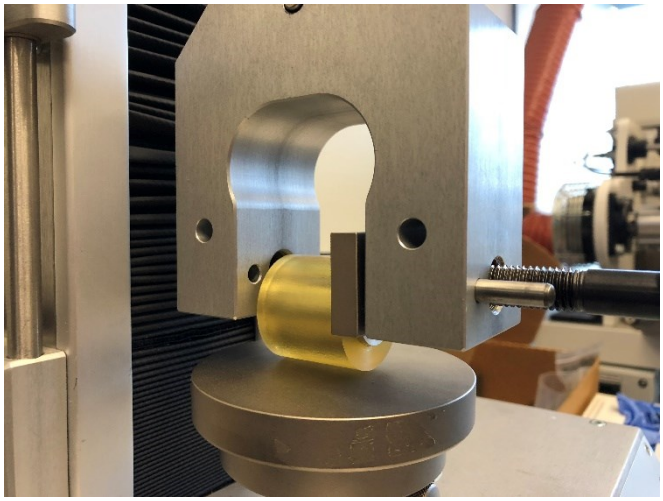

Figure 6.5 Static testing setup.

It was demonstrated in chapter 3 that when steering prepreg tows, 222.4 N or 50 lbf is the optimum compaction force, providing a balance between creating intimate contact without causing too much resin distribution. In the first step, the rollers are compressed up to 350 N (78 lbf) to obtain the

force versus vertical displacement behavior of the rollers, result of which are presented in Figure 6.4. Approximately below 20 N, all rollers deform nonlinearly. However, with increasing the applied load, the exhibited force-displacement behavior is linear. From the linear trendlines fitted to the experimental data, it can be concluded that the overall behavior of polyurethane rollers can be considered linear for engineering purposes (which was also observed in [77]).

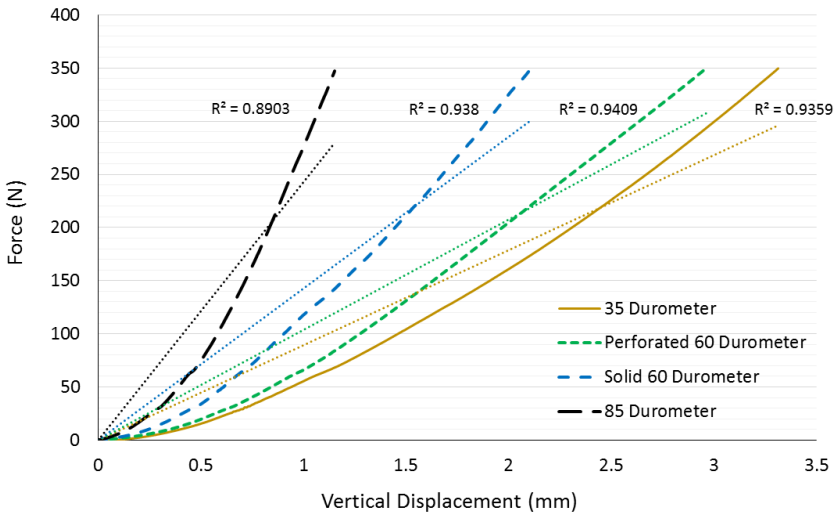

Figure 6.6 Force-displacement of rollers.

In this study, the contact width under 222.4 N will be used (in the next section) to validate finite element simulations. A thin paper ruler is affixed on the flat fixture, perpendicular to the roller axis. The tensile testing machine was programmed to compress the roller and remain at 222.4 N. The contact width was subsequently measured with 1 mm accuracy (Figure 6.7). The measured contact widths are presented in Table 6.1. The contact width of the 35 durometer roller is found to be the same as the perforated 60 durometer one and they both reach the largest width of contact among different rollers. As expected, higher hardness is translated into smaller contact width for the solid rollers.

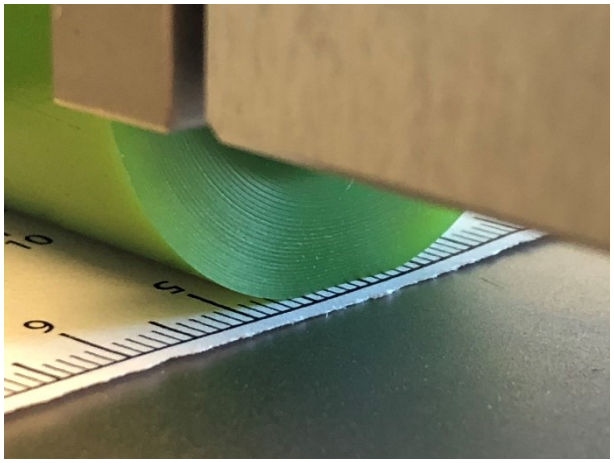

Figure 6.7 Example of contact width measurement under 222.4 N.

Table 6.1 Experimental contact width under 222.4 N (50 lbf).

Roller Hardness (Durometer)	Contact width (mm)
35	14
60, Perforated	14
60, Solid	11
85	4
Stainless Steel	Line Contact

6.1.2 Simulations

In this section, the static experiment is simulated in the commercial finite element package Abaqus. The roller and aluminum kernel are modeled with their actual dimensions. Three dimensional C3D8R brick elements are used for discretizing the roller. Elements sizes from 0.5 mm to 0.1 mm were tried for the roller as a convergence study. It was found that 0.5 mm meshes are capable of producing accurate results. However, 0.2 mm ones were found to be required for the perforated roller because of the small regions, and in the 85 durometer one because of the small contact area.

As a result of the large difference in stiffness between the polyurethane roller and Aluminum kernel, and the fact that the aluminum kernel does not contribute to the overall deformation of the rollers, the kernel is modeled as a three dimensional rigid shell. The flat fixture is modeled as a two dimensional rigid plate and it is discretized using discrete rigid, R3D4 elements. The mesh size should be small enough to prevent penetration of the roller into the fixture. The mesh size of 0.5 mm was found to be sufficient for this purpose. The final assembled and meshed model of a solid roller is presented in Figure 6.8, as an example.

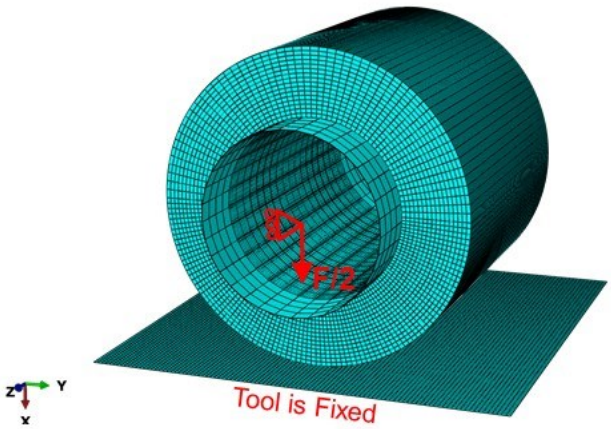

Figure 6.8 Meshed and assembled model of the static testing of rollers.

The internal surface of the roller is tied to the outer surface of the kernel. Two concentrated forces are applied at the center of each end of the cylindrical kernel. Additionally, all of its boundary conditions, except the direction in which the forces are applied (perpendicular to the flat plate), are constrained. All degrees of freedom of the rigid plate representing the flat fixture are constrained. A frictionless hard contact is defined between the roller surface and the rigid plate to simulate the contact. Finally, the problem was solved using the standard Abaqus algorithm.

The line of initial contact between the roller and fixture is important in the perforated roller. Based on the architecture of the perforated roller, three different cases (identified with A, B and C) were chosen to be simulated, in order to study the effect of roller's position on the pressure distribution. These three cases are presented in Figure 6.9.

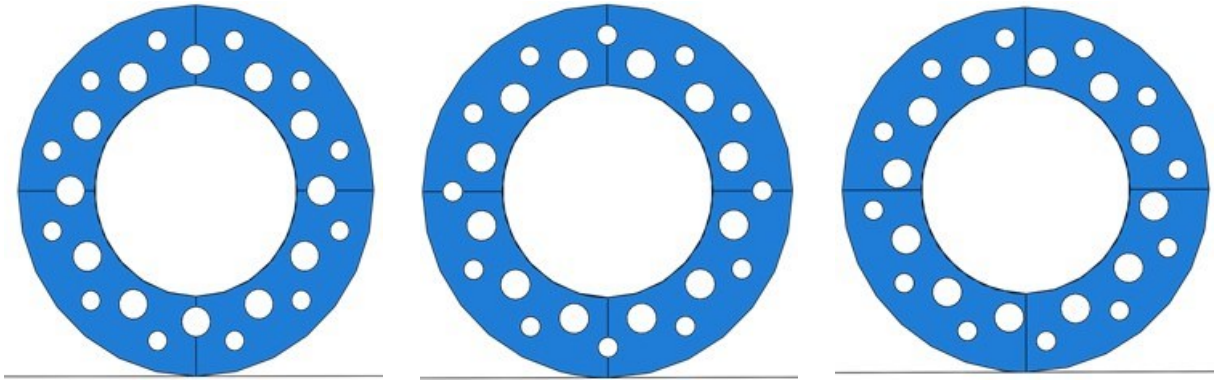

Figure 6.9 Different positions of the perforated roller during the simulations.

Highly deformable polyurethane tubes are usually categorized based on their shore A (or shore D) hardness instead of their stiffness. Equation (6.1) presents an engineering relationship between the logarithms of the elastic modulus and the shore A hardness of the elastomers and elastomer-like materials [78].

$$\log_{10} E = 0.0235\, S - 06403 \tag{6.1}$$

In this equation, E is the elastic modulus in MPa and S is the shore A hardness of the elastomer in durometer. The values obtained by this formula were used as a first approximation of the elastic modulus of polyurethane tubes. The width of contact obtained from the simulations were compared with their corresponding experimental value. Since, this formula is an approximation, maximum difference of 20% was obtained among the contact widths of different rollers between the experimental values and the ones obtained from simulations. Consequently, a few iterations were performed in each case to find more accurate values of the elastic modulus and to have the finite element models validated against the experiments. Initial estimations and the final values of the elastic moduli are presented in Table 6.2.

Table 6.2 Conversion of hardness to elastic modulus.

Hardness (Durometer)	35	60	85
Initial Estimate from (6.1)	1.5	5.9	22.8
Final Value Used	3.0	5.50	35.0

Simulation versus real deformation of the perforated 60 durometer roller in different initial conditions and subjected to 222.4 N is presented Figure 6.10. In addition, distribution of the compaction pressure along the length of the roller, under 222.4 N is presented in Figure 6.11.

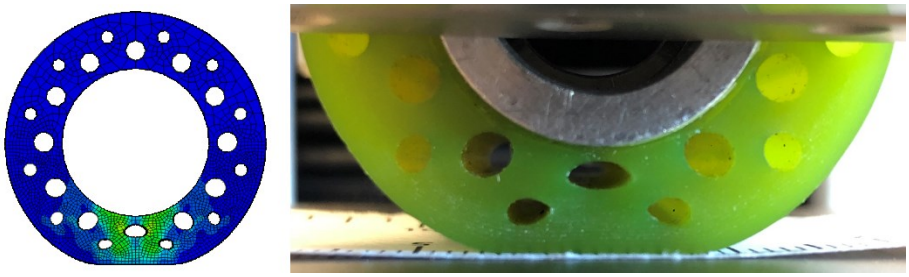

Case A

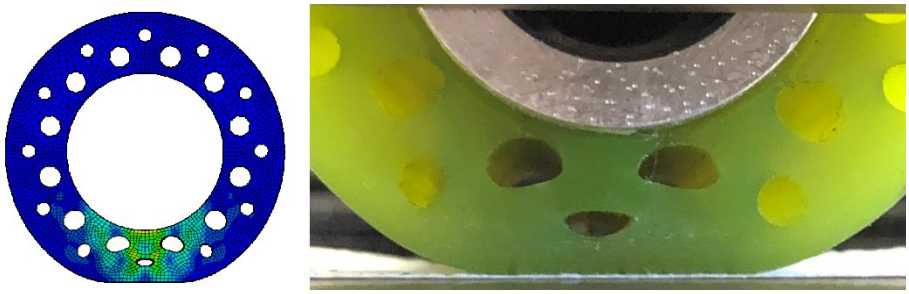

Case B

Figure 6.10 Simulation versus real deformation of the perforated 60 durometer roller under 222.4 N or 50 lbf.

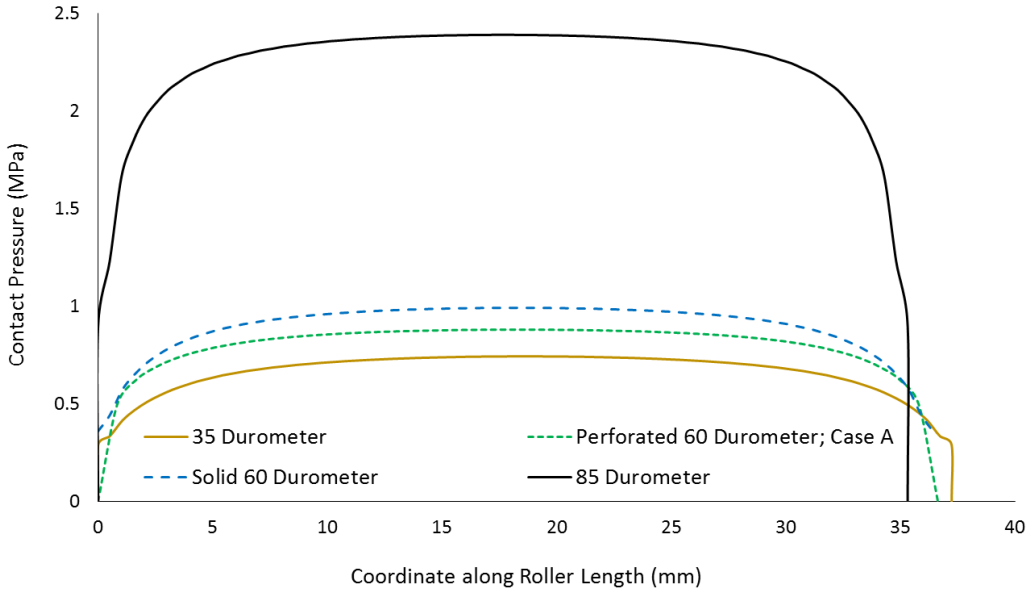

Figure 6.11 Compaction pressure distribution along the length of the rollers.

Under the same amount of compaction force, the high modulus of the 85 durometer roller results in a small contact area and consequently, a higher pressure in comparison to the other rollers. More interestingly, is the distribution of compaction pressure along the width of contact. Figure 6.12 presents this distribution for the solid rollers, while Figure 6.13 presents the distribution for the perforated and solid 60 durometer rollers. In Figure 6.12, it is clear that again, the small contact area in the 85 durometer roller is producing a much higher compaction pressure, with a very sharp increase in the intensity. The 35 durometer roller, on the other hand, provides a very smooth and evenly distributed pressure over the whole width of contact. The solid 60 durometer roller is the median case between the two. Having 20% smaller contact width compared to the 35 durometer roller, the pressure reaches slightly higher values with a sharper rise from the edges to the center of contact.

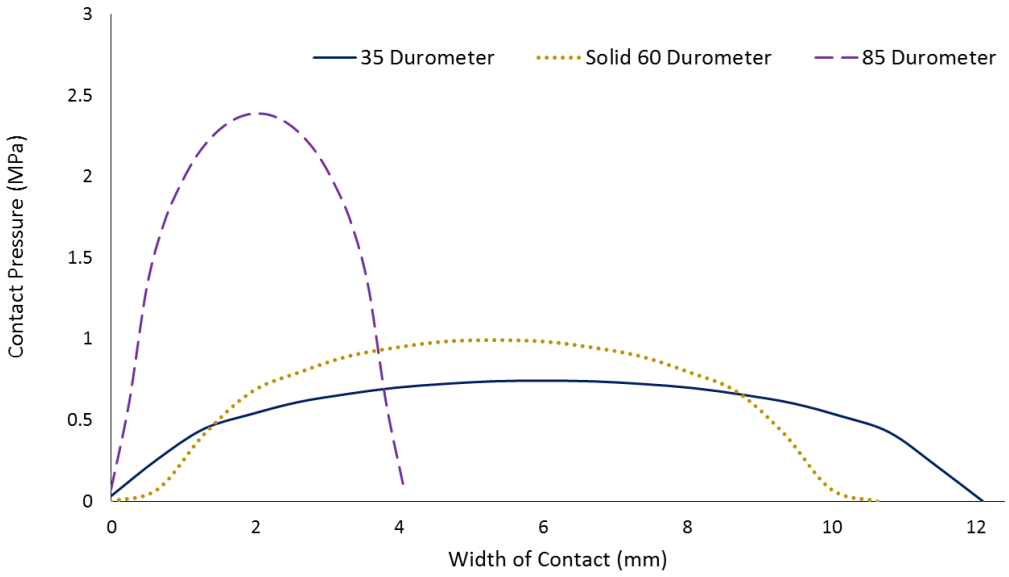

Figure 6.12 Compaction pressure distribution along the contact width in the solid rollers.

Figure 6.13 demonstrates a comparison between the compaction pressure distribution provided by three different cases of the perforated 60 durometer roller, and the solid 60 durometer roller. In case B where the hole is closer to the periphery of the roller, a smaller local pressure is required to locally deform that section to make it follow the overall deformation of the roller. In case A, however, the hole is much closer to the metal kernel. Therefore, the local pressure which is needed to produce the required deformation is higher.

AFP head is ideally moving at high speeds for maximizing process productivity. Each arbitrary segment of the prepreg tow is deposited by some place on the periphery of the compaction roller, which is happened to be at center of the contact width at that specific moment. Consequently, each arbitrary segment of the prepreg tow is *primarily* (although not entirely) subjected to compaction pressure under positions A or B of the perforated roller (or somewhere in-between, such as C), when that position is at the middle of the contact width.

The local fluctuations of the compaction pressure which can be observed at the middle of the contact width in Figure 6.13, essentially causes different locations of the prepreg tow (along its length) to experience different pressures. When subjected to 222.4 N of compaction force, the highest local pressure (case A) is 0.88 MPa and is 52% higher than the minimum local pressure

which is 0.58 MPa occurring in case B. In addition to Figure 6.13, contours of the compaction pressures at the interface (i.e. over the contact area) are presented in Figure 6.14 that can be used to interpret the pressure distributions.

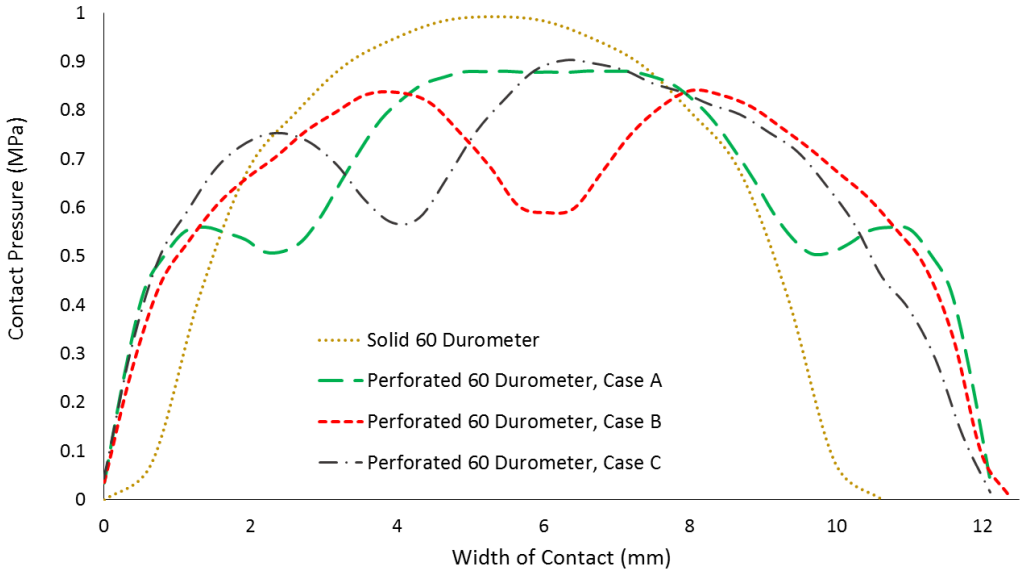

Figure 6.13 Comparison between the pressure distribution along the contact width in the solid rollers and the perforated roller.

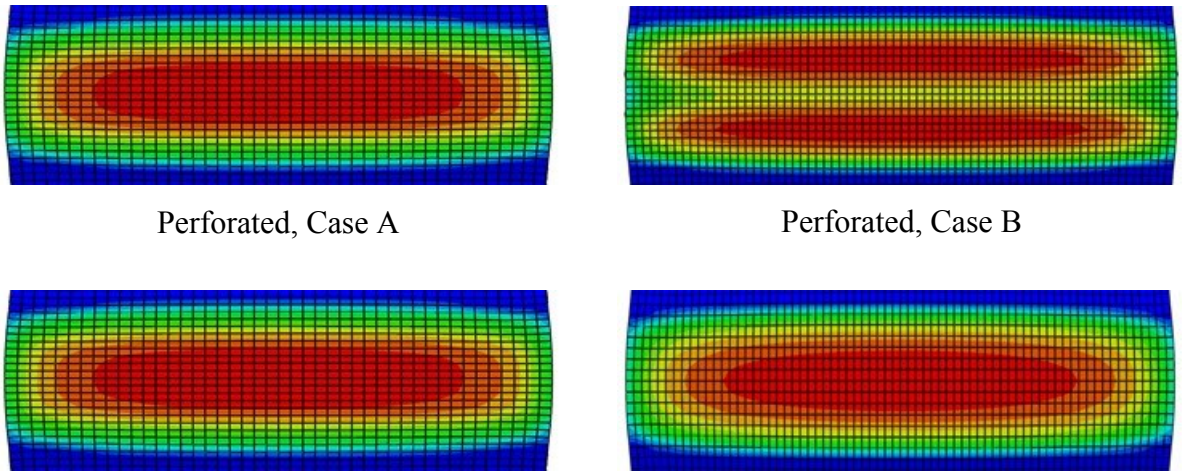

Perforated, Case A

Perforated, Case B

Perforated, Case C

Solid Roller.

Figure 6.14 Pressure contours at the interfaces: comparison between the solid and perforated cases of the 60 durometer polyurethane roller.

6.2 AFP TRIALS

Total of 80 trials with various different process conditions, steering radii and rollers were performed to investigate the effect of different compaction rollers. The series of AFP trials of chapter 3, were conducted with smaller steering radii which could amplify some of the defects. The main focus, here, is on larger steering radii to reduce the contributions of stresses induced in tows and highlight the influence of compaction roller. Moreover, more than one tow was laid down in each course to be able to identify potential patterns in the formation of blisters along the length of tows.

Process conditions that could help in identifying and demonstrating significant patterns are presented in Tables 6.3 and 6.4. In the first case, prepreg tows are laid down using the *standard perforated* 60 durometer compaction roller. While keeping the process conditions constant, steering radius was varied from 45 to 80 in with 5 in increments to observe the improvement of defects as the steering radius increased (or the curvature decreased). Figure 6.15 (a, b and c) are sample images from the resulting layups, for tows steered at 45, 55 and 70 in (or 114, 140 and 178 cm), respectively. It is clear that the wrinkles are *improving* as the steering radius *increases*. This was indeed expected based on the discussions presented on the experimental observations of chapter 3 and modeling approaches, discussed in chapters 4 and 5. More importantly, however, is to note the pattern in the formation of blisters. Higher levels of stress induced in the tows with smaller steering radius (e.g. Figure 6.15 (a)) causes number of blisters and wrinkles to appear with a more non-uniform pattern, again highlighting the roles induced stress levels and interface strength play in the formation of defects.

Table 6.3 Summary of important process conditions.

Case #	Steering Radius (cm)	Head Speed (mm/s)	Compaction Force (N)	Temperature (°C)	Flow Rate (lit/s)	Roller Description
1	114:12.7:203[1] (45:5:80)[2]	100	222.4	200	85	60[3], Perforated
		150, 100	222.4	150		
2	Straight	50	222.4	150, 200	85	60, Perforated
		50	89.0, 133.4, 177.9	150		
3	203 (80)	100	89.0, 133.4, 222.4	200	85	60, Perforated

[1] Notation: first radius : incremental increase (or decrease) in each trial : last radius.

[2] Steering radii in inches are provided in parentheses.

[3] Numbers in the roller descriptions are the shore-A hardness (in Durometer) of polyurethane tubes.

Experimental investigations and local models of predicting wrinkle formation suggest a maximum of ~120 cm as the value of *critical* steering radius above which the wrinkles do not appear (see 2.3.2.2). With increasing the steering radius, the stress levels and subsequently their effect on the formation of blisters is reduced. By using larger steering radii (e.g. Figure 6.15 (b) and (c)) the influence of the mechanical stresses induced due to tow steering is eliminated. In these figures a clear pattern can be observed. In each course, blisters are appearing in different tows along the same line. Moreover, the line of appearance of blisters is approximately appeared every 9-10 mm.

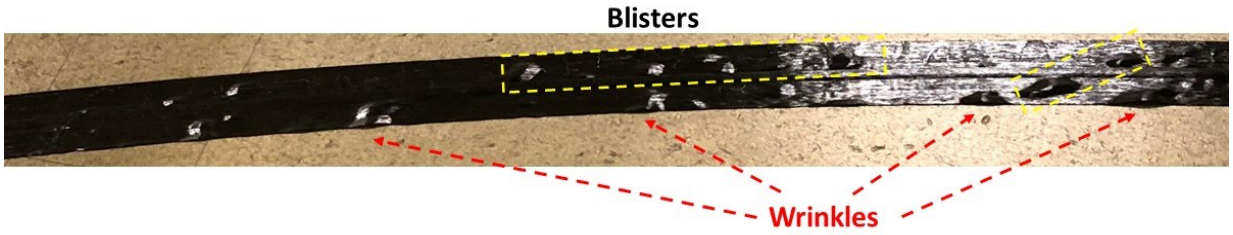

a. Two prepreg tows steered at 114.3 cm or 45 in.

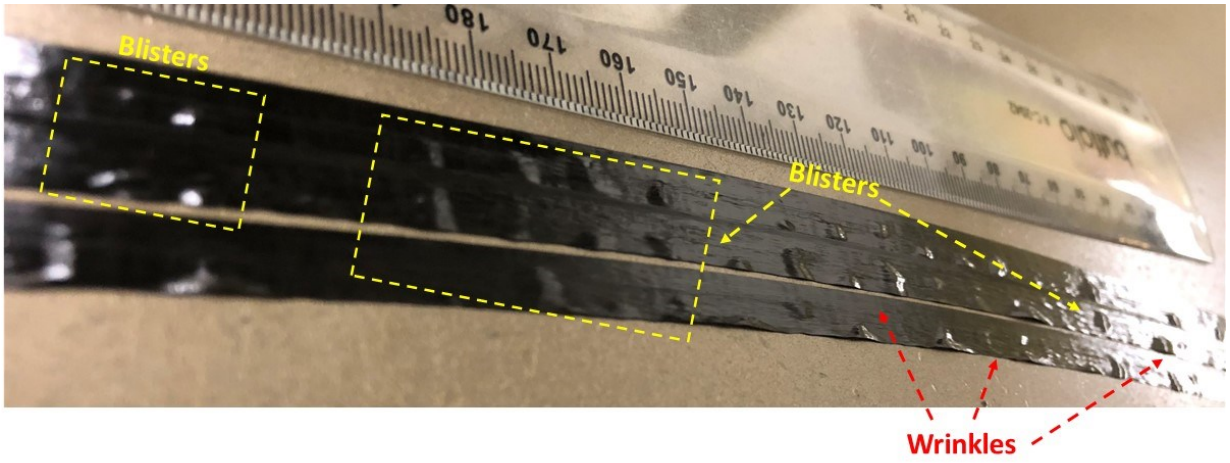

b. Three prepreg tows steered at 139.7 cm or 55 in.

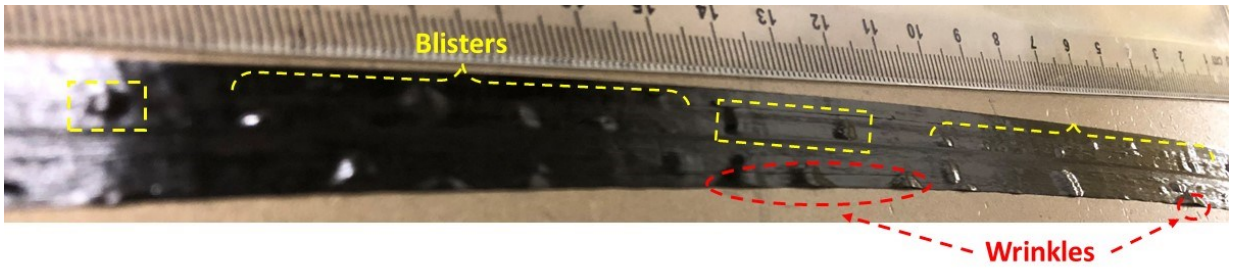

c. Two prepreg tows steered at 177.8 cm or 70 in.

Figure 6.15 Prepreg tows deposited with 60 durometer perforated roller; case 1.

Another interesting phenomenon is that some of the blisters (along a certain blister line) might transition into wrinkles. This can be seen in Figure 6.15 (c), especially in the first tow of the course (from the bottom) which has the smallest steering radius of the course. Some wrinkles have appeared that have taken the form of blisters in the second or third tow. Figure 6.16 from another

trial with different process conditions is also presented as an example demonstrating this phenomenon. The higher adhesion levels achieved as a result of locally elevated compaction pressure in the perforated roller (will be further discussed later) synchronizes with the buckling driven energy release mechanism resulting in the transformation of blisters to wrinkles in smaller steering radii.

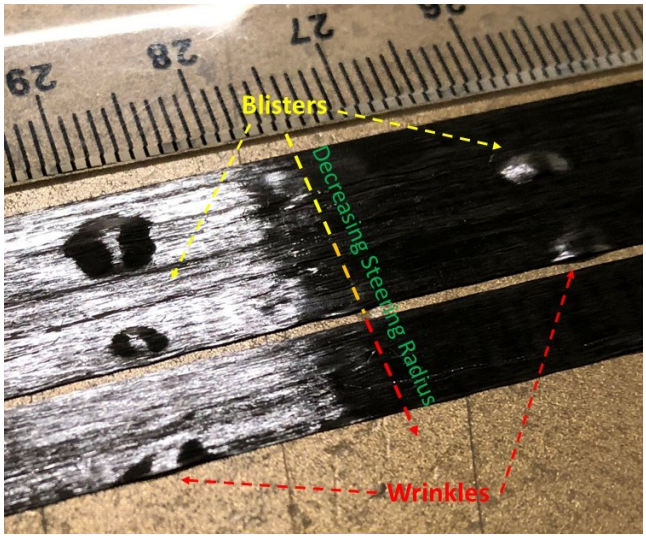

Figure 6.16 Possible transition from blisters to wrinkles at reference radius of 203 cm (80 in) and 222.4 N compaction force (case 3).

In the second case, prepreg tows are laid down on a straight path using the 60 durometer perforated roller and different process conditions (7 sample conditions tabulated in Table 6.3). The only stress available in a straight tow is the uniform longitudinal (on-axis) stress resulted from the fiber tension. Fiber tension is typically set to the minimum value that is found effective in keeping the prepreg tows straight, hence it results in a negligibly small amount of stress in the tow. Based on the mere consideration of internal stresses, it is *expected* that the prepreg tows which are deposited on a straight path and on a flat tool have an excellent quality.

In the first four sample process conditions tabulated in case 2, different layup speeds and temperature were used with the constant compaction force of 222.4 N. It was found that, as expected, the resulting layup has an excellent quality and the majority of different defect type have not appeared in the laid down tow. However, contrary to the predictions disregarding the roller

architecture, blisters have formed. Blisters have almost appeared on all four tows along lines that are approximately 9-10 mm apart (Figure 6.17), the length corresponding to the distance between the holes (place of local peaks in pressure distribution) in the loaded roller.

It was previously discussed in Prepreg Tack (2.2.3) and tack measurement (4.3.2.3) that sufficient compaction force is indispensable for attaining complete contact between the rough surfaces of prepreg and tool. The required levels of compaction are necessary for developing a strong interface and consequently, tack. It should be noted, however, that compaction force is a parameter that enhances the tack between prepreg and roller as well as the tack between prepreg and tool surface. The perforated architecture of roller causes local peaks and lows in the compaction pressure which is applied on the prepreg tows. When the applied compaction force is high enough, the local maximus of the pressure produces prepreg-roller tack which is of comparable strength to the tack between prepreg and tool. Consequently, as the roller moves forward, local high values of tack pulls the prepreg tows away from the tool surface, detaching the prepreg from the tool surface, and causing the uniform and orderly pattern of blisters to appear in the layups.

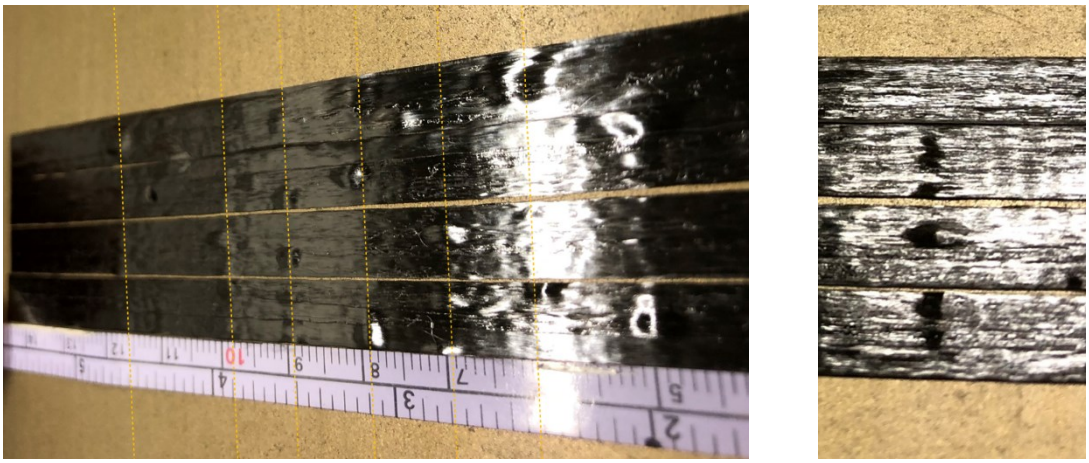

a. A course containing four tows. b. Magnification

Figure 6.17 Straight path with perforated roller (case 2; speed 100 mm/s, compaction force 222.4 N, temperature 150 °C).

In order to investigate this premise more thoroughly, the last three sample process conditions of case 2 are presented. A straight fiber path, evidently, do not require very strong tack levels to

remain on the tool surface. Consequently, the compaction force can be reduced from the 222.4 N which was previously found to be the optimum level. A sample image of the resulting layups is presented in Figure 6.18. When the compaction force is reduced (89.0 – 177.9 N), the pressure required to obtain higher levels of tack between the roller and prepreg is not attained. As a result of lower tack between roller and prepreg the prepreg is not pulled away strongly, and has remained intact, even though the prepreg-tool tack itself is weaker.

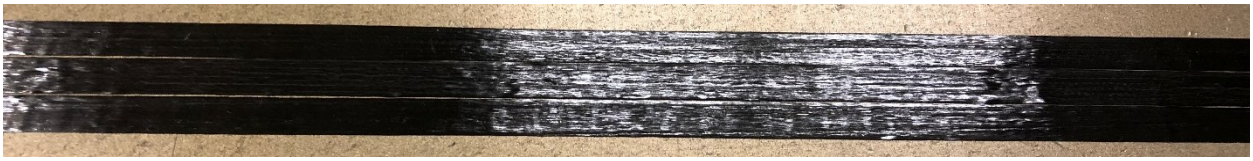

Figure 6.18 Straight path (case 2; speed 50 mm/s, force 133.4 N, temperature 150 °C).

When the prepreg tows are steered rather than being laid down on a straight reference path, in-plane stresses are induced in the tow. The internal stresses contribute to the formation of blisters even though the primary factor initiating them is the local spike of tack that occurs as a result of the roller architecture. In case 3, a slight curvature is introduced to the reference path by steering the course with 80 in or 203 cm radius. The compaction force is reduced from 222.4 N to 133.4 and 89.0 N. This will allow the weakening of the interface to be exhibited by the formation of *wrinkles* at the inside edge of the tows.

With the 222.4 N of compaction force, many blisters are formed (Figure 6.19 (a)). A comparison of this picture with the picture of straight tows (Figure 6.17) shows that in case of the steered tow, the formation of *blisters* are more pronounced. In addition, a few wrinkles are formed only on the first prepreg tow with the smallest steering radius of the course. Reducing the compaction force to 133.4 and 89.0 N (the minimum achievable with the current machine) results in the elimination of blisters from the layups (Figure 6.19 (b) and (c)). As expected, by reducing compaction force both tacks (prepreg-tool and prepreg-roller) are enfeebled. Consequently, the local maximus of the prepreg-roller tack is not strong enough to locally detach the prepreg and produce the blisters. Moreover, the weakened prepreg-tool interface causes more wrinkles to appear in these steered courses.

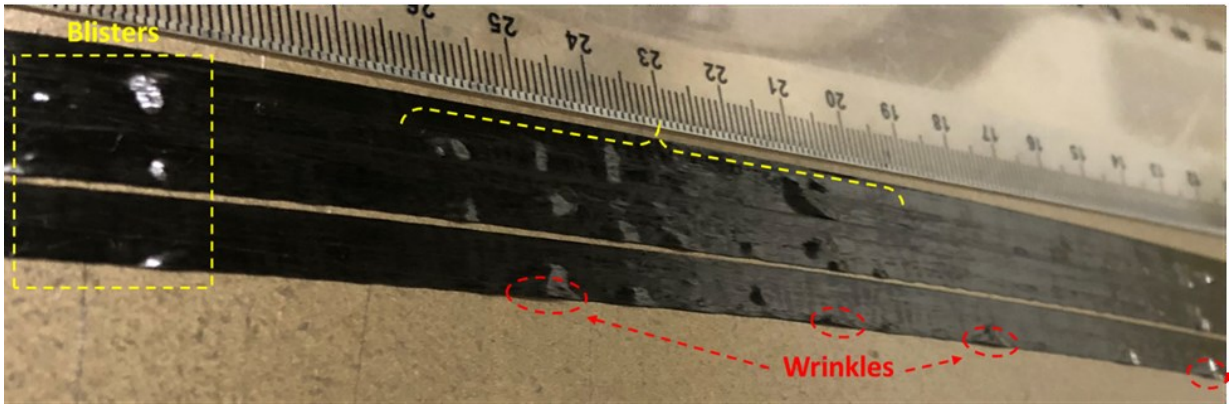

a. Compaction force 222.4 N (50 lbf).

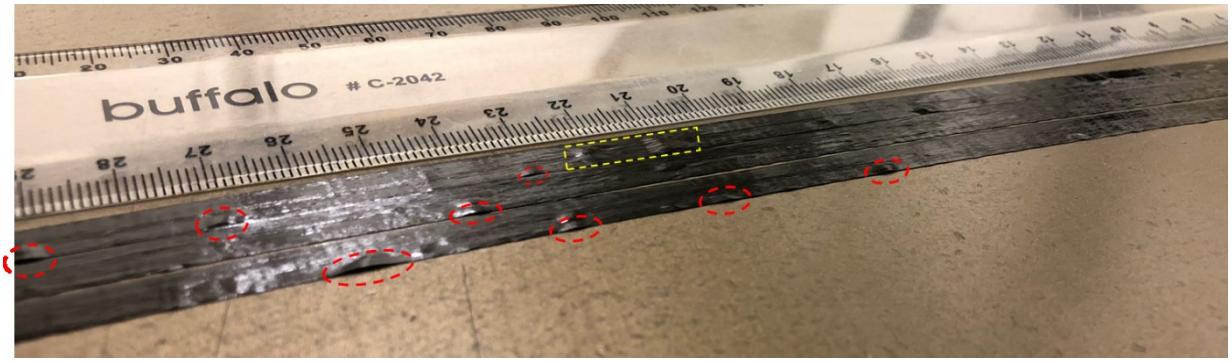

b. Compaction force 133.4 N (30 lbf).

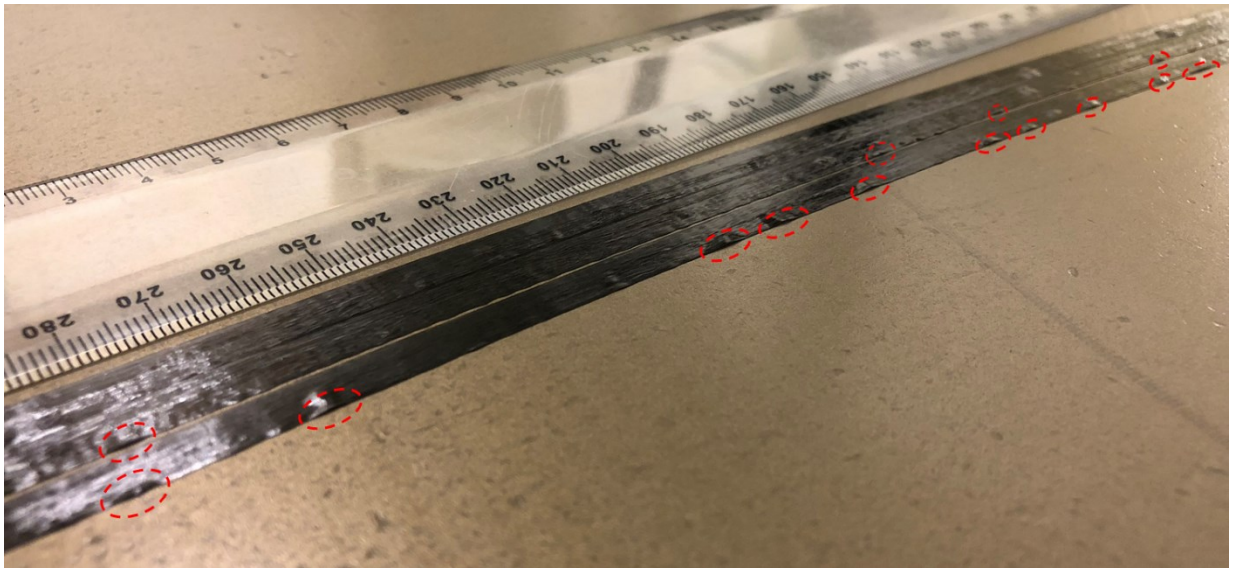

c. Compaction force 89.0 N (20 lbf).

Figure 6.19 Each course contain three prepreg tows steered at 203 cm, laid down with 60 durometer perforated roller (case 3).

The present section of the study highlighted the influence of the architecture of the compaction roller on the formation of defects. It is demonstrated that the prepreg-roller tack should be taken into consideration in addition to the prepreg-tool tack in order to achieve the highest layup quality. It was shown that maximizing prepreg tack by increasing compaction force can be detrimental to the layup quality when material is laid down using perforated rollers. With this type of rollers, lower compaction forces should be utilized *when possible*. However, this is not a robust solution since strong tack is required between the tool surface and prepreg for the prepreg to remain on the tool. Alternative strategies will be investigated to find solutions that are more suitable for laying down prepreg tows at smaller steering radii.

Deformation of the compaction roller is governed by three parameters, namely, compaction force, stiffness of the roller material and the architecture of the roller (perforated/solid). Compaction force that is applied to the roller is transmitted to the resin, causing its deformation. Consequently, an upper bound exists on the compaction force above which the redistribution of resin content becomes dominant, facilitating tow pull up to occur in the steered tows. In chapter 3, the best value of compaction force that could maximize tack was found to be in the vicinity of this upper bound. The issues arising as a result of using a perforated roller were discussed in this section. In the following, rollers with different hardness grades are used in the process to investigate how effective inherent material stiffness is, in comparison to the other two parameter. Rollers with decreasing levels of stiffness are presented in cases 7 to 11, tabulated in Table 6.4.

Table 6.4 Summary of important process conditions, continued from Table 6.3.

Case #	Steering Radius (cm/in)	Head Speed (mm/s)	Compaction Force (N)	Temperature (°C)	Flow Rate (lit/s)	Roller Description
4	Straight	100	222.4	150	85	Stainless Steel
5	Straight	150:10:100[1]	222.4	150	85	Stainless Steel with Tooltek
6	101.6 (40)[2]	50	222.4	200, 250	85	Stainless Steel with Tooltek
7	Straight	50	222.4	100	75	85[3], Solid
8	Straight	150, 100	89.0, 222.4	100	85	60, Solid
9	203, 152, 127 (80, 60, 50)	100	89.0, 222.4	200	85	60, Solid
10	203, 152.4, 101 (80, 60, 40)	100	177.9	200	85	35, Solid
11	203, 152.4 (80, 60)	150	177.9	220	85	35, Solid

[1] Notation: first radius : incremental increase (or decrease) in each trial : last radius.

[2] Steering radii in inches are provided in parentheses.

[3] Numbers in the roller descriptions are the shore-A hardness (in Durometer) of polyurethane tubes.

The second roller investigated in this study is the fully stainless steel roller that is sometimes used in the industry. Prepreg tows were laid down on straight paths with the gas temperature of 100 and 150 °C, compaction force of 222.4 N (50 lbf) and three different speed levels of 50, 100 and 150 mm/s. Prepregs were not able to adhere to the tool surface at the head speed of 150 mm/s, regardless of layup temperature. At 50 and 100 mm/s (case 4), where the prepreg was able to adhere to the tool, the smooth texture of the metal roller and very high pressure produced by the

roller helps in having a very good quality with no visible defects (Figure 6.20). Overall, however, this level of sensitivity to speed is not promising, considering the fact that the prepreg tows were not steered.

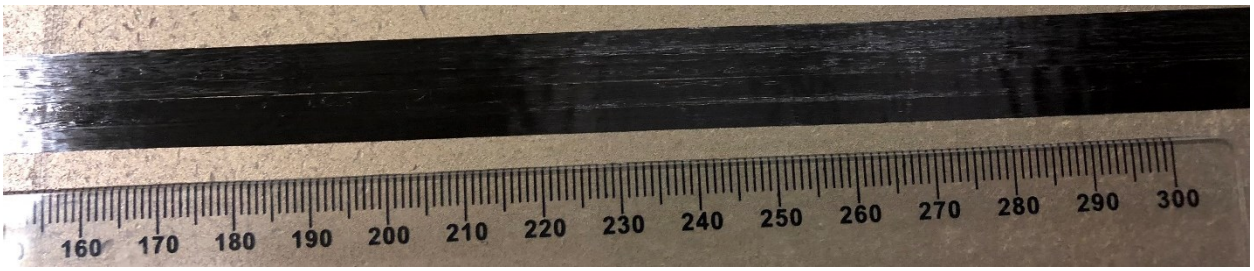

Figure 6.20 A straight course containing four tows laid down with stainless steel roller (case 4).

The primary reason for the high sensitivity of the tow quality to speed when using the stainless steel is the short dwell time created by the roller. Recalling from chapter 4, the contact time during which each segment of prepreg tow experiences the compaction force is on average $t_{ave} = \theta/V$ where θ is the contact width and V is the AFP head speed. The contact width is greatly determined by the inverse of rollers elastic modulus (equation (4.54)). Consequently, very high stiffness of the stainless steel causes the dwell time to decrease significantly which prohibits the tack from developing. Another possibility is that the prepreg-roller tack could be inherently higher for a stainless steel roller compare to the polyurethane ones, as a result of difference in surface energies. In order to control for this factor, a layer of tooltek tape is applied on the surface of the roller to minimize the prepreg-roller tack. Tooltek is essentially a fiberglass tape with Teflon PTFE plastic as the facing's coating and it is often used to provide a smooth and low-friction release at the roller surface.

In case 5, prepreg tows are deposited with the stainless steel roller and tooltek at constant parameters of 150 °C and 222.4 N while the head speed was reduced from 150 mm/s to 100 mm/s with 10 mm/s intervals. The maximum material deposition speed that resulted in the prepreg tow to adhere to the tool surface was found to be 110 mm/s. Above this speed, prepreg tows would not adhere to the tool, meaning that the very small contact area and resulting dwell time is primarily

responsible for this. At and below the 110 mm/s the resulting layups were very high quality, similar to Figure 6.20.

As the 6th case, prepreg tows were steered at moderate radius of 40 in or 101.6 cm using the stainless steel covered with tooltek. It was found that even at a relatively high process temperature and low speed, the roller is incapable of providing the tack necessary for a quality comparable to the layups deposited with the standard roller (Figure 6.21). Similar to the cases of chapter 3, high temperature combined with low velocity forms the *sheared fiber* type of defect. Contrary to the previous case, however, one cannot solve this issue by increasing the velocity or reducing the temperature, since the result would be lack of adherence of the tows to the tool surface This is again due to the fact that stainless steel roller is incapable of producing significant deformations and hence dwell time for the prepreg tack to develop which causes all types of defects to appear in the steered tows disposed by this roller.

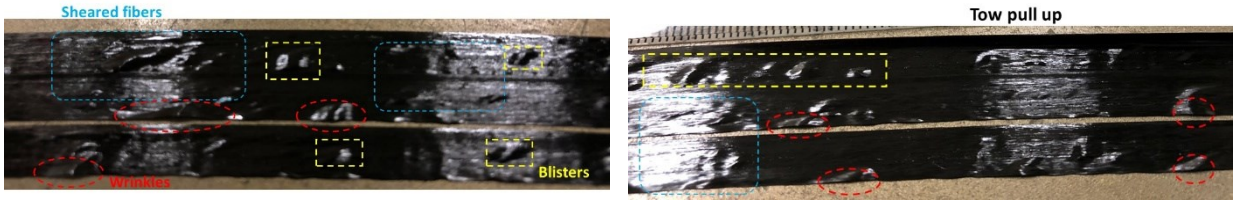

Figure 6.21 Samples from case 6: stainless steel roller with toolkit used to steer at 101.6 cm.

The 85 durometer roller is the stiffest polyurethane tube that was made and investigated for depositing prepreg tows on straight and steered paths. The contact width of this roller is more than 70% smaller than that of the standard 60 durometer perforated roller. Consequently, the primary issue with the stainless steel roller (short dwell time) persist in the 85 durometer roller to a significant extent. The performance of this roller, therefore, is limited. In case 7, for example, the speed of 50 mm/s is used to deposit the prepreg tows, which has resulted in a relatively good quality with slight blisters and waviness in the tow (Figure 6.22), but higher layup speeds and steering the tows would produce defective layups.

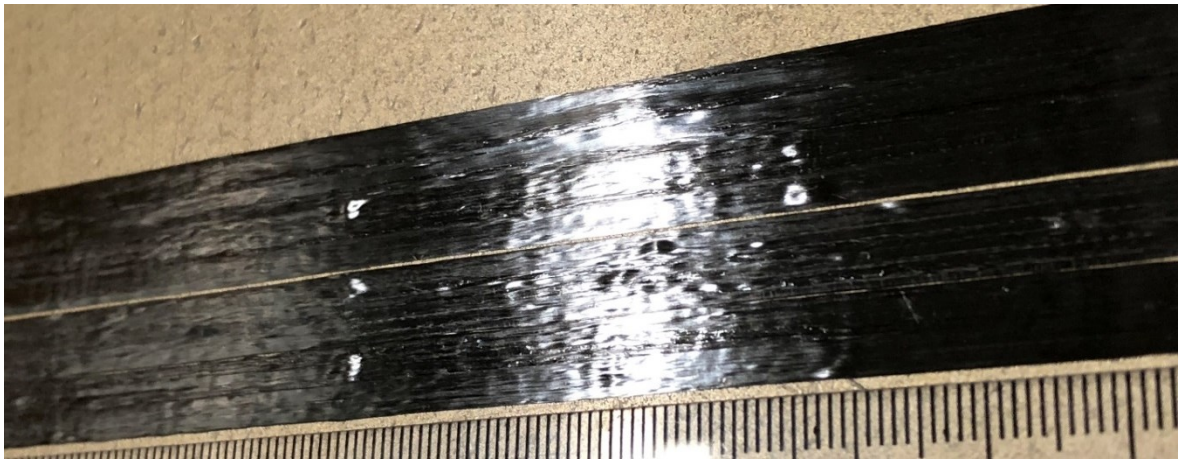

Figure 6.22 Straight fibers with solid 85 durometer roller (case 7).

The 60 durometer solid roller is made from the same grade of polyurethane as the standard perforated roller which is supplied by Automated Dynamics. The solid roller has rather a smaller contact area (~20%) due to lack of perforations in the polyurethane tube. However, because of the more steady pressure distribution it produces, it facilitates a better quality in the laid down tows. Sample process conditions used with the solid 60 durometer roller are presented in case 8 and 9. Material deposited on a straight fiber path has an excellent quality, with no visible defect regardless of the layup speed and compaction force, as presented in Figure 6.23.

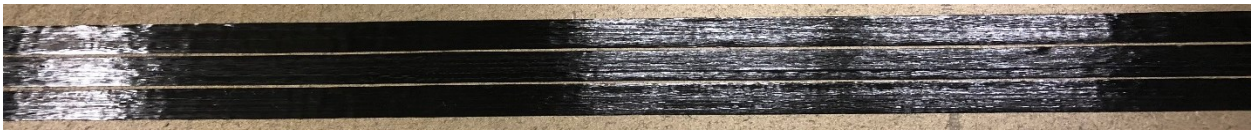

Figure 6.23 Straight fibers laid down with solid 60 durometer roller (case 8).

Moreover, material is laid down using process condition similar to the ones used with the perforated roller to enable a direct comparison between the two (Figure 6.24). A direct comparison at the relatively large steering radius of 203 cm, between Figure 6.19 (a) and Figure 6.24 (a), reveals the impact of perforated roller on the formation of blisters. The solid roller has resulted in a very good quality layup, which is mostly free of blisters. Smaller radius of 152.4 cm (Figure 6.24 (b)) with the solid roller can be compared with steering radii of 140 and 178 cm (Figure 6.15 (b)

and (c), respectively). The solid roller, again has smaller number of blisters even compared to the layup disposed with the perforated roller at a *larger* steering radius. With further decrease of steering radius, however, the stresses become more dominant and cause a change in the formation mechanism of blisters, from being driven by the prepreg-roller tack to being driven by the stresses induced as a result of tow steering. Consequently, more blisters are appeared in the smallest steering radius (127 cm), Figure 6.24 (c).

The last roller investigated in the present work is the most compliant of all, the solid 35 durometer roller. The static testing of the rollers under 222.4 N revealed that this roller reaches the same level of contact width as the perforated 60 durometer roller. As a result of large width of contact, a significant dwell time is provided for the prepreg tows during which a uniform and steady compaction pressure is applied. Therefore, it has the benefit of providing a large contact width, the perforated roller offers, without the drawback of imposing local pressure fluctuations on the prepreg tows.

Not surprisingly, similar to the moderately stiff 60 durometer solid roller, disposing prepreg tows with 35 durometer roller, on straight paths result in an excellent layup quality. The roller can easily deform against the tool surface, providing a smooth contact surface and consistent contact pressure for material deposition. In case 10, prepreg tows were laid down at 100 mm/s and three different steering radii of 203, 152.4 and 101.6 cm, results of which are presented in Figure 6.25. As can be seen in the sample pictures, perfect layup quality is attained for the 203 and 152.4 cm steering radii. The 101.6 cm steering radius that was laid down using the 35 durometer roller is the *smallest radius achieved in this chapter* that is relatively free of defects. Similar to the larger steering radii disposed with this roller, no blister has appeared in the prepreg tows. More interestingly, however, is the very small number of wrinkles in the 101.6 cm layup. The large dwell time provided by this roller and the *even* compaction pressure distribution, helps in establishing a very strong prepreg-tool tack. Result of this, is a layup quality that is significantly improved compared to the tows laid down using other rollers, *even though their steering radii were larger.*

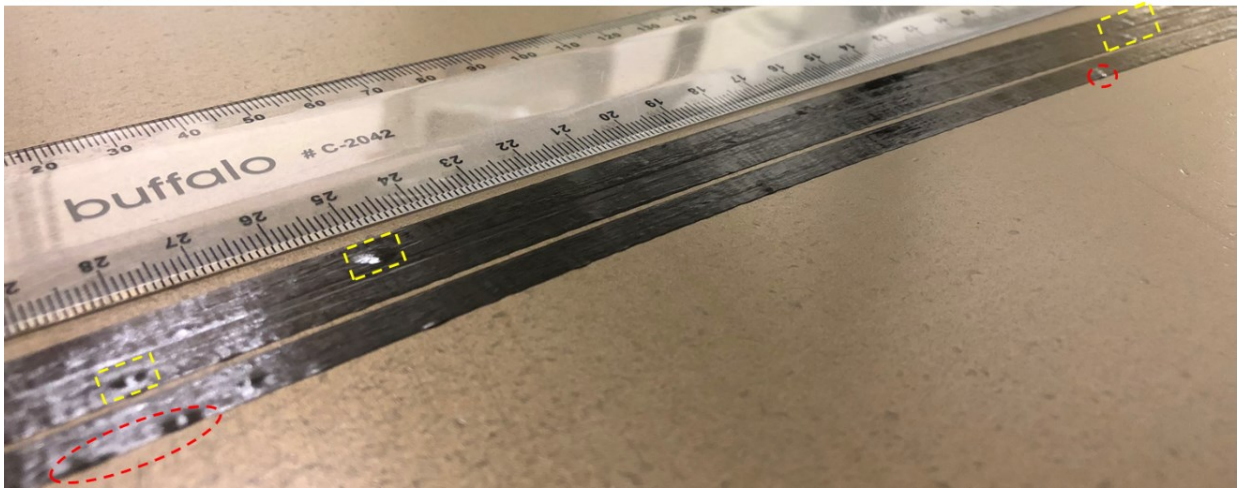

a. Steering radius = 203 cm.

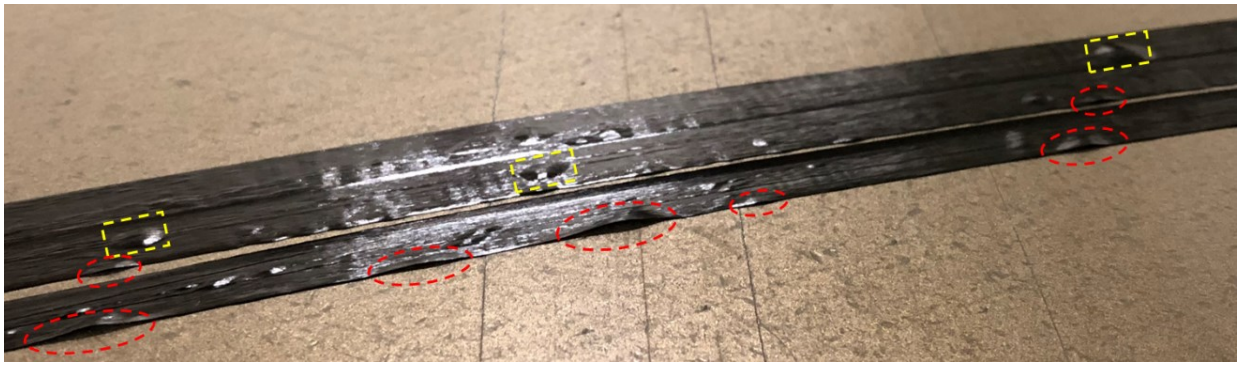

b. Steering radius = 152.4 cm.

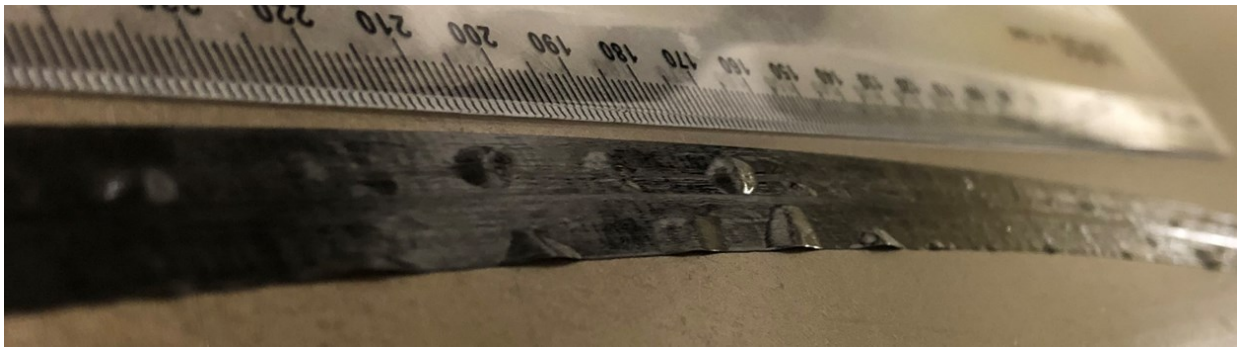

c. Steering radius = 127 cm.

Figure 6.24 Layups laid down with solid 60 durometer roller at different steering radii.

To demonstrate the application the 35 durometer roller in increasing the productivity of the process, case 11 with two different steering radii was performed in which the layup speed was

increased by 50%. Prepreg tows were laid down at 150 mm/s and with steering radii of 203 and 152 cm. Sample results are presented in Figure 6.26. In both trials, *only* a few wrinkles or blisters have appeared within the steered tows, which demonstrates that superior performance of the 35 durometer compliant roller. This roller is able to reach higher material deposition rates, with less compromising the quality of the layup.

a. Steering radius = 203 cm.

b. Steering radius = 152.4 cm.

c. Steering radius = 101 cm.

Figure 6.25 Layups laid down with 35 durometer roller with different steering radii and layup speed of 100 mm/s.

a. Steering radius = 203 cm.

b. Steering radius = 152.4 cm.

Figure 6.26 Layups laid down with 35 durometer roller with different steering radii and layup speed 150 mm/s.

6.3 CONCLUSIONS

The effect of compaction roller on the layup quality was investigated in this chapter. Specifically with regards to blisters it should be noted that different mechanisms contribute into their formation in the process. The stress distribution induced as a result of the tow steering produces weak spots in the prepreg-tool interface. Moreover, local peaks in the compaction pressure distribution caused by the perforated roller can produce locally elevated levels of prepreg-roller tack. Consequently, the roller is able to pull the prepreg away from the tool surface, detaching the prepreg tow from the tool and forming blisters.

Other inclusions and layup defects can also cause blisters. As an example, some level of gaps always exist between prepreg tows and different course. When a prepreg tow is laid down on top of gaps, the lack of material in the preceding layer prevents the current prepreg tow to have any support in that specific spot, therefore causing the formation of blisters. During the process, these different mechanisms can happen independently, or simultaneously and produce a synergic effect in the formation of blisters. These blisters can themselves be turned into out-of-plane buckling and manifest in the form of wrinkles in tows steered with smaller radii. Knowing all the different mechanisms contributing to the formation of blisters, and defects in general, can help in setting preventive strategies in place, in order to achieve the best layup quality possible.

The local pressure fluctuations that occur in perforated rollers were found to be detrimental to the layup quality. Using solid rollers that can produce the same level of contact width under similar compaction forces was found to be superior to the perforated roller in terms of the achievable layup quality. This can be further utilized to obtain higher process productivity. The contact width of the roller, in general, is very important in achieving a high quality layup. More compliant materials can provide a smoother and more even pressure distribution over the prepreg tows. Moreover, they have larger deformations, which helps in establishing higher tack levels by increasing the dwell time in the process.

7 CONCLUSIONS, CONTRIBUTIONS AND FUTURE WORK

7.1 NAVIGATING THE SPACE OF POSSIBLE PROCESS CONDITIONS

The key mechanism which resists against the formation of most layup defects is prepreg tack [29, 31, 33, 35, 38, 39]. Tack is a complex systemic property of prepreg-tool interface that can be reasonably controlled by process parameters. Experimental trials performed during this study as well as a review of the literature demonstrated that tack levels as a function of process parameters can be generally understood considering the formation of a strong Intimate Contact (IC), stress relaxation effects taking place inside the prepreg resin and the resin's cohesive strength.

Perhaps layup temperature is the most sensitive process parameter that affects the prepreg tack and layup quality. By increasing the temperature, the resin viscosity decreases and a better IC is achieved, resulting in higher tack. Experimental observations, however, have reported a peak in the tack of prepregs and pressure sensitive adhesives as a function of temperature. This is due to the fact that reduction of resin viscosity (with increasing temperatures) is accompanied by the decline of resin strength. Consequently, at very high temperatures, a good contact is formed, whereas the lower strength of the resin results in cohesive failure within the prepreg (as opposed to interfacial failure at the prepreg-tool interface for lower temperatures) [29, 38, 39]. It is worthwhile to mention that the cohesive failure for prepreg materials is characterized by an observable amount of residual resin on the tool.

Layup speed in the AFP is inversely proportional to the contact time. As such, the lower speed means more time for IC formation, lower strain rates and more time for relaxation of stresses in the prepreg resin, all of which result in higher tack levels. Increasing compaction force, again, helps to establish a good IC and increases the prepreg tack. A peak is also observed for the tack as a function of compaction force since further increase of the force will result in redistribution of the resin content and a contraction after the loading is released. Both these effects facilitate detachment of the prepreg from the tool surface (i.e. lower tack) [29]. Tack also has a peak around moderate values of relative humidity (50–60%), which is generally attributed to the changes in resin viscosity and strength [35].

Another important factor is the age of prepreg [33]. As the material ages, the crosslinking reaction occurs in the resin and the degree of cure increases. This will result in a stiffer material with higher storage modulus, G', and lower loss modulus, G'', which makes the development of IC and wetting of the tool surface harder. With the reduction in the degree of IC, the achievable tack levels decrease. Using fresh prepregs within their shelf life helps in having a better quality layup. Other parameters such as tool's surface roughness, and, resin and tool surface energies also play a role in both establishing the IC and the amount of work of adhesion, however, their macroscopic effects on prepreg tack is not very well understood at the moment and further investigation is required.

7.2 CONCLUDING REMARKS

The present thesis focuses on the defects appearing during tow steering in automated fiber placement of thermosetting prepreg tows. Experimental and modeling aspects of defect formation were considered.

In the first step, an extensive experimental AFP study is performed using various different process parameters and steering radii to investigate the defect formation process in the steered prepreg tows. Five major types of defects namely in-plane fiber waviness, sheared fibers, tow pull ups, blisters and out-of-plane wrinkles were identified in the steered tows. Seven sample cases elucidating some patterns and conditions that lead to the formation of each of these defects are presented and possible strategies that could lead to alleviating the defects were proposed. The viscoelastic properties of the resin causes prepreg tows and defects to exhibit time dependent behavior. A suitable process condition in which the time-dependent growth of wrinkles was more pronounced, is identifies. A camera was used to monitor the growth of wrinkles with time to demonstrate the viscoelastic nature of defect formation.

From the modeling perspective, two novel models were developed. First, the existing approach called *local modeling approach* is generalized to take the time-dependency of prepreg-tool tack into account. In this approach, the wrinkle formation process is considered to be an energy release process driven by the out-of-plane buckling of the prepreg tow. Because of the gradual deposition of prepreg tow in the AFP, the formation of each wrinkles is considered to be isolated from the other ones. Consequently, the wrinkle formation can be treated as the buckling of a representative

plate. A generalized viscoelastic Pasternak foundation is introduced between the tool and prepreg to incorporate the viscoelastic effects into the model.

Furthermore, a new global defect modeling framework through modeling the whole prepreg deposition process of Automated Fiber Placement is presented. A simple mechanism is created to simulate the prepreg feeding mechanism of the prepreg tow. The surface-based cohesive zone modeling technique using a bilinear traction-separation law is used to model the prepreg tack. The application of the modeling framework in capturing the out-of-plane wrinkles and blisters is demonstrated.

The experimental procedures required to obtain model parameters are presented. Specifically, the application of probe tack test for determining the unknown parameters of the bilinear traction-separation law is discussed. A simple contact theory approach is presented to relate the dwell time of the probe tack test to the AFP head speed and compaction force. The theoretical model and finite element simulations are compared against their corresponding experimental AFP trials and it was demonstrated that good agreement is achieved in both cases.

Finally, an in-depth investigation on the influence of the compaction roller on the layup quality is conducted. The deformation of the rollers and the compaction pressure profile they produce when subjected to the process-levels of compaction force are obtained through static testing and simulation. It was demonstrated how through controlling the dwell time and compaction pressure the roller affects the layup quality. The 35 durometer polyurethane rollers were found to be most effective in laying down thermosetting prepreg tows with high quality, and was shown they can potentially be implemented to increase the process productivity.

7.3 CONTRIBUTIONS

Some of the major contributions presented in this thesis are summarized below:

- Identification of the process-induced defects in fiber placement and during fiber steering. Different types of defects were detected and documented.

- A novel time-dependent buckling model for an orthotropic plate which is resting on a generalized viscoelastic Pasternak foundation and is subjected to in-plane axial loading is developed.
- The local modeling approach of predicting wrinkles is extended to consider the time-dependent growth of wrinkles. The application of the developed time-dependent buckling model in this context is presented.
- A new global modeling framework in the commercial finite element software Abaqus is developed which is capable of capturing wrinkles and identifying the contribution of steering-induced stresses to the formation of blisters.
- The influence of compaction roller on the quality of layups was investigated. The effect of different grades of materials and roller architecture on the compaction pressure distribution and width of contact the roller produces, as well as how they will consequently influence the prepreg layups' quality were studied.

In addition to the above reported contributions, the following publications have been accomplished during the study:

Journals:

1. **Nima Bakhshi** and Mehdi Hojjati, "An experimental and Simulative Study on the Defects Appeared during Tow Steering in Automated Fiber Placement", *Composite Part A: Applied Science and Manufacturing*, Vol. 113, pp. 122-131 (2018).
2. **Nima Bakhshi** and Mehdi Hojjati, "Time-dependent wrinkle formation during tow steering in automated fiber placement", submitted to the *Composite Part B: Engineering*.
3. **Nima Bakhshi** and Mehdi Hojjati, "Effect of Compaction Roller on Layup Quality and Defects Formation in Automated Fiber Placement", submitted to the *Composite Part A: Applied Science and Manufacturing*.

Conferences:

1. **Nima Bakhshi**, Muhsen Belhaj, and Mehdi Hojjati," Viscoelastic Effects on Wrinkle Formation during Tow Steering in Automated Fiber Placement" 18th European Conference on Composite Materials ECCM 18, Athens, Greece, June 24-28 (2018).

2. Muhsen Belhaj, **Nima Bakhshi**, and Mehdi Hojjati," Foundation Parameters Characterization for Prediction of Critical Steering Radius in Automated Fiber Placement" 18th European Conference on Composite Materials ECCM 18, Athens, Greece, June 24-28 (2018).
3. **Nima Bakhshi** and Mehdi Hojjati," Simulating Layup Defects During Tow Steering In Automated Fiber Placement" Proceedings of The Canadian Society for Mechanical Engineering International Congress 2018, Toronto, Ontario, Canada May 27-30, (2018).

7.4 FUTURE RESEARCH

A vast opportunity for research exists in the automated manufacturing of thermosetting and thermoplastic composite materials. Broad aspects of areas that require more investigations were presented in [6]. Specifically, in the context of steering thermosetting prepreg tows in the automated fiber placement process, the following recommendations for further research in experimental and modeling aspects of the problem can be offered.

The global modeling framework presented here can be further generalized to consider more accurate material properties. Accounting for the through thickness behavior of prepreg materials (e.g. [79]) and resin redistribution can enable the model to capture tow pull ups (i.e. bridging) at the outside edge of the steered tows. Furthermore, implementing time-temperature superposition, along with a viscoelastic orthotropic material representation for the prepreg can help in reducing the number of tests required for characterizing the prepreg behavior by incorporating the rate and temperature dependencies into the model.

Moreover, the prepreg-tool tack is essentially a viscoelastic property. Developing a viscoelastic cohesive zone using contact Abaqus subroutines can allow for a more detailed, time-dependent representation of tack, and consequently time-dependent growth of defects. Using the same method, the prepreg-roller tack can also be taken into account as a function of local fluctuations in the compaction pressure that may be produced by the roller. This could potentially allow the user to capture blisters more accurately.

Fresh prepreg materials do not entirely lose their tackiness after being detached from the tool surface. Applying a temporary pressure on defects, sometimes, can help in keeping the tow on the

tool surface. Consequently, effect of laying down subsequent layers of prepreg tows on defective layups, and the interaction between the compaction roller and existing defects should be further studied.

Layup defects have been identified and possible strategies for mitigating them have been proposed. Ultimately, however, further optimization of the manufacturing process would require knowledge of the extent to which these defects can affect mechanical properties of the final cured parts. Considering that some of the defects are very hard to be completely avoided, degrees of tolerance should be defined. Optimum windows of process conditions might be established acknowledging that some degree of defects appear within layups, that are deemed acceptable. Moreover, the effect of curing technique, for instance using caul plates, autoclave, etc., how the defects develop throughout the curing process and how these factors influence final properties of parts made up of defective layups should be studied.

Last but not least, more accurate characterization of normal and especially tangential (which is under investigated) behavior of the prepreg tack, i.e. I, II and III modes of failure of tack, is still required. Moreover, how the *characterization conditions* in the peel test and probe test can be *mapped into* the AFP *process conditions* need to be further investigated experimentally. Robust methods for quantitatively measuring prepreg tack, to produce mechanical properties data that can meaningfully describe tack (e.g. parameters of advanced cohesive zone models) is of utmost importance for gaining any deeper insights into the AFP process as well as the defect formation processes.

8 REFERENCES

[1] S. V. Hoa, *Principles of the manufacturing of composite materials*. DEStech Publications, Inc, 2009.

[2] J. Sloan, "ATL & AFP: Defining the megatrends in composite aerostructures," *High performance composites,* vol. 16, no. 4, p. 68, 2008.

[3] *Composites World Magazine*. Available: www.compositesworld.com

[4] B. Denkena, C. Schmidt, and P. Weber, "Automated Fiber Placement Head for Manufacturing of Innovative Aerospace Stiffening Structures," *Procedia Manufacturing,* vol. 6, pp. 96-104, 2016.

[5] Y. Khaled and H. Mehdi, "Processing of thermoplastic matrix composites through automated fiber placement and tape laying methods: A review," *Journal of Thermoplastic Composite Materials,* p. 0892705717738305, 2017.

[6] H.-J. L. Dirk, C. Ward, and K. D. Potter, "The engineering aspects of automated prepreg layup: History, present and future," *Composites Part B: Engineering,* vol. 43, no. 3, pp. 997-1009, 2012.

[7] J. Frketic, T. Dickens, and S. Ramakrishnan, "Automated manufacturing and processing of fiber-reinforced polymer (FRP) composites: An additive review of contemporary and modern techniques for advanced materials manufacturing," *Additive Manufacturing,* vol. 14, pp. 69-86, 2017.

[8] C. González, J. J. Vilatela, J. M. Molina-Aldareguía, C. S. Lopes, and J. Llorca, "Structural composites for multifunctional applications: Current challenges and future trends," *Progress in Materials Science,* vol. 89, no. Supplement C, pp. 194-251, 2017/08/01/ 2017.

[9] R. J. Crossley, "Characterisation of tack for automated tape laying," PhD thesis, University of Nottingham, 2011.

[10] K. Kendall, "Adhesion: molecules and mechanics," *Science,* vol. 263, no. 5154, pp. 1720-1725, 1994.

[11] A. Tiwari *et al.*, "The effect of surface roughness and viscoelasticity on rubber adhesion," *Soft Matter,* 10.1039/C7SM00177K vol. 13, no. 19, pp. 3602-3621, 2017.

[12] B. Persson, O. Albohr, U. Tartaglino, A. Volokitin, and E. Tosatti, "On the nature of surface roughness with application to contact mechanics, sealing, rubber friction and adhesion," *Journal of Physics: Condensed Matter,* vol. 17, no. 1, p. R1, 2004.

[13] K. L. Johnson, K. Kendall, and A. Roberts, "Surface energy and the contact of elastic solids," *Proc. R. Soc. Lond. A,* vol. 324, no. 1558, pp. 301-313, 1971.

[14] B. Derjaguin, V. Muller, and Y. P. Toporov, "Effect of contact deformations on the adhesion of particles," *Progress in Surface Science,* vol. 45, no. 1-4, pp. 131-143, 1994.

[15] D. Maugis, "Adhesion of spheres: the JKR-DMT transition using a Dugdale model," *Journal of colloid and interface science,* vol. 150, no. 1, pp. 243-269, 1992.

[16] R. S. Bradley, "LXXIX. The cohesive force between solid surfaces and the surface energy of solids," *The London, Edinburgh, and Dublin Philosophical Magazine and Journal of Science,* vol. 13, no. 86, pp. 853-862, 1932.

[17] W. Banks and C. Mill, "Tacky adhesion—a preliminary study," *Journal of Colloid Science,* vol. 8, no. 1, pp. 137-147, 1953.

[18] D. Satas, *Handbook of pressure sensitive adhesive technology*. Van Nostrand Reinhold New York, 1989.

[19] K. Ahn, J. Seferis, T. Pelton, and M. Wilhelm, "Analysis and characterization of prepreg tack," *Polymer Composites,* vol. 13, no. 3, pp. 197-206, 1992.

[20] B. Duncan, S. Abbot, and R. Roberts, "Measurement Good Practice Guide No. 26: Adhesive tack," Repot 1999.

[21] I. Mohammed, M. Charalambides, and A. Kinloch, "Modelling the interfacial peeling of pressure-sensitive adhesives," *Journal of Non-Newtonian Fluid Mechanics,* vol. 222, pp. 141-150, 2015.

[22] I. Mohammed, M. Charalambides, and A. Kinloch, "Modeling the effect of rate and geometry on peeling and tack of pressure-sensitive adhesives," *Journal of Non-Newtonian Fluid Mechanics,* vol. 233, pp. 85-94, 2016.

[23] C. Creton and M. Ciccotti, "Fracture and adhesion of soft materials: a review," *Reports on Progress in Physics,* vol. 79, no. 4, p. 046601, 2016.

[24] A. Kinloch, C. Lau, and J. Williams, "The peeling of flexible laminates," *International Journal of Fracture,* vol. 66, no. 1, pp. 45-70, 1994.

[25] Z. Peng, C. Wang, L. Chen, and S. Chen, "Peeling behavior of a viscoelastic thin-film on a rigid substrate," *International Journal of Solids and Structures,* vol. 51, no. 25-26, pp. 4596-4603, 2014.

[26] A. Kinloch, H. Koay, S. Lee, and L. Ng, "Using the simple peel test to measure the adhesive fracture energy, Ga," 2012.

[27] H. Lakrout, P. Sergot, and C. Creton, "Direct observation of cavitation and fibrillation in a probe tack experiment on model acrylic pressure-sensitive-adhesives," *The Journal of Adhesion,* vol. 69, no. 3-4, pp. 307-359, 1999.

[28] Y. Peykova, S. Guriyanova, O. V. Lebedeva, A. Diethert, P. Müller-Buschbaum, and N. Willenbacher, "The effect of surface roughness on adhesive properties of acrylate copolymers," *International Journal of Adhesion and Adhesives,* vol. 30, no. 4, pp. 245-254, 2010/06/01/ 2010.

[29] C. Creton, "Pressure-sensitive adhesives: an introductory course," *MRS bulletin,* vol. 28, no. 6, pp. 434-439, 2003.

[30] S. Sun, M. Li, and A. Liu, "A review on mechanical properties of pressure sensitive adhesives," *International Journal of Adhesion and Adhesives,* vol. 41, pp. 98-106, 2013/03/01/ 2013.

[31] O. Dubois, J.-B. Le Cam, and A. Beakou, "Experimental analysis of prepreg tack," *Experimental Mechanics,* vol. 50, no. 5, pp. 599-606, 2010.

[32] J. SEFERIS and J. MEISSONNIER, "Development of a tack and drape test for prepregs based on viscoelastic principles," *SAMPE quarterly,* vol. 20, pp. 55-64, 1989.

[33] K. J. Ahn, L. Peterson, J. C. Seferis, D. Nowacki, and H. G. Zachmann, "Prepreg aging in relation to tack," *Journal of Applied Polymer Science,* vol. 45, no. 3, pp. 399-406, 1992.

[34] A. Gillanders, S. Kerr, and T. Martin, "Determination of prepreg tack," *International Journal of Adhesion and Adhesives,* vol. 1, no. 3, pp. 125-134, 1981.

[35] C. Wohl *et al.*, "Tack Measurements of Prepreg Tape at Variable Temperature and Humidity," 2017.

[36] R. Banks, A. Mouritz, S. John, F. Coman, and R. Paton, "Development of a new structural prepreg: characterisation of handling, drape and tack properties," *Composite structures,* vol. 66, no. 1, pp. 169-174, 2004.

[37] S. Rao, R. Umer, J. Thomas, and W. J. Cantwell, "Investigation of peel resistance during the fibre placement process," *Journal of Reinforced Plastics and Composites,* vol. 35, no. 4, pp. 275-286, 2016.

[38] R. Crossley, P. Schubel, and N. Warrior, "The experimental determination of prepreg tack and dynamic stiffness," *Composites Part A: Applied Science and Manufacturing,* vol. 43, no. 3, pp. 423-434, 2012.

[39] R. J. Crossley, P. J. Schubel, and D. S. A. De Focatiis, "Time–temperature equivalence in the tack and dynamic stiffness of polymer prepreg and its application to automated composites manufacturing," *Composites Part A: Applied Science and Manufacturing,* vol. 52, pp. 126-133, 9// 2013.

[40] M. L. Williams, R. F. Landel, and J. D. Ferry, "The temperature dependence of relaxation mechanisms in amorphous polymers and other glass-forming liquids," *Journal of the American Chemical society,* vol. 77, no. 14, pp. 3701-3707, 1955.

[41] G. G. Lozano, A. Tiwari, C. Turner, and S. Astwood, "A review on design for manufacture of variable stiffness composite laminates," *Proceedings of the Institution of Mechanical Engineers, Part B: Journal of Engineering Manufacture,* vol. 230, no. 6, pp. 981-992, 2016.

[42] B. F. Tatting, "Analysis and design of variable stiffness composite cylinders," Virginia Tech, 1998.

[43] B. F. Tatting and Z. Gurdal, "Automated finite element analysis of elastically-tailored plates," 2003.

[44] Z. Gurdal, B. Tatting, and K. Wu, "Tow-placement technology and fabrication issues for laminated composite structures," in *46th AIAA/ASME/ASCE/AHS/ASC Structures, Structural Dynamics and Materials Conference*, 2005, p. 2017.

[45] O. Falcó, J. Mayugo, C. Lopes, N. Gascons, and J. Costa, "Variable-stiffness composite panels: Defect tolerance under in-plane tensile loading," *Composites Part A: Applied Science and Manufacturing,* vol. 63, pp. 21-31, 2014.

[46] X. Li, S. R. Hallett, and M. R. Wisnom, "Modelling the effect of gaps and overlaps in automated fibre placement (AFP)-manufactured laminates," *Science and Engineering of Composite Materials,* vol. 22, no. 2, pp. 115-129, 2015.

[47] O. Falcó, C. Lopes, F. Naya, F. Sket, P. Maimí, and J. Mayugo, "Modelling and simulation of tow-drop effects arising from the manufacturing of steered-fibre composites," *Composites Part A: Applied Science and Manufacturing,* vol. 93, pp. 59-71, 2017.

[48] W. Francis, M. Lake, and J. S. Mayes, "A review of classical fiber microbuckling analytical solutions for use with elastic memory composites," in *47th AIAA/ASME/ASCE/AHS/ASC Structures, Structural Dynamics, and Materials Conference 14th AIAA/ASME/AHS Adaptive Structures Conference 7th*, 2006, p. 1764.

[49] W. H. Francis IV, "Mechanics of post-microbuckled compliant-matrix composites," Citeseer, 2008.

[50] F. Lopez Jimenez, "Mechanics of thin carbon fiber composites with a silicone matrix," California Institute of Technology, 2011.

[51] P. Hörmann, *Thermoset Automated Fibre Placement-on Steering Effects and Their Prediction*. Verlag Dr. Hut, 2016.

[52] B. W. Rosen, "Fiber composite materials," *American Society for Metals, Metals Park, Ohio,* vol. 37, 1965.

[53] S. Nagendra, S. Kodiyalam, J. E. Davis, and V. Parthasarathy, "Optimization of tow fiber paths for composite design," in *Proceedings of the AIAA/ASME/ASCE/AHS/ASC 36th Structures, Structural Dynamics and Materials Conference, New Orleans, LA*, 1995, pp. 1031-41.

[54] J. Chen, T. Chen-Keat, M. Hojjati, A. Vallee, M.-A. Octeau, and A. Yousefpour, "Impact of layup rate on the quality of fiber steering/cut-restart in automated fiber placement processes," *Science and Engineering of Composite Materials,* vol. 22, no. 2, pp. 165-173, 2015.

[55] A. W. Blom, "Structural performance of fiber-placed, variable-stiffness composite conical and cylindrical shells," 2010.

[56] M. Wiehn and R. Hale, "Low cost robotic fabrication methods for tow placement," in *47 th International SAMPE Symposium and Exhibition 2002*, 2002, pp. 1842-1852.

[57] R. Smith, Z. Qureshi, R. Scaife, and H. El-Dessouky, "Limitations of processing carbon fibre reinforced plastic/polymer material using automated fibre placement technology," *Journal of Reinforced Plastics and Composites,* vol. 35, no. 21, pp. 1527-1542, 2016.

[58] C. Zhao, J. Xiao, W. Huang, X. Huang, and S. Gu, "Layup quality evaluation of fiber trajectory based on prepreg tow deformability for automated fiber placement," *Journal of Reinforced Plastics and Composites,* vol. 35, no. 21, pp. 1576-1585, 2016.

[59] A. Beakou, M. Cano, J. B. Le Cam, and V. Verney, "Modelling slit tape buckling during automated prepreg manufacturing: A local approach," *Composite Structures,* vol. 93, no. 10, pp. 2628-2635, 2011/09/01/ 2011.

[60] M. Y. Matveev, P. J. Schubel, A. C. Long, and I. A. Jones, "Understanding the buckling behaviour of steered tows in Automated Dry Fibre Placement (ADFP)," *Composites Part A: Applied Science and Manufacturing,* vol. 90, no. Supplement C, pp. 451-456, 2016/11/01/ 2016.

[61] M. Belhaj and M. Hojjati, "Wrinkle formation during steering in automated fiber placement: Modeling and experimental verification," *Journal of Reinforced Plastics and Composites,* p. 0731684417752872, 2018.

[62] B. C. Kim, K. Potter, and P. M. Weaver, "Continuous tow shearing for manufacturing variable angle tow composites," *Composites Part A: Applied Science and Manufacturing,* vol. 43, no. 8, pp. 1347-1356, 2012.

[63] Cytec Engineered Materials, "CYCOM 977-2, Product data sheet," 2012.

[64] N. Bakhshi and M. Hojjati, "An experimental and Simulative Study on the Defects Appeared during Tow Steering in Automated Fiber Placement," *Composites Part A: Applied Science and Manufacturing,* 2018.

[65] N. Bakhshi and M. Hojjati, "Time-dependent wrinkle formation during tow steering in automated fiber placement," *Submitted to Composites Part B: Engineering,* 2018.

[66] R. Christensen, *Theory of viscoelasticity: an introduction*. Elsevier, 2012.

[67] A. D. Kerr, "Elastic and Viscoelastic Foundation Models," *Journal of Applied Mechanics,* vol. 31, no. 3, pp. 491-498, 1964.

[68] R. A. Schapery, "A method of viscoelastic stress analysis using elastic solutions," *Journal of the Franklin Institute,* vol. 279, no. 4, pp. 268-289, 1965.

[69] D. W. Wilson and J. R. Vinson, "Viscoelastic analysis of laminated plate buckling," *AIAA journal,* vol. 22, no. 7, pp. 982-988, 1984.

[70] P. Weaver and J. Herencia, "Buckling of a flexurally anisotropic plate with one edge free," in *48th AIAA/ASME/ASCE/AHS/ASC Structures, Structural Dynamics, and Materials Conference*, 2007, p. 2413.

[71] R. A. Sauer, "A survey of computational models for adhesion," *The Journal of Adhesion,* vol. 92, no. 2, pp. 81-120, 2016.

[72] Wikipedia. Available: https://en.wikipedia.org/wiki/Fracture_mechanics

[73] ABAQUS, "ABAQUS 6.14 Documentation," *Dassault Systemes, Providence, RI, USA,* 2014.

[74] K. Potter, "Bias extension measurements on cross-plied unidirectional prepreg," *Composites Part A: Applied Science and Manufacturing,* vol. 33, no. 1, pp. 63-73, 2002.

[75] H. Alshahrani, R. Mohan, and M. Hojjati, "Experimental investigation of in-plane shear deformation of out-of-autoclave prepreg," *International Journal of Composite Materials,* vol. 5, no. 4, pp. 81-87, 2015.

[76] P. L. Mischler, M. C. Tingley, and K. Hoffmann, "Compaction roller for a fiber placement machine," ed: Google Patents, 2010.

[77] F. Hélénon, D. Ivanov, and K. Potter, "Modelling slit tape deposition during automated fibre placement," in *Proceedings of the 19th international conference on composite materials*, 2013.

[78] H. Qi, K. Joyce, and M. Boyce, "Durometer hardness and the stress-strain behavior of elastomeric materials," *Rubber chemistry and technology,* vol. 76, no. 2, pp. 419-435, 2003.

[79] D. H. A. Lukaszewicz and K. Potter, "Through-thickness compression response of uncured prepreg during manufacture by automated layup," *Proceedings of the Institution of*

Mechanical Engineers, Part B: Journal of Engineering Manufacture, vol. 226, no. 2, pp. 193-202, 2012.

[80] C. Stover, "Laplace-Carson Transform," *From MathWorld--A Wolfram Web Resource*.

APPENDIX A: TRANSFORMATIONS

Laplace-Carson transformation is a variation of Laplace transform which was especially devised by Carson to make the transform of Heaviside step function equal to 1 (in appose to $1/s$ in the Laplace space) [80]. It is defined by:

$$\tilde{F}(s) = s\int_0^\infty e^{-st} f(t)dt \tag{A.1}$$

The Laplace-Carson transformation is different from the Laplace transformation in the s which is multiplied to the integral, therefore, $\tilde{F} = s\bar{F}$. Where the tilde $\widetilde{(.)}$ denotes the Laplace-Carson transformation of the function while the bar $\overline{(.)}$ denotes the Laplace transformation of the function.

In the context of viscoelasticity, the integral approaches can be developed using two different, but equivalent, integrals, namely the Stieltjes integral and the Boltzmann integral. The Stieltjes integral can be more easily treated in the Laplace-Carson space:

$$F * dG(\tau) \equiv \int F(t-\vartheta)dG(\vartheta) \rightarrow \tilde{F}(s) \times \tilde{G}(s) \tag{A.2}$$

However, for the normal convolution (also known as constitutive Boltzmann integral equation in the viscoelasticity literature), the Laplace transform is more convenient.

$$(F * G)(t) \equiv \int F(\vartheta)G(t-\vartheta)d\vartheta \rightarrow \bar{F}(s) \times \bar{G}(s) \tag{A.13}$$

In this thesis, the convolution theorem, the linearity of both transformations and $\mathcal{L}\{1\} = 1/s$ are used to develop the time-dependent critical buckling load of the representative plate.

APPENDIX B: COMPACTION ROLLERS

Drawing of the Aluminum kernel manufactured for the polyurethane-based compaction rollers.

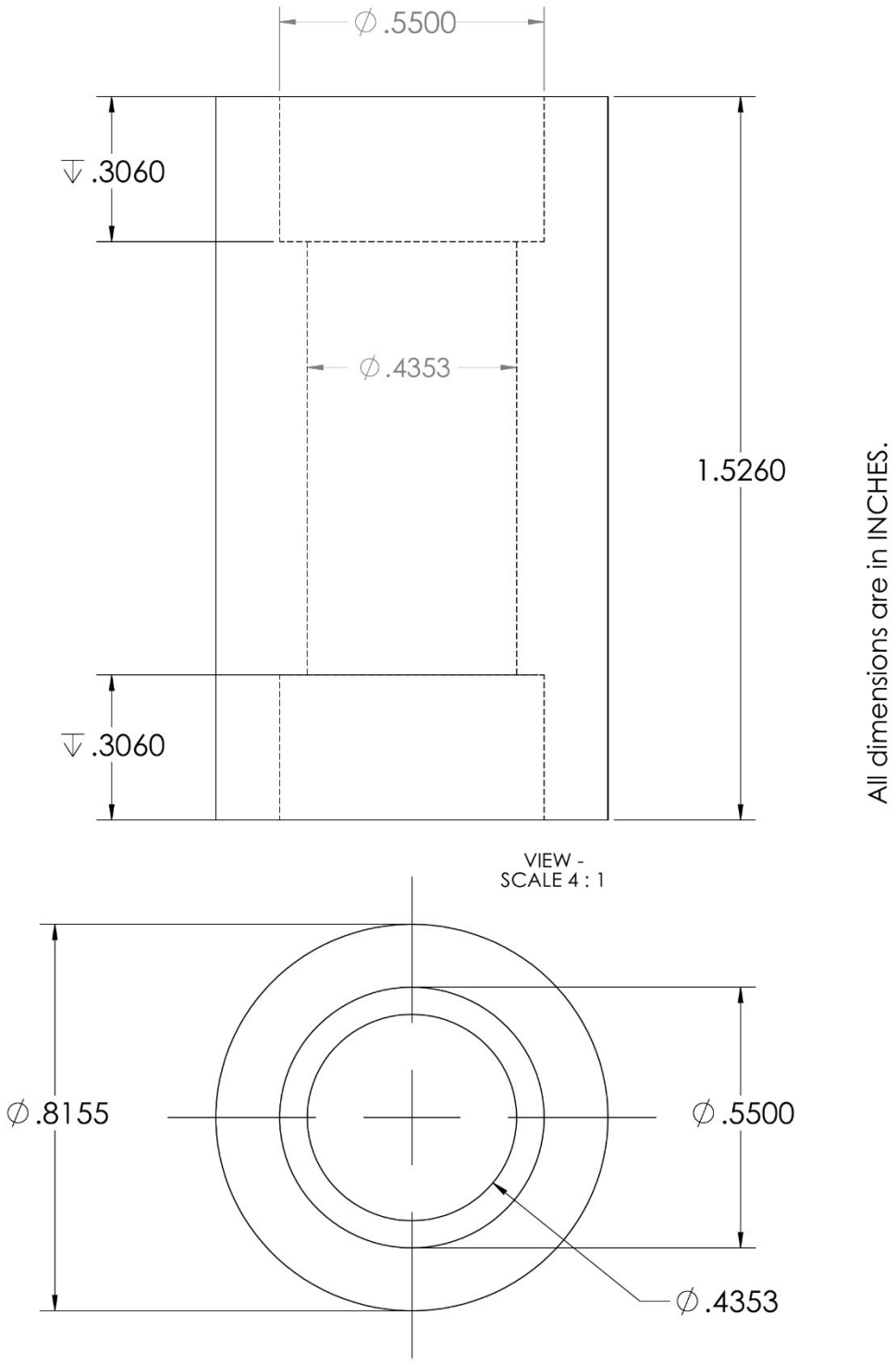

Drawing of the stainless steel compaction roller.